Si/C Nanocomposites for Li-ion Battery Anode

by

Yinjie Cen

A Dissertation

Submitted to the Faculty

of the

WORCESTER POLYTECHNIC INSTITUTE
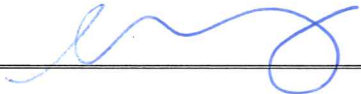
in partial fulfillment of the requirements for the

Degree of Doctor of Philosophy

in

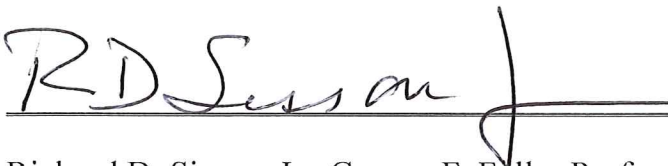Materials Science and Engineering

Jan 2017

APPROVED:

_____

Professor Jianyu Liang, Major Advisor

Associate Professor of Mechanical Engineering

_____

Richard D. Sisson, Jr., George F. Fuller Professor

Director of Manufacturing and Materials Engineering

Abstract

The demand for high performance Lithium-ion batteries (LIBs) is increasing due to widespread use of portable devices and electric vehicles. Silicon (Si) is one of the most attractive candidate anode materials for the next generation LIBs because of its high theoretical capacity (3,578 mAh/g) and low operation potential (~0.4 V vs Li^+/Li). However, the high volume change (>300%) during Lithium ion insertion/extraction leads to poor cycle life.

The goal of this work is to improve the electrochemical performance of Si/C composite anode in LIBs. Two strategies have been employed: to explore spatial arrangement in micro-sized Si and to use Si/graphene nanocomposites.

A unique branched microsized Si with carbon coating was made and demonstrated promising electrochemical performance with a high active material loading ratio of 2 mg/cm^2, large initial discharge capacity of 3,153 mAh/g and good capacity retention of 1,133 mAh/g at the 100th cycle at 1/4C current rate. Exploring the spatial structure of microsized Si with its advantages of low cost, easy dispersion, and immediate compatibility with the prevailing electrode manufacturing technology, may indicate a practical approach for high energy density, large-scale Si anode manufacturing.

For Si/Graphene nanocomposites, the impact of particle size, surface treatment and graphene quality were investigated. It was found that the electrochemical performance of Si/Graphene anode was improved by surface treatment and use of graphene with large surface area and high defect density. The 100 nm Si/Graphene nanocomposites presented the initial capacity of 2,737 mAh/g and good cycling performance with a capacity of 1,563

mAh/g after 100 cycles at 1/2C current rate. The findings provided helpful insights for design of different types of graphene nanocomposite anodes.

Acknowledgement

This thesis was completed under Prof. Liang, Jianyu's supervision. During my five years of Ph.D. life, she has been there, providing insight advice, encouraging me to keep moving forward and making me the man I am. I cannot be blessed more for my academic training under her guidance. It has been a great honor for me to be his Ph.D. student, and this good relationship will last forever. I could never have been here without her. I also want to thank Prof. Sisson, Prof. Shivkumar and Prof. Tao from Civil Engineering for being my committee members.

I would like to thank all the people I have been working with, including: Prof. Diran, Prof. Rao, Prof. Makhlouf, Prof. Burnham and Prof. Datta; Zhangfeng, Yangyang, Yuqin, Xi, Wisawat and Yangzi, etc. I've learned a lot from all the faculty members, also from all my dear friends. I am never along on my way pursuing the Ph.D. degree.

I would like to show my love to my parents: Li Cen and Xiaojun Lei. They have all their heart on me and I will never let them down. No matter where I go, we are always linked as a family. Their happiness is my deepest wish and I love them very much.

I would also like to show my love to my wife Yuchen Liu. We met here and married here. I am such a luck guy to have this wonderful special. I would love to have a happy life with her, forever.

At last, I want to dedicate this dissertation to my grandparents who were both gone during my Ph.D. period. I did not have the chance to say goodbye to them and I will regret for this forever. I will have them remembered in my heart.

Table of Contents

Chapter 1 Introduction

The ever-increasing demand for high energy power devices have never been such critical by now as the haze fog pollution is putting thousands people in danger. Electric Vehicle (EV) is considered as an alternative to gas-powered vehicle to reduce exhausts gases [1]. Lithium-ion batteries (LIBs) outperform other secondary power source such as nickel-cadmium (Ni-Cd) and nickel-metal hydride (Ni-MH) batteries. According to the report from National Renewable Energy Laboratory (NREL), the total demand of EV equipped LIBs in 2020 is estimated as 55 GWh, 15 billion-market, which is 3 times higher than that of 2016. However the EVs equipped with current LIBs cannot provide sufficient mileage to compete with gas-powered vehicles. The next generation of LIBs with high energy density, high power density, long cycle life, small volume occupation and safety concern are urgently demanded.
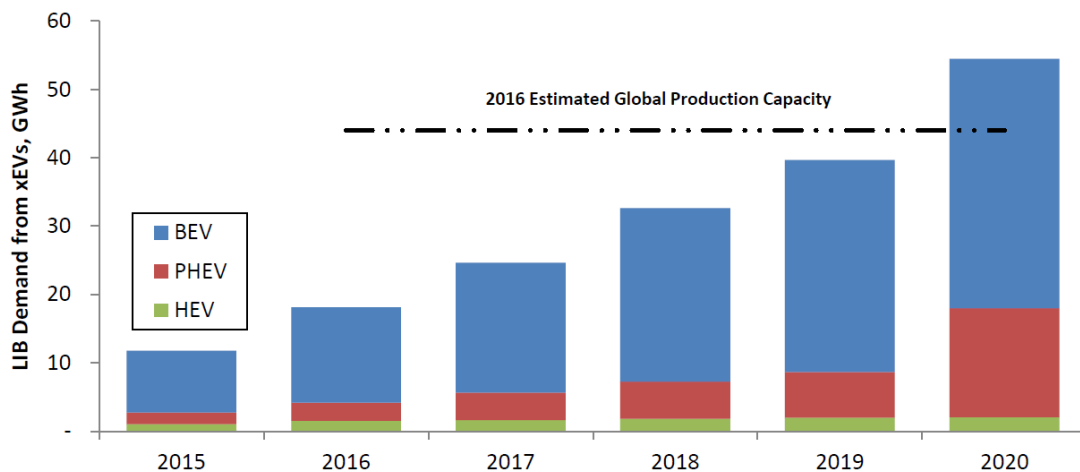
Figure 1-1: Estimated xEV LIB demand and global automotive LIB manufacturing capacity [2]

1.1 Research Objective

The goal of this work is to improve the electrochemical performance of Si/C composite anode for the next generation LIBs.

1.2 Research Plan

Two strategies have been employed: to explore spatial arrangement in microsized Si and to use Si/graphene nanocomposites. In details,

1. Al-Si alloy was used as Si source in order to obtain the spatial arrangement microsized Si by acid-etching mehod. The carbon coating process was followed to increase the conductivity. The active materials loading ratio was adjusted to meet high energy density. The electrochemical performance was tested and the structural information was investigated by X-ray Diffraction (XRD), Scanning Electron Microscopy (SEM) and the Cyclic Volumetric (CV).

 2. Si/Graphene nanocomposites was fabricated by static force assembly method. Si particles with size of 20-30 nm, 30-50 nm, 100 nm and 1-5 µm were selected to study the size impact. Si particle surface was modified by Piranha solution before (3-Aminopropyl)triethoxysilane (APTES) amide functionalization to investigate the impact of surface treatment by measuring zeta potential. The desired graphene quality in Si/Graphene nanocomposites was also concentrated by synthesizing three different graphene nanosheets, which were thermal reduced graphene, chemical reduced graphene and a chemical reduced graphene with improved modified Hummer's method. Raman spectrum, SEM and Electrochemical Impedance Spectroscopy (EIS) were used to characterize the graphene quality.

1.3 Dissertation Organization

There are 4 parts included in this dissertation: The introduction part provides the motivation, objectives and research plans for this study. The second part is a a comprehensive literature review solely for Si/Graphene nanocomposite anode to summarize its current advances in synthesis routine, novel nanostructure and electrochemical performance. The submitted or planning to submitted papers are listed in the third part. At last, a conclusion of this work and a perspective of Si/C anode is given in part four.

Reference

1.   Larcher, D. and J. Tarascon, *Towards greener and more sustainable batteries for electrical energy storage.* Nature chemistry, 2015. **7**(1): p. 19-29.
2.   Chung, D., E. Elgqvist, and S. Santhanagopalan, *Automotive Lithium-ion Cell Manufacturing: Regional Cost Structures and Supply Chain Considerations.* Contract, 2016. **303**: p. 275-3000.

Chapter 2 Literature Review of Si/Graphene Anode for LIBs

2.1 General Introduction of Si/C Anode in Li-ion Battery

Lithium-ion battery (LIB) has become the prevailing power supply/storage since its first commercialization as a portable electronic device in 1991 by Sony [1]. LIB possesses several advantages including high energy density, good charging rate, long cycle life and high power retention [2-5]. In addition, the LIB is considered as the best alternative option to replace the non-renewable fossil fuel for powering vehicles [6, 7]. The increasing demand for electric vehicles (EV) and hybrid electric vehicles (HEV) is expected to boost the LIBs mass production in the next 10 years [8]. A schematic diagram is given in Figure 2-1 to visualize the function mechanism of LIBs. However, high capacity, fast charging rate and low cost are demanded by customers. Developing new electrode materials for next generation LIBs remains a challenge.
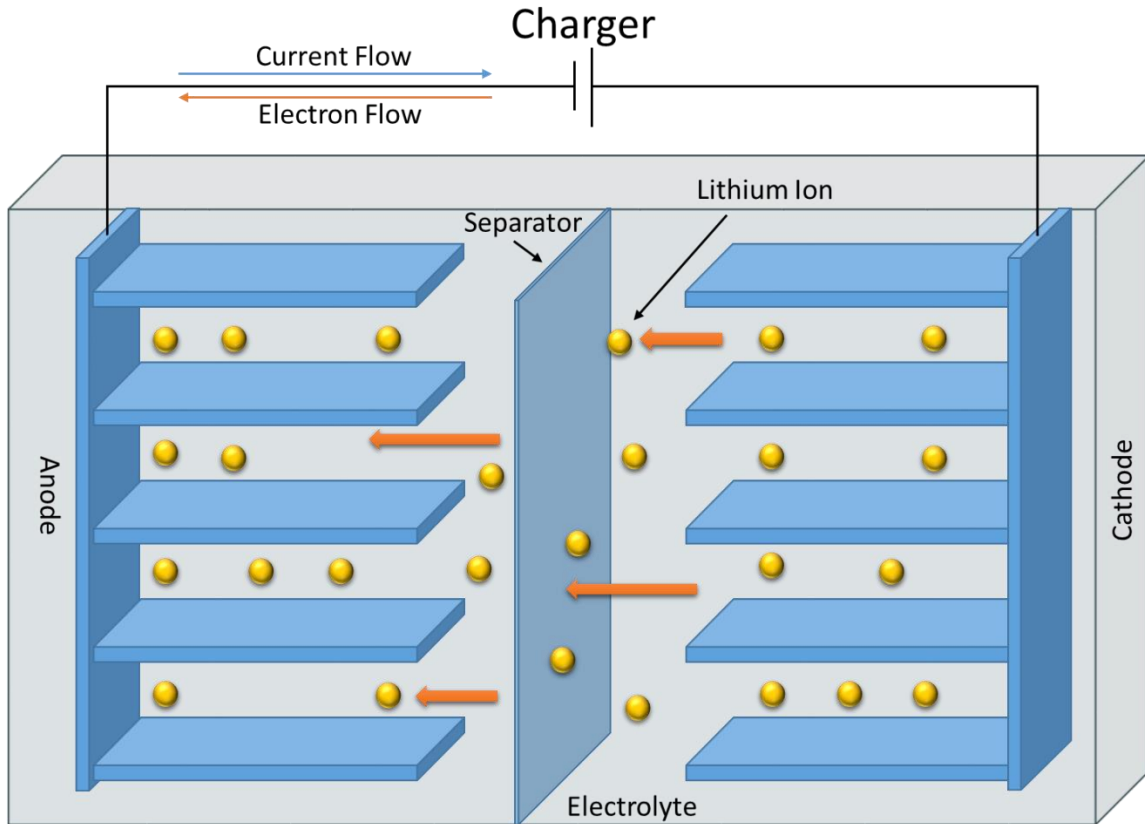
Figure 2-1: Schematic diagram of typical LIB in its charging process

2.1.1 Si as Candidate Anode Material in LIBs

Currently, Si is the most attractive candidate anode material for the next generation LIBs.

Comparing with graphite's highest lithiated state of LiC_6 with capacity of 372 mAh/g [9],

Si can contribute a capacity of 3,578 mAh/g by forming $Li_{15}Si_4$ at room temperature [10].

It also has the theoretical highest capacity of 4,200 mAh/g by forming $Li_{22}Si_5$ at elevated

temperature [11]. Besides its 10 times higher capacity than graphite, the discharging

potential of Si is about 0.2 V vs. Li/Li^+, which is very close to Lithium metal [10, 12]. This

low potential results in a high energy battery because the more voltage difference between

cathode and anode, the more power the full cell can deliver. Furthermore, Si ranks as the

2nd most abundant element in Earth's crust next to Oxygen [13] and it is environmental friendly. The properties of typical anode materials are summarized in Table 2-1, and Si clearly outperforms on many fronts. However, despite decades of intensive study on Si, a commercialized full cell with Si-based anode providing desirable rate and cycling performance is not available yet.

Table 2-1 Comparison of anode materials

	Li Meal	Graphite	Silicon
Potentail vs. Lithium	0	~0.15	~0.3
Theoretical Capacity (mAh/g)	~4,000	372 (LiC_6)	3,578 ($Li_{15}Si_4$)
Charging Rate	High Rate (>1C)	High Rate (>1C)	Low Rate (1/10C)
Cycle Life	Long	Long	Beyond Satisfied
Volume Expansion	~0%	Good (~10%)	Poor (320%)
Current Conditions	Abandoned	Most commercialized	In Lab

The main challenges that prevent Si-based anode from replacing graphite anode are the huge volume expansion during lithiation processes, slow lithium diffusion rate and low electronic conductivity. In fact, the volume of lithiated $Li_{15}Si_4$ is 370% of delithiated Si. There are serious consequences from issues beside the physical structural collapse, including that: 1) surface electrolyte interphase (SEI) layer becomes unstable after several cycles of lithiation and delithiation leading to short cycle life and pulverization; 2) active Si anode loses contact with conductive carbon and binder resulting in permanent capacity fading; and 3) Si anode performs poorly at high charging/discharging rate due to the low electron conductivity.

2.1.2 Methods to Improved Si Anode Performance

Nanotechnology

Nanotechnology is expected to offer new approaches to overcome some of the drawbacks discussed. The nanosized Si-based anode exhibits improved cycle life and high rate stability comparing with bulk Si-based anode [14]. The volume expansion remains, but the nanosize lessens long-distance stress. This can provide a higher specific capacity with an enhanced cycle life. Nanosized Si-based anode has significantly higher surface area which allows faster rate of lithium ion transportation during lithiation and delithiation. The faster lithium ion transportation rate will lead to an improved high rate performance and reduce the pulverization.

Carbon Coating

Another approach to increase the electron conductivity of Si-based anode material is the carbon coating method. This method has been intensively studied for many energy sources such as solar cell, fuel cell and LIBs. The conventional carbon coating method has proven itself being simple and efficient. In this method carbon precursors are introduced to the surface of active material and calcinated at elevated temperature to acquire the final product coated by layers of amorphous carbon. In Si-based anode, carbon coating not only increases the electron conductivity, but also acts as an 'anchor' to prevent the movement of loosed active Si clusters. Nanosized Si in combination with different forms of carbon materials are explored for high performance Si/C nanocomposite anode. These carbon forms include 0-D (amorphous, nanodot and nanoparticle), 1-D (nanowire and nanotube), 2-D (graphene

and thin film) and 3-D (porous) structures. Among them Si/graphene nanocomposite has great potential.

2.1.3 General Introduction of Graphene in LIBs

Graphene, a 2-D single layer of bonded carbon atoms was first synthesized by Novoselov and Geim in 2004 [15] through mechanical exfoliation method on bulk graphite flask. The structure of graphene is shown in Figure 2-2. Note that the hexagonal pattern could theoretically expend to infinity. Graphene exhibited exceptional physical properties, such as high electrical conductivity (10^6 S/m) [16, 17], high thermal conductivity (500~600 W/m·K) [18] and super stiffness (1.1×10^3 GPa Young's Modulus) [16]. Its unique physical properties can be attributed to its C=C resonance structure, hexagonally arrayed sp^2 σ bonding and π electron. Several synthesis methods have been explored, including exfoliation of graphite [19, 20], chemical vapor deposition (CVD) [21] and thermal/chemical reduce of graphite oxide (GO) [17, 20]. Among all the methods, graphene resulted from reduction of GO has the potential to be used in electrochemistry device such as photovoltaic cells, super capacitors and LIBs. The GO reduction is a process of low cost, simplicity and relatively high yield; In addition, side groups of thermal/chemical reduced GO can be tailored to fit the specific property demand of contain applications. The side groups could be oxide group (carboxyl, hydroxyl) or amine group (amine).
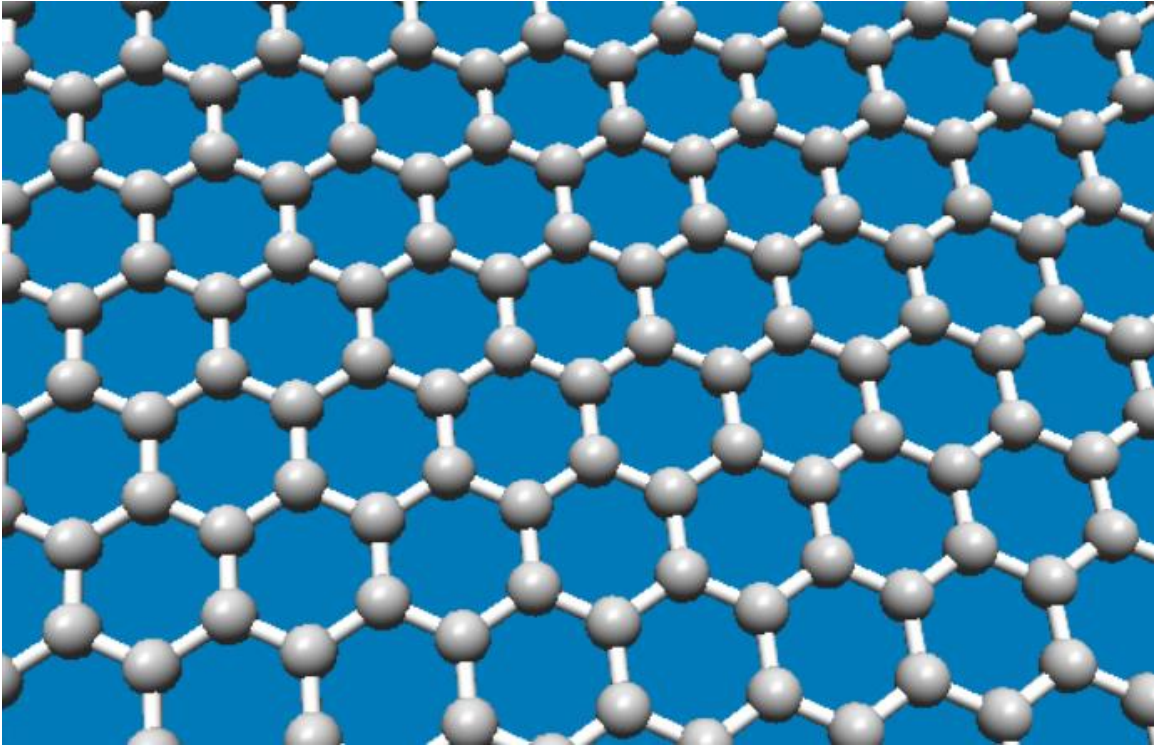
Figure 2-2: Graphene structure

Graphene can serve either an electrode material or an additive material in LIBs. Until the cost of synthesizing graphene becomes more feasible, the use of graphene as additive material seems to be applicable. The improvements of electrochemical performance have been reported in other anode materials like carbon based graphene composite, metal oxide/graphene composite and alloy with graphene. Therefore the fabrication of Si/graphene nanocomposite was the first step of this proposed study.

2.2 The Structures of Si Anode during Lithiation/Delithiation
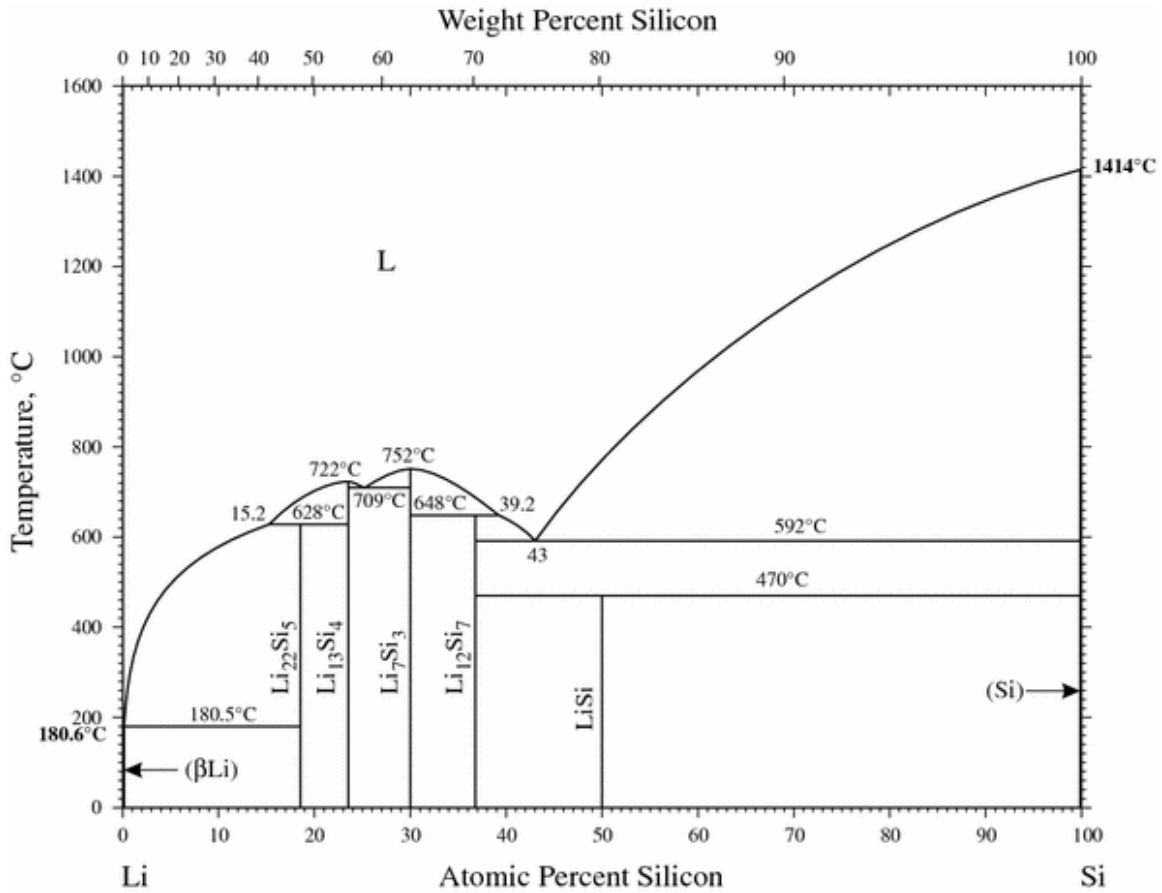
Figure 2-3: Li-Si Phase Diagram (Published in 2009)

There are five reported crystalline Li_xSi_y structures from the binary Li-Si phase diagram in

Figure 2-3 [22]. They are LiSi, $Li_{12}Si_7$, Li_7Si_3, $Li_{13}Si_4$ and $Li_{22}Si_5$. Among them, phase

$Li_{22}Si_5$ theoretically contributes the highest capacity of 4,200 mAh/g. However, none of

these five phases have been observed in Si based anodes at room temperature. It was

observed that the phases between the first lithiation and the second lithiation process are

significantly different. A typical charging/discharging curve for Si anode is presented in

Figure 2-4, in which 100 nm Si is selected as anode. The electrochemical performance test

follows standard procedure to prepare electrode slurry with weight ratio of Si, Binder

(PVDF) and Additives (Carbon Black) as 7:2:1. There are 5 plateaus labeled as Equation

(1) to (5) and the reactions for each plateau are listed below:

$$\text{Si (crystalline)} + x \text{ Li } \rightarrow \left(1 - \frac{x}{y}\right) \text{Si } + \frac{x}{y} \text{Li}_y\text{Si (amophous)} \qquad \text{Eq. (1)}$$

$$4 \text{ Li}_y\text{Si (amophous)} + (15 - 4y) \text{ Li } \leftrightarrow \text{Li}_{15}\text{Si}_4\text{(crystalline) at V} < 60\text{mV} \qquad \text{Eq. (2)}$$

$$\text{Li}_{15}\text{Si}_4\text{(crystalline)} \leftrightarrow 4 \text{ Li}_y\text{Si (amophous)} + (15 - 4y) \text{ Liat V} < 60\text{mV} \qquad \text{Eq. (2)'}$$

$$\text{Li}_{15}\text{Si}_4\text{(amophous) } \rightarrow 4 \text{ Si (amophous)} + 15 \text{ Li} \qquad \text{Eq. (3)}$$

$$\text{Si (amorphous)} + x \text{ Li } \rightarrow \left(1 - \frac{x}{y}\right) \text{Si (amophous) } + \frac{x}{y} \text{Li}_y\text{Si (amophous)} \qquad \text{Eq. (4)}$$
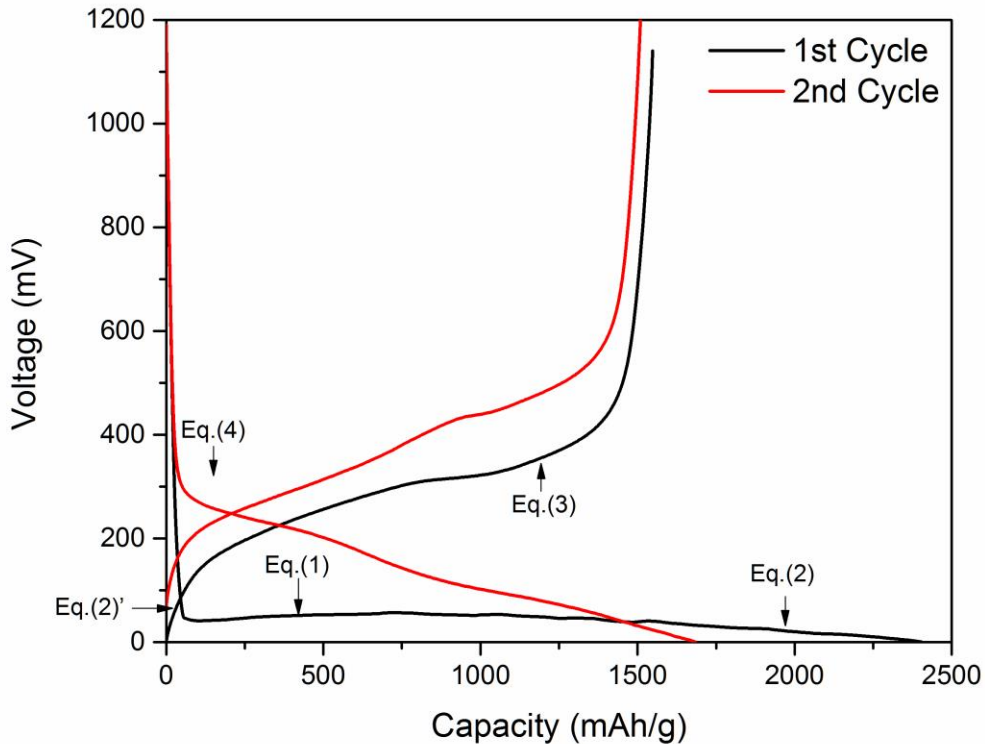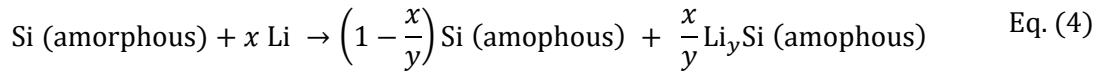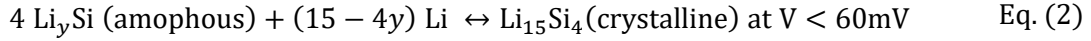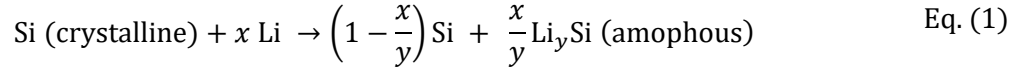
Figure 2-4: A typical charging/discharging curve for Si anode (~100 nm Si electrode, PVDF and Carbon Black; weight ratio 7:2:1, no further modification)

In fact, the first discharge reaction of Li and Si contains a process in which crystalline Si transfers into amorphous Si as confirmed by Chiang et al [23]. When the Si-based anode undergoes the first constant current discharging, the potential drops rapidly from initial state of open circuit current down to around 0.1 V vs Li/Li$^+$. Then the broad and flat plateau occurs between 0.08 V to 0.12V vs Li/Li$^+$ which indicates the crystalline Si is under lithiating, and transferring into amorphous Li$_y$Si as showing in Eq. (1). The full capacity of Si (3570 mAh/g, Li$_{15}$Si$_4$) can be reached just after the potential dropping down to 0 V vs Li/Li$^+$ as the amorphous Li$_y$Si transfers into crystalline Li$_{15}$Si$_4$ as seen in Eq. (2) from left to right. This recrystalline process begins at the potential of 60 mV vs Li/Li$^+$. During the first constant current charging process, the crystalline Li$_{15}$Si$_4$ breaks into small clusters of amorphous Li$_{15}$Si$_4$ as seen in Eq. (2)'. Then the chemical potential continuously increases up to about 0.4 V vs Li/Li$^+$ where crystalline Li$_{15}$Si$_4$ is transferring into amorphous Li$_{15}$Si$_4$ gradually. At the potential of 0.4 V vs Li/Li$^+$, amorphous Si is delithiated according to Eq. (3) as indicated by a plateau. During the second constant current discharging, the potential drops down to ~0.3 V vs Li/Li$^+$ then reaches a plateau resulted from amorphous Si transferring into amorphous Li$_y$Si as seen in Eq. (4). At the end of second discharging, the slope of pl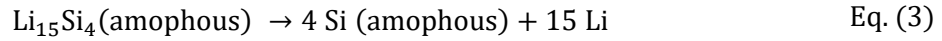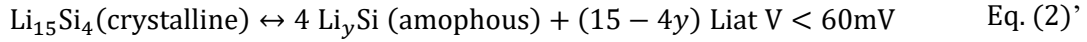ateau changes again because of the formation of crystalline Li$_{15}$Si$_4$ starting at potential of 60 mV vs Li/Li$^+$ as seen in Eq. (2). Thus, there is no crystalline Si after the first cycle if all the crystalline Si are reacted.

2.2.1 Si Anode Structure Change by XRD Method

All the phases presented before and after lithiation/delithiation at first cycle, and the following cycles have been confirmed by in-situ XRD study [24-26] as shown in Figure

2-5 and Figure 2-6 [26] and they are consistent with the description above. However the in situ XRD method is not able to precisely detect the phase changes during lithiation/delithiation process due to the nature of amorphous structure. There was unidentified phase detected during delithiation by Cui et al. The researchers failed to match the pattern to any of the known XRD data [26]. This phase disappeared when discharging finished.
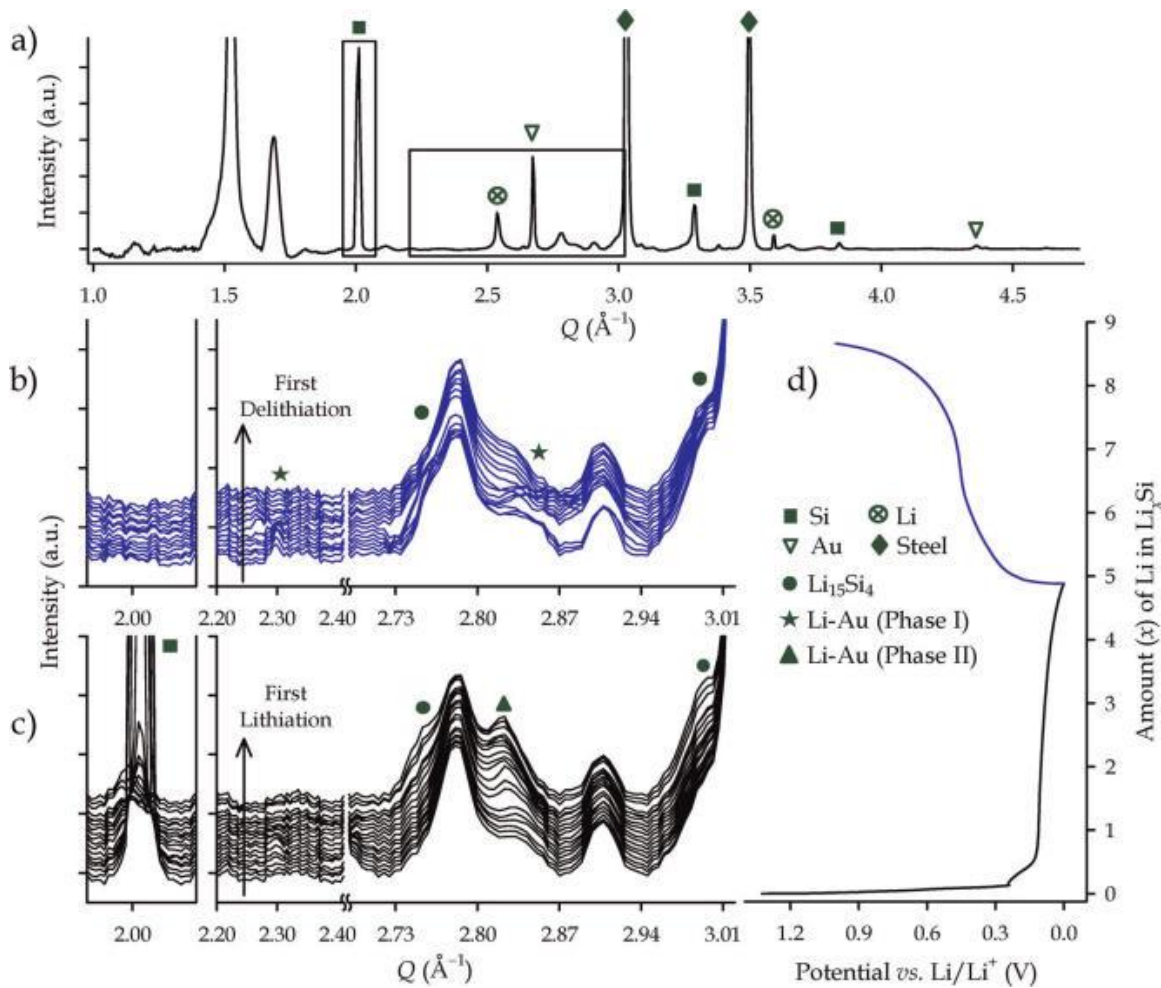
Figure 2-5: In situ XRD results for Si-anode cell cycled at C/5, a) XRD pattern at the start of lithiation, b) and c) XRD patterns showing zoom-in sections of a) for the first lithiation and the se delithiation respectively, and d) charging/discharging curve showing the first cycle as a function of the amount Li in Li$_x$Si. Unlabeled peaks are associated with either the polyester pouch or polymer separator [26].
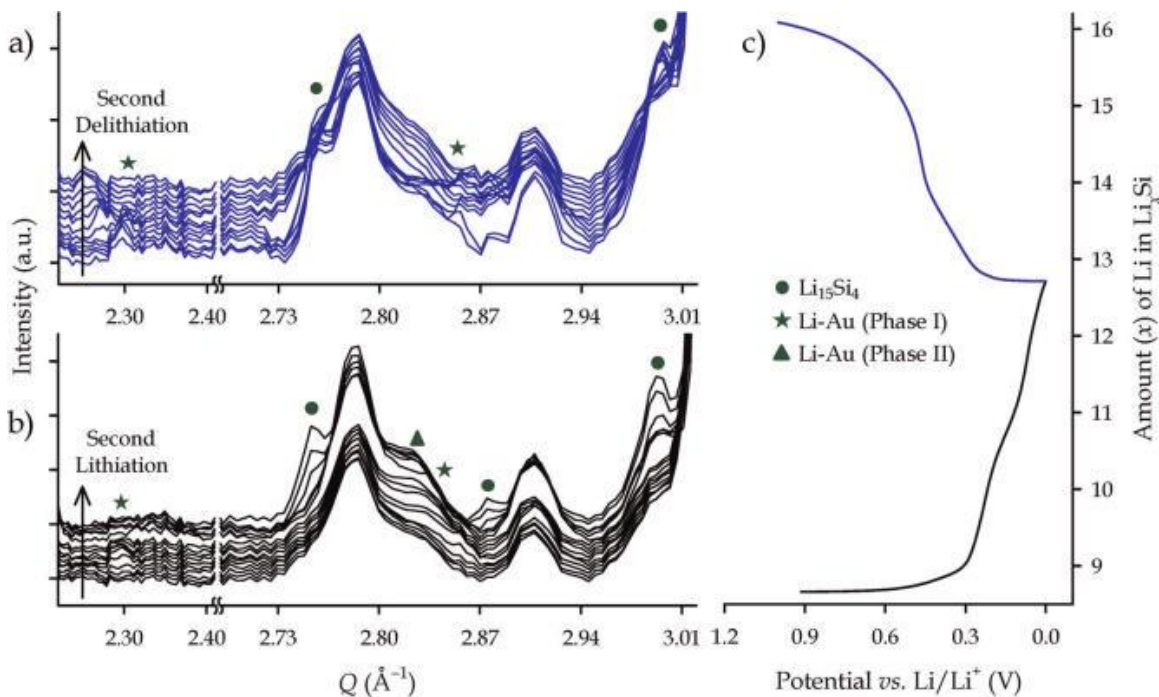
Figure 2-6: In situ XRD results for the same sample in Figure 2-5, a) and b) XRD pattern for the second lithiation and delithiation and c) charging/discharging curve showing the second cycle as a function of the amount Li in Li_xSi. Unlabeled peaks are associated with either the polyester pouch or polymer separator [26].

2.2.2 Si Anode Structure Change by TEM Method and Their Mechanical Properties

The lithiation/delithiation process was also studied by ex-situ and in-situ TEM technology. Zhou and Yu et al showed HRTEM images of Si nanowires (SiNWs) at different Li insertion level to confirm that the transformation from crystalline Si to amorphous Si, and to re-crystalline Si ($Li_{15}Si_4$) [27]. They also claimed that the amorphous nanosized Si particles showed a strong tendency to agglomerate during the process of lithiation/delithiation. The phase evolution of Si nanoparticles and nanowires during lithiation/delithiation was investigated by in-situ TEM and the process of phase transformation was videotaped [28, 29]. Atomic scale TEM images showed that the interface of crystalline Si and amorphous Si was atomically sharp (~1 nm thickness). The pathway of Lithium ions was also confirmed as shown in Figure 2-7, which were along

14

<110> and <112> directions during lithiation [30]. The interesting finding from their high resolution images was that the volume expansion during lithiation was anisotropic. It turned out that the favorable expansion direction for Si during lithiation was along <110> direction. Direction <111> was confirmed as the least swelling direction [28, 31]. The actual diameter changes were less than 10% along radial <111> but more than 200% along orthogonal <110>. And the different formations of Si nanowire growth under lithiation were given in Figure 2-8 as the formation of different cross sections with shapes of 4-fold, 2-fold and 6-fold symmetries for <100>, <110> and <111> pillars, respectively .
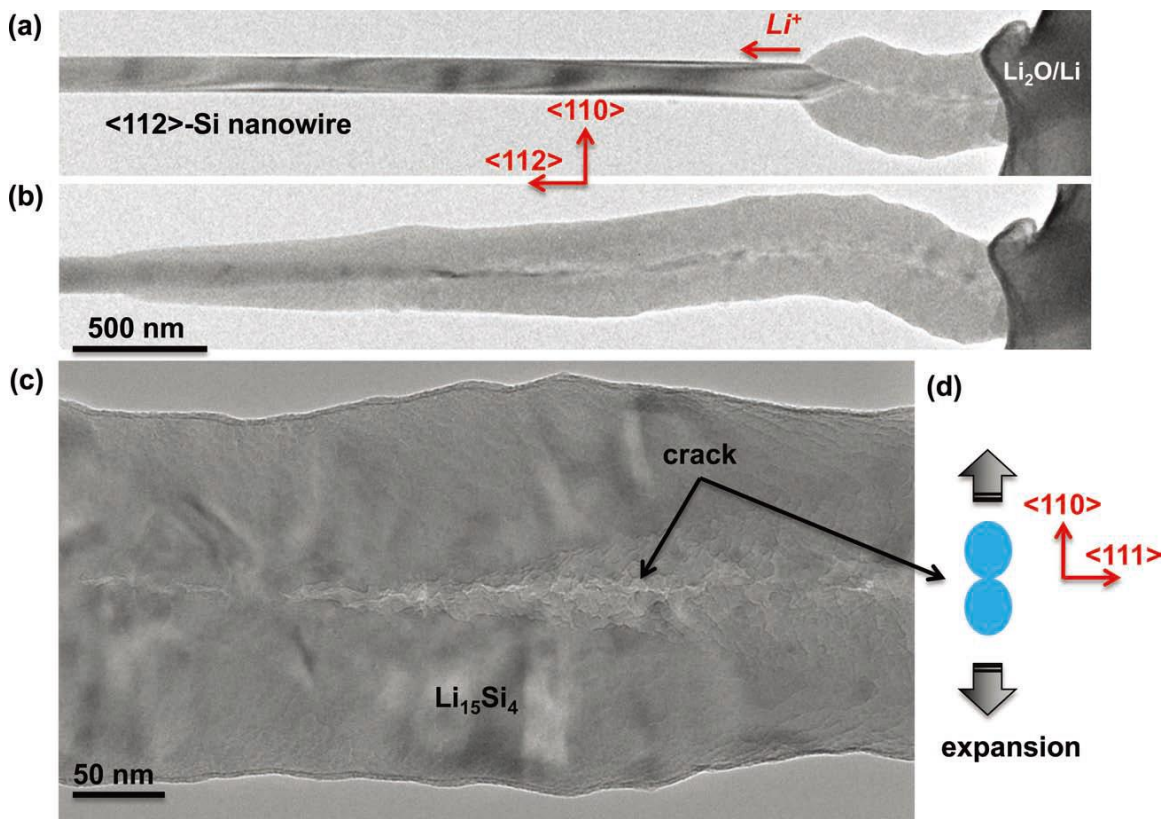
Figure 2-7: Anisotropic swelling and cracking of a <112> Si nanowire. a) and b) Snapshots showing progressive lithiation along both the axial and radial directions. The radial swelling was anisotropic. C) Enlarged image showing the central crack in the lithiated Si nanowire. d) Schematic illustration of the dumbbell-shaped cross section of a lithiated <112> Si nanowire viewed along the <112> direction [32].
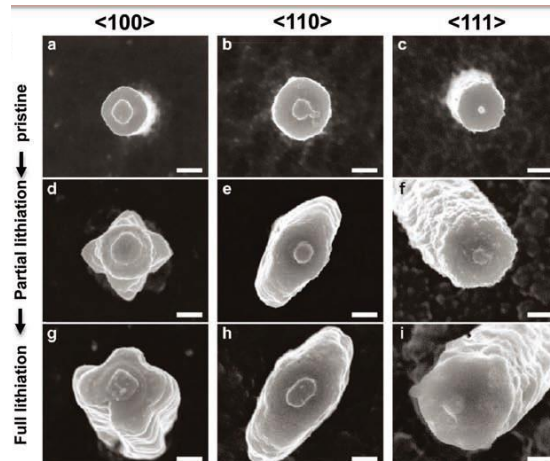
Figure 2-8: The anisotropic radial lithiation of Si pillars with different orientations in conventional ex situ cells. Preferential lithiation along <110> directions leads to formation of different cross sections with shapes of 4-fold, 2-fold and 6-fold symmetries for <100>, <110> and <111> pillars, respectively [32].

In the meantime, internal stress due to the structure change was studied. Nuzzo et al fabricated several ordered microstructural arrays in single crystalline Si embedding 1-, 2-, and 3 Dimensional design rules to study the structural dynamics and anisotropy of strain upon lithiation [33]. The anisotropy along with <110> direction was confirmed and similar to wet chemical etching of Si wafer in semiconductor industry [34-36]. Huang and Li et al reported an in situ tensile strength measurement of fully lithiated Si nanowires inside TEM chamber. Permanent fracture with fracture strain of 8% to 16% was observed. The axial tensile strength also decreased from 3.6 GPa for pristine unlithiated Si nanowires to 0.72 GPa for lithiated Si nanowires [37]. With the boundary of amorphous Si moving to crystalline Si during lithiation, the compressive stress was measured as 0.5 GPa in the amorphous layer. An essential finding was that at the tensile stress of 1.5 GPa during delithiation in the amorphous layer, plastic deformation happened inevitably [31, 38]. A simulated stress distribution of lithium ions in Si structure was presented by Liu et al as shown in Figure 2-9 where the Si nanowire was grown along [112] direction and the

preferred elongation direction was along [110] resulting in dumbbell-shaped deformation structure [31].
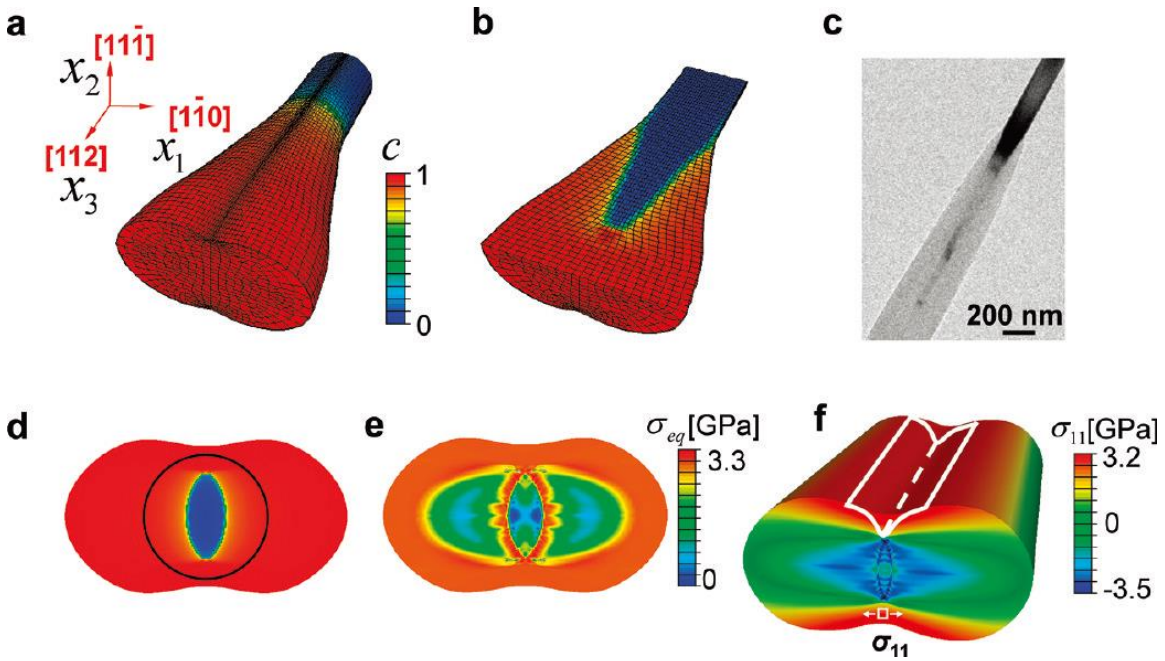
Figure 2-9: Simulated Li and stress distribution in a [112] oriented Si nanowire. a) 3-D simulation of a progressively lithiated nanowire showing the development of the dumbbell-shaped cross section along the longitudinal direction. The contour indicates the normalized Li concentration where 1 represents Li$_{3.75}$Si. b) The wire is cut to expose the Li distribution, showing the tapered Si core structure, which is correlated with TEM image of c). The Li distribution in (112) cross section at a representative postnecking stage. The black circle indicates the initial cross section of the pristine Si nanowire. e) Distribution of the von Mises Equivalent stress, correlated to Li distribution of Li in d); where red areas indicates plastic yielding; f) Schematic of neck growth along the longitudinal direction of the nanowire. The diminishing of central compression with increasing indent facilitates unstable necking growth (white lines) that can progress to form cracks [31].

Beside the study of Si nanowires and Si wafer, Si nanoparticles were also investigated by in-situ TEM [39-41]. As shown by the in-situ TEM in Figure 2-10, crystalline Si with a critical particle size of ~150 nm or below would be free of cracking; crystalline Si with size above 150 nm would suffer cracking during lithiation [42]. Based on the observation of the sharp interface between crystalline Si and amorphous Si by in-situ TEM, it was concluded that the transformation between the two phases was not continuous. And this rapid transformations resulted in hoop stress in the surface layers, which was considered

17

as the driving force of cracking. A model of concurrent reaction and plasticity in Si particles proposed by Suo et al agreed with the in-situ TEM observations [43]. Their simulation indicated the velocity of the reaction front related to the change in kinetic energy, while the stress field evolved according to the elastic-plastic theory. Thus the fracture could be averted when the particles was small and yield strength of lithiated Si was low. Furthermore, the kinetics of crystalline Si was limited by the Si-Si bond breakage. It was suggested that the rate of Si-Si breakage increased in the Li-rich area. As high concentration of Li weakened the Si-Si bonds, the two-phase boundary moved forward [30, 44, 45]. During the second and following lithiation process, there was no crystalline Si transferring into amorphous involved. However the lithiation process in amorphous could not be easily defined because lithium diffusion still involved breaking Si-Si bonds [29, 46]. The significant difference between amorphous and crystalline Si was that the amorphous Si did not crack during lithiation with micron particle size [29]. The non-fracture behaviors could be attributed to less breakage of Si-Si bonds, isotropic internal stress and boarder reaction interface. Thus, a better electrochemical performance can be expected from amorphous Si comparing with the crystalline Si.
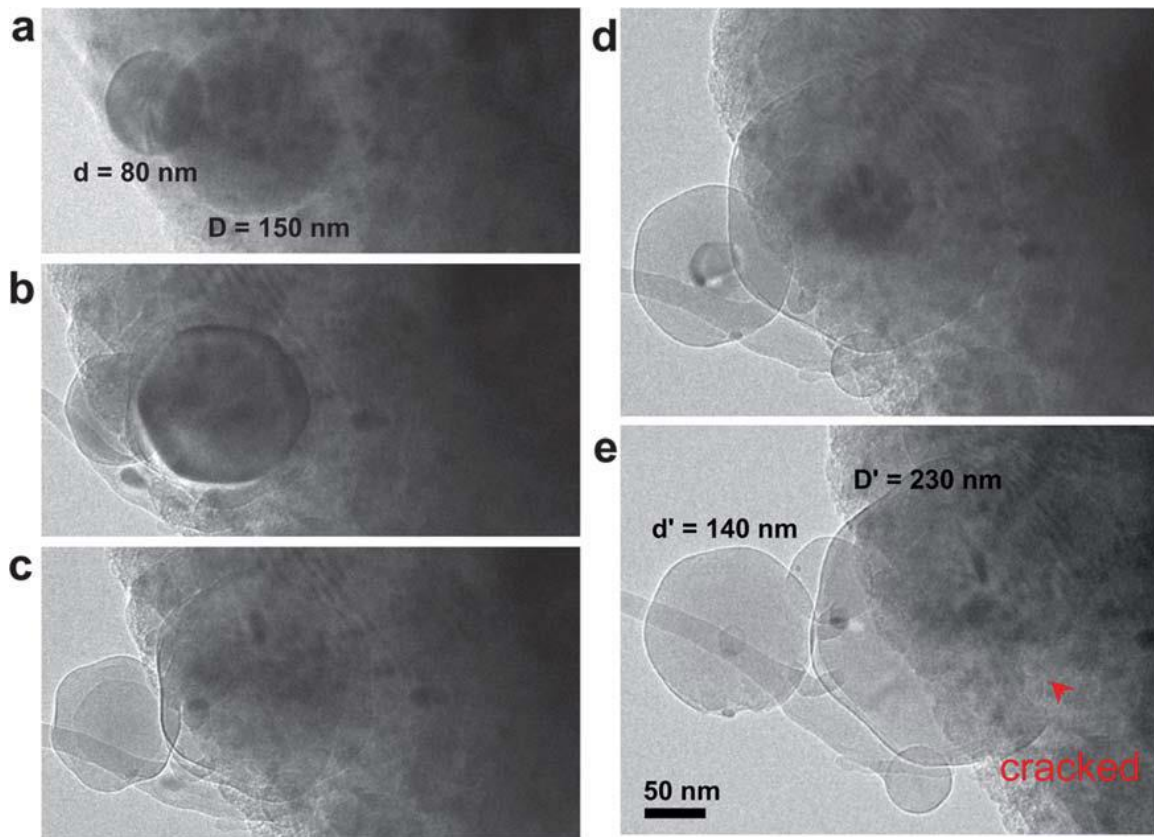
Figure 2-10: Size dependent fracture of Si nanoparticles during lithiation. a) Pristine Si nanoparticles with round shape. The smaller particle had a diameter of ~80 nm and the big one ~150 nm. b), c) and d) Lithiation process of the particles. The particles both showed core-shell structure with hexagonal SI cores and bumps in the lithiated shell. e) The larger particle cracked upon completion of lithiaion, while the smaller particle remain integral when fully lithiated. Note that the final diameter of the smaller particle was about 140 nm, accounting for an expansion by 75% [47].

2.2.3 Si Anode Structure Step-by-Step Change by NMR Method

As neither the in-situ XRD nor in-situ TEM is able to identify the phase during lithiation/delithiation process, Nuclear magnetic resonance (NMR) was employed to investigate the short-range order of crystalline and amorphous Si structures. During the first lithiation process, the crystalline Si was broken into isolated Si and Si-Si clusters. The Si-Si clusters then transferred into isolated Si. Eventually, at the end of lithiation all isolated Si recrystallized. . The recrystallized $Li_{15}Si_4$ contained excessive lithium which was extremely reactive in the electrolyte. Thus a loss of lithium happened resulting in an

increased open circuit voltage [44]. NMR confirmed that during the first lithiation, the crystalline Si (Diamond structure) began to gather initial Li on the silicon surface and then formed interstitial sites. The present Li ion brought in extra electron density to Si framework and weakened the Si network surrounding Li, resulting in breaking Si-Si bonds to form Si clusters surrounded by Li ions. As soon as the Si-Si bond breakage started, it would kinetically continue to break up more Si clusters instead of breaking up more Si framework. There was no crystalline structure such as Li_7Si_3 emerged because only the different ordered clusters existed and the activation energy needed to active the recrystallization of Si clusters was too high. This amorphous process continued to consume all crystalline Si above the potential of 85 mV. At 85 mV, isolated Si formed since the breakage of Si cluster became dominated. Then a crystalline structure began to nucleate below the potential of 50 mV and eventually formed metastable $Li_{15}Si_4$. The delithiation process began rapidly from both surface and core due to high Li ion diffusivity in $Li_{15}Si_4$. The delithiated $Li_{15}Si_4$ led to formation of Si clusters. Si clusters grew into an amorphous silicon matrix with the help of rapid diffusion of Li. The remaining isolated Si gathered from the already formed amorphous Si matrix until all the Li were gone. In the second lithiation, the amorphous Si was structurally more favorable for Li ions than that of crystalline Si to insert. The whole process were summarized in Figure 2-11 by Grey et al [48].
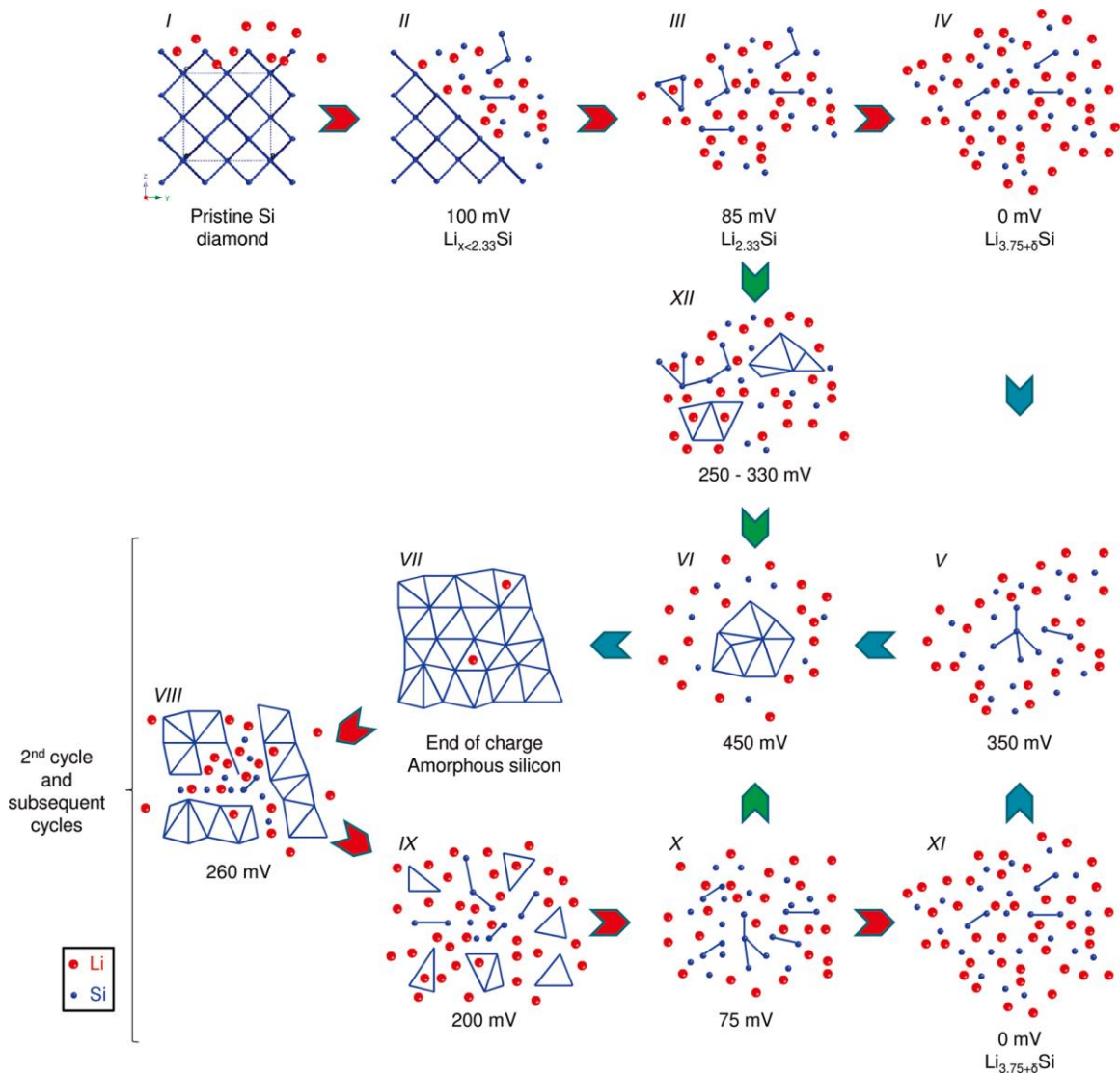
Figure 2-11: Illustration of mechanisms by which silicon is lithiated and delithiated. I to IV corresponds to lithiation of crystalline silicon discharged down to 0 mV. Red arrows denote discharge steps, while blue and green arrows denote charge steps. V to VIII correspond to the delithiation of fully lithiated silicon, and VIII to XI correspond to the relithiation of amorphous silicon to form fully lithiated silicon for cycle number > 1 [48].

2.3 Failure Phenomenal of Si anode in LIBs

2.3.1 Cracking of Si Anode during Lithiation/Delithiaion

Cracking of Si anode during cycling is the main issue that leads to battery failure. A Si thin film was used as the substrate to observe the cracking behavior during charging/discharging as reported by Wang et al [49]. A large-area nano-textured silicon

thin films (NTSTF) was prepared and the 1st lithiation process resulted in dendrite-like cracks on surface. After the 1st delithiation process, the cracking stayed visible by SEM. Due to the stress generated by charging/discharging process, the thin film eventually peeled off from its substrate and completely lost electronic contact after about 10 cycles. Several coating materials like Cu, Al_2O_3 and Ti were utilized with 2~5 nm thickness to restrain the cracks [49, 50] and each of them could help reduce the crack size, control the crack elongation then improve the electrochemical performance. These experiments agreed with the results from other coating method especially carbon coating.

High charging/discharging rate could also cause cracking, then lead to battery failure. As the agglomeration of lithium ions in small surface area under high current rate would turn Si into clusters. Surface coating with increasing conductivity could help transfer the electrons and ions then maintain the structure integer. Also considering the preferred expansion direction along <110>, the cracking may be controlled by engineering the structure orientation of Si anode. Nanocomposite is another option to reduce the damage from cracking by introducing the second phase to restrain the volume expansion.

2.3.2 SEI Formation on Si Surface and Its Cracking

The SEI layer is the side-product of charging/discharging process which involves the reaction between electrode and electrolyte at low potential vs. Li/Li^+. The SEI layer could have positive effects when it meets the following criteria:

1). The SEI layer should be able to conduct lithium ions and insulate electrons with the thickness less than 3 nm [51];

2) The SEI layer should also cover the particle surface completely or the electrolyte will be consumed continuously to form high resistance SEI layer, and

3) The SEI layer is preferred to be electrochemical, chemical and thermal stable during charging/discharging.

The SEI layer in the graphite anode meets all the criteria discussed above. However, the SEI layer in Si anode does not meet all the criteria.

The biggest concern of SEI layer in Si anode is its thickness. It has been reported by Li et al that during slow cycling, SEI layer on silicon nanocone (SNC) could be as thick as 5 µm [52]. Many studies have been conducted to understand the mechanism of SEI layer on Si anode, including XPS, FTIR, NMR, DSC-MS, IR and SERS [53-57]. It was revealed that there are two layers of SEI formed: an inner inorganic layer with LiF, LiOH and Li_2O and an outer organic layer with LiOR, PEO and other compounds [51, 56, 58]. All the species are decomposition products from electrolyte. Due to the volume expansion, the newly formed SEI layer on Si anode will continuously crack and then expose the fresh electrode surface to electrolyte. This unstoppable process results in accumulation of thick SEI layer. It also leads to the undesirable consumption of electrolyte and low cycling performance.

To mitigate the continuous formation of SEI layer on Si anode, smaller particle size, especially nanostructure Si anode is considered. The critical particle size which allows the formation of stable and thin SEI layer on Si anode without breaking in each lithiation/dilithation cycle is worth investigation. Another approach is to introduce additives into electrolyte. The additives such as vinylene carbonate (VC) [53, 59, 60], fluoroethylene carbonate (FEC) [61] and Lithium bis(oxalato)borate (LiBOB) [62]

significantly stabilizes the SEI layer and enhances the toughness of SEI layer. Profatilova et al pointed out that 10 wt% of VC could improve the thermal stability of SEI layers on Si anode at elevated temperature [63]. Lucht et al found that 10~15 wt% of FEC provided the highest specific capacity, best capacity retention and smallest impedance in the study of composition ratio range [64]. LiBOB was also tested as an additive in electrolyte for Si anode to sufficiently reduce the LiF content by generate a thin film with high concentration of oxidants to improve the cycling performance [60]. However, current studies about the SEI formation of Si anode are still incomplete and more quantitative analyses are needed.

2.4 Si Anode Structure and Morphology

Nanostructured Si anodes are attractive because of its high ratio of surface area vs. volume which effectively decreases the diffusion pathway of lithium ions resulting in high charging/discharging rate and better accommodation of side effects due to volume expansion. Nanosized Si anodes are commonly classified as 0-D, 1-D, 2-D and 3-D nanomaterials. But this classification is not sufficient to highlight the complexity of Si anode nanocomposites. A lot of structures, such as nano particle [65], nano wire [66, 67], nano tube [67], nano hollow pore [68, 69], thin film [70, 71], nanospheres [72, 73] and nano composite matrix [74], have been explored in the last 20 years.

2.4.1 0-Dimensional Si Nanoparticle

Si nanoparticle is the most commonly used 0-D Si source for anode in LIBs. In the year of 2000, Chen et al demonstrated the pure ball-shaped Si nanoparticles (NPs) which was

synthesized by laser-induced silane gas reaction method with particle size of 80 nm. Their high resolution TEM (HRTEM) revealed the ordered-disordered transition during lithiation/delithiation processes. HRTEM also witness the extraction of lithium ions promoted the recrystallization of lithium ion inserted Si in the range of nanometer. They also pointed out that the agglomeration of Si NPs was hard to control which could lead to irreversible capacity loss caused by lithium ions trapped in Si matrix [27]. Cho et al investigated the critical size of Si NPs synthesized by reverse micelles at high pressure and temperature in a bomb. The Si NPs with diameter of 5 nm, 10 nm and 20 nm were all treated with surfactant. It turned out that 10 nm Si NPs presented the most charging capacity of 4,443 mAh/g but had only 60% Coulombic Efficiency at its first cycle. The 20 nm Si NPs offered the best combined performance in both initial capacity and coulombic efficiency.

2.4.2 1-Dimensional Structured Nano Si

For 1-D materials, nanowires and Si nanotubes are two most commonly used candidates for Si anode. Cui et al first demonstrated Si nanowire which was able to accommodate large strain without pulverization in the year of 2008. The Si nanowire with an average diameter of ~89 nm was synthesized by vapor–liquid–solid (VLS) method on stainless steel substrates using Au catalyst. The theoretical capacity of 4,200 mAh/g was achieved at its initial discharging cycle with the rate of C/20 and the fading was negligible in the first 10 cycles [75]. One year later, Cho et al used the Si nanotubes as anode materials to assemble a full cell with $LiCoO_3$ as counter electrode showing a promising result on electrochemical performance. The Si nanotubes were synthesized by chemically depositing $SiCl_4$ and Tri

(ethylene glycol dimethyl ether) solvent onto porous alumina membrane templates. After multi-annealing steps, carbon coating was also performed to stabilize electrode-electrolyte interface. The full cell demonstrated a tremendous capacity retention after 200 cycles with a capacity of 2,600 mAh/g. After 200 cycles charging/discharging, the morphology of Si nanotubes were investigated by HRTEM. Though the HRTEM images indicated that expended tube thickness was as high as ~300 nm, comparing with original 40 nm, Si nanotubes were able to maintain their original morphologies with contribution from both carbon coating and small diameter size [67]. Kim, Rogers and Paik et al presented an arrays of sealed Si nanotubes structure which was fabricated by CVD method on scarified ZnO nanorods template resulting in 80% capacity retention after 50 cycles. Besides its electrochemical performance accommodated by architecture design, a more general design guideline was also provided by theoretical analysis of the mechanics. For Si nanowires and Si nanotubes with the same outer diameter, Si nanotubes are expected to have a better electrochemical performance. Because their inner space reduces the peak stress and results in larger surface area. The optimized Si nanotube inner and outer radii were also calculated and it was claimed that a nano triangular array of Si nanotubes could further improve its electrochemical performance [76].

2.4.3 2-Dementional Structured Nano Si

Vapor deposition is the most common way to acquire Si nano thin films. High energy source like heating, electron beam and laser are the primary methods to generate Si vapor for physical vapor deposition (PVD) [77, 78]. The sputtering methods involved in PVD are powdered by magnetic, plasma and radio frequency (RF) [79, 80]. PVD method are usually

applied to get amorphous Si thin film and the morphology and thickness of Si films can be adjusted precisely to meet the demand [81]. Chemical vapor deposition (CVD) is another alternative routine to fabricate pure Si thin film as its relatively cheap cost and low operation temperature. Thanks to the development of semi-conduct industry, the CVD method to fabricate Si thin film is very mature. Trichlorosilane ($SiHCl_3$) [82] and silane (SiH_4) [83] are two most commonly used silicon gas precursors. Most of the Si thin films resulted from CVD method are polycrystalline [84].

The most important property of Si thin film for LIBs is thickness as it will naturally impact the lithium ion diffusion distance. The preferred thickness of Si thin film is in the range of nanometers and the deviation should be as small as possible to contain the stress concentration. Adhesive energy between thin film and substrate can also determine the electrochemical performance of LIBs. Cu and stainless steel, mostly common used current collector for anode, can be directly used as substrate. Wei and Jiang et al fabricated a thin single crystal Si anode with thickness of 100~400 nm by transfer-printing inorganic devices for flexible/stretchable electronics method. The structure of this thin film Si anode was complex design which involved: Si anode was first derived from SOI wafer then doped by boron species at 20 keV following 900 ℃ annealing treatment for 1 min under N_2; The doped Si surface was patterned to form ribbons by reactive ion etching (RIE) following photolithography process to let Si ribbon rest on silicon wafer without being chemically bonded; after depositing sandwich-layered current collector with Cr/Au/Cr, the whole anode transferred onto Poly(dimethylsiloxane) (PDMS) substrate which was a soft elastomer substrate [85, 86]. The electrochemical performance were impressive with an extremely low fading rate of 0.033% degradation per cycle up to 500 cycles. The maximum

stress from the soft substrate was only 0.5 GPa at the state of 0.5 lithium ion insertion/extraction, comparing with that of more than 3 GPa from a rigid substrate [86]. Mullins et al also demonstrated a possibility routine to increase cycling stability of Si nano thin film anode by introducing about 20 at% amount of oxygen. The oxygen concentration was controlled by evaporating Si in a water ambient without changing the morphology of 500 nm Si thin film synthesized by reactive ballistic deposition (RBD) [87] method at glancing angles. Though scarified some of Si's capacity, the combination of homogeneous oxygen doping during the synthesis of the films and surface oxidation by low-temperature annealing in air provided the best cycling stability with virtually no capacity loss above 2,200 mAh/g for 120 cycles. Oxygen was believed to introduce portion of SiO_x species which had irreversible reaction with lithium ion then anchored the Si structure during cycling [88].

Modelling and simulation were also heavily performed to investigate the mechanism of Si nano thin film anode [89-91]. Maiti et al applied Langmuir–Mclean theory for segregation kinetics to study the degradation of the interface. The Si thin film with Cu substrate was considered as elasto-plastic materials. If there is no embrittlement observed in interface, crack propagated rapidly for very first several cycles then settled eventually with a fracture strength of 2 GPa. If embrittlement was considered, the extent of delamination would be enhanced [89, 91]. Also the fracture energies of Si thin film anode was simulated and tested by Choi et al as 12.0 ± 3.0 J/m^2 for amorphous silicon and 10.0 ± 3.6 J/m^2 for $Li_{3.28}Si$ [92]. Furthermore, the relationship between the thin film thickness and electrochemical performance of Si anode was studied by Demirkan et al by comparing the electrochemical performance of thickness ranged from 74 nm to 450 nm [93]. The results showed that a 4-

layer density modulated Si thin film with thickness of 380 nm provided a reversible capacity of ~1700 mAh/g at the 50th cycle with a high coulombic efficiency of ~99%, which was the best electrochemical performance among all their samples. Besides the fact that the Si thin film anode with a thickness within nanometer tended to have a better electrochemical performance than that within micrometer, the optimized thickness for Si thin film anode was highly depended on its design routine.

2.4.4 3-Dimensional Nano Si

The 3-D structured Si for anode is the extension from 0-D, 1-D and 2-D. It could be a matrix of Si nanoparticle bedded onto carbon nanotube and graphene sheet. It could also be a core shell structure, or even yolk shell structure. The imagination from scientists to fabricate suitable 3-D structure for Si anode seems unlimited but the logic behind each design follows the constant strategies, which are: 1) the selected materials could efficiently help constrain the volume expansion of Si anode; 2) the selected materials should conduct electrons and ions effectively; 3) the selected materials could also act as a barrier which allowed free movement of Si anode within engineered structure without losing contact. Wang et al fabricated a novel flexible 3-D Si/C fiber paper electrode which was synthesized by simultaneously electrospraying nano-Si-PAN (polyacrylonitrile) clusters. The electrospinning PAN fibers was also performed to carbonize coating layers. This combination allowed Si nanoparticles to uniformly distribute among 3-D carbon textile matrix network. The designed paper electrode was flexible and had high initial capacity of 1,600 mAh/g. It also presented a capacity loss of 0.079% per cycles for 600 cycles which demonstrated a good cycling performance. This 3-D Si/C fiber paper electrode could be

used in flexible electronic devices due to nature of bending paper [94]. Yushin et al designed a large-scale hierarchical bottom-up assembly route for Si nanocomposite anode. The Si was first coated onto annealed carbon black dendritic particles by CVD method, then another layer of carbon was coated onto Si surface by CVD method too. Then the whole nanocomposite were assembled into rigid spheres with open interconnected internal channels which were brought by previous carbon coating CVD method. The hierarchical rigid spheres were as big as 20 µm but assembled by ~20 nm Si particles. The electrochemical performance of hierarchical structured Si anode was promising with initial capacity of 1,950 mAh/g. There was almost no decay observed in its first 100 cycles at current rate of 1C [82]. Wang et al successfully synthesized a hierarchical 3-D carbon-coated mesoporous Si nanospheres at graphene form by thermal bubble ejection assisted chemical-vapor-deposition and magnesiothermic reduction method. The existing of graphene form provided sufficient spaces to accommodate the huge volume change of Si anode. The designed hierarchical structure maintained a stable cycling performance for more than 200 cycles at both low rate and high rate. At low charging/discharging rate of 500 mA/g, the capacity was maintained at 1,200 mAh/g after 200 cycles; at high charging/discharging rate of 10 A/g, the capacity remained ~700 mAh/g after 200 cycles with less than 5% capacity loss [95].

2.5 Si/Graphene Nanocomposite for LIB Anode

Considering the nature of Si's huge volume expansion and its low electric conductivity, GNS could be used as Si/GNS nanocomposite for LIB anode because it has unique properties of 1): mechanical flexibility, which could be regarded as barrier to hold the Si

structure change during lithiation/dilithiation; 2): electrochemical stability, which GNS itself does not react with most of current used electrode/electrolyte/separator materials; 3): super conductivity, which can conduct electrons with conductivity of ~10^6 S/m [17]. Thus the study of Si/GNS nanocomposite for LIB anode becomes essential as it has the potential to provide a possible solution for the next generation LIBs. A completely summary of Si/Graphene nanocomposite studies was also given in Table 2-2, as the morphology, method and correlated electrochemical performance were cleared stated.

2.5.1 The Early Stage Studies of Si/Graphene Nanocomposite

With the successful demonstration of graphene supported SnO_2 NPs as LIB anode, Kung et al was the first group to present the work on Si NPs-graphene composites for LIB anodes in the year of 2010 [96, 97]. The Si NPs-graphene paper composites in Kung et al's work began with the synthesis of graphene oxide (GO) by graphite oxidization. Then Si NPs with particle size less than 30 nm was pre-treated in air overnight to ensure the formation of silicon oxide layer on the surface. After mixing with GO and Si NPs, the mixture was collected by filter membrane then reduced under the flow of 10% H_2 in Ar at elevated temperature to form the Si-Graphene nanocomposites. The electrochemical performance of fabricated Si-Graphene nanocomposites was promising with approximately 1,950 mAh/g capacity at the first discharge and about 900 mAh/g capacity retention after 120 cycles for graphene reduced at 800 ℃ with current rate of 1,000 mA/g [96]. Following with the similar assemble procedure, Wang et al also demonstrated a free-standing graphene-Si composite film with graphene reduced by Hydrazine at mild elevated temperature (80 ℃) and the Si particle size ranged from 3 – 80 nm [98]. It highlighted an

excellent cycling performance with only 3% capacity loss from the fifth cycle (~820 mAh/g) to the one hundredth cycle (~800 mAh/g). Besides the Si NPs, there were also other formations of nano Si engineered with graphene to form Si-graphene nanocomposites. Yan et al was able to grow Si nanowires (SNWs) on graphene surface by loading Au NPs which resulted an initial capacity of ~3,500 mAh/g and cycling performance of above 1,500 mAh/g after thirty cycles at the current rate of 420 mA/g [99]. Liu and Zhu et al also fabricated a 3-D porous architecture of Si/graphene nanocomposites where 3-D Si was synthesized by Magnesiothermic Reduction method. Their 3-D porous Si/graphene nanocomposites demonstrated a discharging capacity retention of more than 400 mAh/g at the high current rate of 5,000 mA/g after 100 cycles [100]. As all the works mentioned above, the preparation of Si/graphene nanocomposites included only dispersion, mixing and synthesizing, from which there was no designed bonding mechanism was involved. Thus the electrochemical performance of those nanocomposites depended highly on NPs dispersion and intensive graphene loading (more than 30 wt % as shown in Table 2-2: A completely summary of Si/Graphene nanocomposites anode studies), which would significantly increase the capability to conduct electrons during charging/discharging.

2.5.2 The Bloomsome Stage Studies on Si/Graphene Nanocomposite

Since 2012, the study of Si/graphene nanocomposites shifted to introduce bonding energy between Si surface and graphene surface. Huang et al demonstrated an evaporation-induced capillary force wrapped graphene sheets around the Si NPs, where graphene was heavily crumpled to form the shell structure. Though the weight ratio of graphene was still high (40 wt %), it was the first attempt to capsule Si NPs with crumpled graphene shell.

This crumpled graphene-Si nanocomposites was claimed with an initial capacity of 1,175 mAh/g and only 86% capacity retention after 250 cycles. The crumpled graphene structure was believed to accommodate the expansion/contraction of encapsulated Si without fracture. The cycling performance was heavily improved because of this [101]. In 2013, Ji and Ruoff et al fabricated a graphene-encapsulated Si on Ultrathin-Graphite Foam (UGF) for LIB anode. In their work, Si NPs were first modified by poly(diallyldimethylammonium chloride) (PDDA) to have graphene oxide (GO) encapsulated. The resulted Si-GO NPs were then drop-casted on UGF surface, following with a thermal annealing process to obtain Si-graphene NPs on UGF. The UGF could provide a huge specific surface area of 20 per unit area of the nominal area due to UGF's porous 3-D structure with a pore diameter of 450 µm. The initial capacity of Si-graphene NPs on UGF was around 1,000 mAh/g and it could maintain the capacity above 400 mAh/g for 100 cycles at the current rate of 400 mA/g [102]. Li and Zhi et al proposed a novel self-supporting binder-free Si based anodes by encapsulation of Si NWs with dual adaptable apparels. First, overlapped graphene sheets were grown from as-synthesized Si NWs by Chemical Vapor Deposition (CVD) method to form Si NWs@G nanocables. The resulted powders were dispersed in graphene oxide aqueous solution before vacuum filtration then reduce the graphene oxide to obtain SiNWs@graphene@reduced graphene oxide structure for accommodation of volume expansion during lithiation. The buffer function of cabled graphene and reduced graphene oxide was confirmed by scanning transmission electron microscopy (STEM) from which there was no losing cluster from Si observed. As result, the fabricated SiNWs@graphene@reduced graphene oxide demonstrated excellent high rate cycling performance of above 95% capacity retention for 50 cycles at the current rate

of 840 mA/g and above 90% capacity retention for 100 cycles at the current rate of 2,100 mA/g while both the columbic efficiency were above 95% [103]. Another fast technique to fabricate Si-graphene nanocomposites was pyrolysis which began with freeze-drying of Si-GO suspensions. After pyrolysis process, the products was finalized by GO reduction at elevated temperature [104, 105].

2.5.3 The Strategies of Si/Graphene Nanocomposite Fabrication

Overall, most of the work on Si/Graphene nanocomposites followed the similar logic thoughts, which were: 1) the graphene oxide was mostly chosen to be applied as the precursor of graphene; 2) the number of graphene oxide synthesis methods were limited, like thermal expansion, hummers method and modified hummers method; 3) the synthesized graphene oxide was chemical bonded or static bonded with pretreated Si anode to form nanocomposites; 4) the whole nanocomposites were reduced either thermally or chemically under the present of reduction agents then the Si/graphene nanocomposites were formed. Most of the Si particles selected were within nanosize and most of the graphene synthesized were several nanometer thickness but expended in micro range. Thus it was essential to fabricate a structure not only being able to hold firmly contact between Si NPs and graphene, but also providing flexibility to accommodate the unpreventable Si volume expansion. Graphene can contribute both of above aspects. Furthermore, the effective of increased graphene weight ratio in Si/graphene nanocomposite had been investigated by Hwang et al, where Si/graphene with weight ratio of 3:1, 2:1, 1:1 and 1:2 were studied. The Si/graphene with ratio of 3:1 demonstrated the best balance on both initial capacity and cycling performance [106]. However the quality of graphene correlated

to the electrochemical performance of fabricated Si/graphene anodes had not established their corresponding relationship.

2.5.4 The Characterization Methods Involved for Si/Graphene Studies

The scanning electron microscope (SEM) was the first option for most scientists to observe the 2-D planer surface where the thickness and number of layers were not able to identify due to the limitation of SEM imaging resolution. The crumple surface of graphene sheet was also visualized by SEM pictures as the winkled surface morphology indicated a relatively high surface area of graphene could also contribute to increase the electron conductivity, which resulted in an improved electrochemical performance [101, 107]. The transmission electron microscope (TEM) was also applied to investigate the pristine crystal structure of Si anode, following with a highlight of graphene sheet by adjusting the contract of TEM image. The atomic force microscope (AFM) was utilized to measure the thickness of graphene nanosheets and most of the fabricated Si/graphene nanocomposites had graphene thickness of less than 10 nm [96, 99, 108]. However AFM was not able to tell if the graphene had only single layer due to some molecule absorbed on the graphene surface. Among all characterization methods, Raman spectrum was the most commonly used technique and it was believed to be the most efficiency way to demonstrate the quality of the synthesized graphene nanosheet/nanosheets [107, 109, 110]. With the concept of illuminating graphene with an incident light with certain wavelength to cause inelastic scattering, the Raman spectrum had feature peaks at 1340 /cm 1,584 /cm and 2,700 /cm for both graphite and graphene nanosheets. The peak at 1340 /cm was characterized as D band. The peak at 1,584 /cm was also called G band, which was caused by E_{2g} vibration mode

that represented the C=C bond stretching of all pairs of sp^2 atoms. The peak at 2,700 /cm was characterized as G' (2D) band, which was caused by double resonance process. The positions of both G and G' band could determine the number of layers of graphene nanosheets. For a single graphene, the peak position would have 5 /cm upshifting with constant intensity. The reason G' band also named as 2D band was because the G' peak would follow the movement of D peak with correlated number of layers of graphene nanosheets. There were actually two individual peaks identified in 2D band, which were $2D_1$ and $2D_2$ in graphite, but only $2D_1$ could be observed in single layer graphene. The intensity of $2D_2$ peak increased with the increasing number of graphene layers, then the 2D peak eventually grew into the typical graphite characteristic peaks as there were more than 5 layers graphene nanosheets stacked [109, 111]. The Raman spectrum could also provide information about the size graphene flakes and defect density by calculating the intensity ratio of D band and G band (I_D /I_G), where I_D and I_G represented the integrated intensities [112, 113]. Eigler et al had utilized Raman spectrum to analyze their synthesized graphene by wet chemical method [114]. However there were no sufficient reports that had established the relationship between graphene parameters (thickness, size and electron conductivity) and electrochemical performance in LIBs, the relative data on Si/graphene anodes were even less. This could be a potential topic that need to be covered in near future.

Table 2-2: A completely summary of Si/Graphene nanocomposites anode studies

Si Source with Ref.	Graphene Synthesis Method	Graphene Weight Ratio	Electrode Loading Weight (mg/cm^2)	Initial Reversible Capacity (mAh/g)	First Cycle Efficiency	Best Capacity Retention with Current Rate	Ref. with Similar Si/Graphene Structure
Si NPs [96]	Graphite Oxidation + H$_2$ Reduction	~40%	2	~2,050	~96%	300th, ~56%, 1,000 mA/g	[96, 115]
Si NPs [98]	Modified Hummers Method + Hydrazine Reduction	73.6%	NR	~1,000	~41%	100th, ~70.8%, 50 mA/g	[98]
Si NPs [116]	Hummers Method + Thermal Reduction	66.7%	NR	1,040	63%	30th, 94%, 50 mA/g	[104, 116-119]
Si NPs [120]	Thermal Expansion	~33%	NR	2,753	~80%	30th, ~91%, 300 mA/g	[120, 121]
Si NWs Mixed with Au [99]	Hummers Method + Hexane Reduction		NR	~3,500	57%	30th, ~67%, 420 mA/g	[99, 103]
Aerosol Droplets Si NPs [101]	Crumpled Reduction	40%	0.2	1,175	~95%	250th, ~86%, 1,000 mA/g	[41, 101]
3-D Porous Si by Magnesiothermic Reduction [100]	Hummers Method + Thermal Reduction	~40%	NR	1,100	~79%	100th, ~50%, 5,000 mA/g	[100, 106, 122-124]
Si NPs on Ultrathin-graphite Foam [102]	Hummers Method + Thermal Reduction	15.1%	1.5	1,000	62.5%	100th, ~37%, 400 mA/g	[102]
Si NPs on 3-D tree-like GNS [125]	Microwave Plasma CVD	19%	NR	2,731	~56%	160th, ~67%, 150 mA/g	[125]
(PANI)-Si NPs [105]	Modified Hummers Method + Pyrolysis Method	26%	0.3	~1,500	~70%	300th, ~76%, 2,000 mA/g	[105]
Si NPs on Electrospunned CNFs [125]	Chemical Method + Thermal Reduction	0.6%	NR	1,270	71.2%	50th, ~91%, 100 mA/g	[125]
Si NPs on Graphene Hydrogel [126]	Modified Hummers Method + Ascorbic Acid + Thermal Reduction	29%	NR	2,250	53%	150th, ~50%, 100 mA/g	[126]

3D Si NWs [127]	CVD + Plasma enhanced CVD	NR	~0.5	~2,600	97%	100th, ~29%, 500 mA/g	[127]

Reference

1. Nagaura, T. and K. Tozawa, *Lithium ion rechargeable battery.* Prog. Batteries Solar Cells, 1990. **9**: p. 209.
2. Armand, M., et al., *Cathode materials for secondary (rechargeable) lithium batteries*. 2003, Google Patents.
3. Padhi, A.K., K.S. Nanjundaswamy, and J.B. Goodenough, *Phospho-olivines as positive-electrode materials for rechargeable lithium batteries.* Journal of the Electrochemical Society, 1997. **144**(4): p. 1188-1194.
4. Etacheri, V., et al., *Challenges in the development of advanced Li-ion batteries: a review.* Energy & Environmental Science, 2011. **4**(9): p. 3243-3262.
5. Ji, L.W., et al., *Recent developments in nanostructured anode materials for rechargeable lithium-ion batteries.* Energy & Environmental Science, 2011. **4**(8): p. 2682-2699.
6. Goodenough, J.B. and K.-S. Park, *The Li-ion rechargeable battery: a perspective.* Journal of the American Chemical Society, 2013. **135**(4): p. 1167-1176.
7. Thackeray, M.M., C. Wolverton, and E.D. Isaacs, *Electrical energy storage for transportation—approaching the limits of, and going beyond, lithium-ion batteries.* Energy & Environmental Science, 2012. **5**(7): p. 7854-7863.
8. Chung, D., E. Elgqvist, and S. Santhanagopalan, *Automotive Lithium-ion Cell Manufacturing: Regional Cost Structures and Supply Chain Considerations.* Contract, 2016. **303**: p. 275-3000.
9. Shi, H., et al., *Structure and lithium intercalation properties of synthetic and natural graphite.* Journal of the Electrochemical Society, 1996. **143**(11): p. 3466-3472.
10. Weydanz, W., M. Wohlfahrt-Mehrens, and R.A. Huggins, *A room temperature study of the binary lithium–silicon and the ternary lithium–chromium–silicon system for use in rechargeable lithium batteries.* Journal of power sources, 1999. **81**: p. 237-242.
11. Li, H., et al., *A high capacity nano Si composite anode material for lithium rechargeable batteries.* Electrochemical and Solid-State Letters, 1999. **2**(11): p. 547-549.
12. Huggins, R.A., *Lithium alloy negative electrodes.* Journal of Power Sources, 1999. **81**: p. 13-19.
13. Reece, S.Y., et al., *Wireless solar water splitting using silicon-based semiconductors and earth-abundant catalysts.* Science, 2011. **334**(6056): p. 645-648.
14. Wang, G., et al., *Nanostructured Si–C composite anodes for lithium-ion batteries.* Electrochemistry Communications, 2004. **6**(7): p. 689-692.
15. Novoselov, K.S., et al., *Electric field effect in atomically thin carbon films.* science, 2004. **306**(5696): p. 666-669.
16. Chen, H., et al., *Mechanically strong, electrically conductive, and biocompatible graphene paper.* Advanced Materials, 2008. **20**(18): p. 3557-3561.
17. Stankovich, S., et al., *Synthesis of graphene-based nanosheets via chemical reduction of exfoliated graphite oxide.* Carbon, 2007. **45**(7): p. 1558-1565.
18. Balandin, A.A., et al., *Superior thermal conductivity of single-layer graphene.* Nano letters, 2008. **8**(3): p. 902-907.
19. Zhao, W., et al., *Preparation of graphene by exfoliation of graphite using wet ball milling.* J. Mater. Chem., 2010. **20**(28): p. 5817-5819.
20. Cai, M., et al., *Methods of graphite exfoliation.* Journal of Materials Chemistry, 2012. **22**(48): p. 24992-25002.
21. Losurdo, M., et al., *Graphene CVD growth on copper and nickel: role of hydrogen in kinetics and structure.* Physical Chemistry Chemical Physics, 2011. **13**(46): p. 20836-20843.

22. Okamoto, H., *Li-Si (Lithium-Silicon)*. Journal of Phase Equilibria and Diffusion, 2009. **30**(1): p. 118-119.

23. Limthongkul, P., et al., *Electrochemically-driven solid-state amorphization in lithium-silicon alloys and implications for lithium storage*. Acta Materialia, 2003. **51**(4): p. 1103-1113.

24. Hatchard, T. and J. Dahn, *In situ XRD and electrochemical study of the reaction of lithium with amorphous silicon*. Journal of The Electrochemical Society, 2004. **151**(6): p. A838-A842.

25. Li, J. and J. Dahn, *An in situ X-ray diffraction study of the reaction of Li with crystalline Si*. Journal of The Electrochemical Society, 2007. **154**(3): p. A156-A161.

26. Misra, S., et al., *In situ X-ray diffraction studies of (de) lithiation mechanism in silicon nanowire anodes*. Acs Nano, 2012. **6**(6): p. 5465-5473.

27. Li, H., et al., *The crystal structural evolution of nano-Si anode caused by lithium insertion and extraction at room temperature*. Solid State Ionics, 2000. **135**(1–4): p. 181-191.

28. Liu, X.H., et al., *Ultrafast electrochemical lithiation of individual Si nanowire anodes*. Nano letters, 2011. **11**(6): p. 2251-2258.

29. McDowell, M.T., et al., *In situ TEM of two-phase lithiation of amorphous silicon nanospheres*. Nano letters, 2013. **13**(2): p. 758-764.

30. Liu, X.H., et al., *In situ atomic-scale imaging of electrochemical lithiation in silicon*. Nature nanotechnology, 2012. **7**(11): p. 749-756.

31. Liu, X.H., et al., *Anisotropic swelling and fracture of silicon nanowires during lithiation*. Nano letters, 2011. **11**(8): p. 3312-3318.

32. Liu, X.H., et al., *In situ TEM experiments of electrochemical lithiation and delithiation of individual nanostructures*. Advanced Energy Materials, 2012. **2**(7): p. 722-741.

33. Goldman, J.L., et al., *Strain Anisotropies and Self‐Limiting Capacities in Single‐Crystalline 3D Silicon Microstructures: Models for High Energy Density Lithium‐Ion Battery Anodes*. Advanced Functional Materials, 2011. **21**(13): p. 2412-2422.

34. Hochbaum, A.I., et al., *Enhanced thermoelectric performance of rough silicon nanowires*. Nature, 2008. **451**(7175): p. 163-167.

35. Seidel, H., et al., *Anisotropic etching of crystalline silicon in alkaline solutions I. Orientation dependence and behavior of passivation layers*. Journal of the electrochemical society, 1990. **137**(11): p. 3612-3626.

36. Peng, K., et al., *Ordered silicon nanowire arrays via nanosphere lithography and metal-induced etching*. Applied Physics Letters, 2007. **90**(16): p. 163123.

37. Kushima, A., J.Y. Huang, and J. Li, *Quantitative fracture strength and plasticity measurements of lithiated silicon nanowires by in situ TEM tensile experiments*. ACS nano, 2012. **6**(11): p. 9425-9432.

38. Chon, M.J., et al., *Real-time measurement of stress and damage evolution during initial lithiation of crystalline silicon*. Physical Review Letters, 2011. **107**(4): p. 045503.

39. Li, H.Q. and H.S. Zhou, *Enhancing the performances of Li-ion batteries by carbon-coating: present and future*. Chemical Communications, 2012. **48**(9): p. 1201-1217.

40. Liu, B., et al., *Three-dimensional hierarchical ternary nanostructures for high-performance Li-ion battery anodes*. Nano letters, 2013. **13**(7): p. 3414-3419.

41. Yi, R., et al., *Dual Conductive Network-Enabled Graphene/Si-C Composite Anode with High Areal Capacity for Lithium-ion Batteries*. Nano Energy, 2014.

42. Liu, X.H., et al., *Size-dependent fracture of silicon nanoparticles during lithiation*. Acs Nano, 2012. **6**(2): p. 1522-1531.

43.   Zhao, K., et al., *Concurrent reaction and plasticity during initial lithiation of crystalline silicon in lithium-ion batteries.* Journal of The Electrochemical Society, 2012. **159**(3): p. A238-A243.

44.   Key, B., et al., *Real-time NMR investigations of structural changes in silicon electrodes for lithium-ion batteries.* Journal of the American Chemical Society, 2009. **131**(26): p. 9239-9249.

45.   Beattie, S.D., et al., *Si electrodes for Li-ion batteries—a new way to look at an old problem.* Journal of the Electrochemical Society, 2008. **155**(2): p. A158-A163.

46.   McDowell, M.T., et al., *Studying the kinetics of crystalline silicon nanoparticle lithiation with in situ transmission electron microscopy.* Advanced Materials, 2012. **24**(45): p. 6034-6041.

47.   Liu, X.H. and J.Y. Huang, *In situ TEM electrochemistry of anode materials in lithium ion batteries.* Energy & Environmental Science, 2011. **4**(10): p. 3844-3860.

48.   Key, B., et al., *Pair distribution function analysis and solid state NMR studies of silicon electrodes for lithium ion batteries: understanding the (de) lithiation mechanisms.* Journal of the American Chemical Society, 2010. **133**(3): p. 503-512.

49.   Wang, Y., et al., *Electrochemical performances and volume variation of nano-textured silicon thin films as anodes for lithium-ion batteries.* Nanotechnology, 2013. **24**(42): p. 424011.

50.   Wang, Y., et al., *Investigation of crack patterns and cyclic performance of Ti–Si nanocomposite thin film anodes for lithium ion batteries.* Journal of Power Sources, 2012. **202**: p. 236-245.

51.   Pinson, M.B. and M.Z. Bazant, *Theory of SEI formation in rechargeable batteries: capacity fade, accelerated aging and lifetime prediction.* Journal of the Electrochemical Society, 2013. **160**(2): p. A243-A250.

52.   Luo, F., et al., *Thick solid electrolyte interphases grown on silicon nanocone anodes during slow cycling and their negative effects on the performance of Li-ion batteries.* Nanoscale, 2015. **7**(17): p. 7651-7658.

53.   Chen, L., et al., *Effect of vinylene carbonate (VC) as electrolyte additive on electrochemical performance of Si film anode for lithium ion batteries.* Journal of Power Sources, 2007. **174**(2): p. 538-543.

54.   Chan, C.K., et al., *Surface chemistry and morphology of the solid electrolyte interphase on silicon nanowire lithium-ion battery anodes.* Journal of Power Sources, 2009. **189**(2): p. 1132-1140.

55.   Szczech, J.R. and S. Jin, *Nanostructured silicon for high capacity lithium battery anodes.* Energy & Environmental Science, 2011. **4**(1): p. 56-72.

56.   Lee, Y.M., et al., *SEI layer formation on amorphous Si thin electrode during precycling.* Journal of The Electrochemical Society, 2007. **154**(6): p. A515-A519.

57.   Zhuang, G., et al., *Study of SEI layer formed on graphite anodes in PC/LiBOB electrolyte using IR spectroscopy.* Electrochemical and solid-state letters, 2004. **7**(8): p. A224-A227.

58.   Favors, Z., et al., *Scalable synthesis of nano-silicon from beach sand for long cycle life Li-ion batteries.* Scientific reports, 2014. **4**.

59.   McAllister, M.J., et al., *Single sheet functionalized graphene by oxidation and thermal expansion of graphite.* Chemistry of materials, 2007. **19**(18): p. 4396-4404.

60.   Dalavi, S., P. Guduru, and B.L. Lucht, *Performance enhancing electrolyte additives for lithium ion batteries with silicon anodes.* Journal of The Electrochemical Society, 2012. **159**(5): p. A642-A646.

61.   Etacheri, V., et al., *Effect of fluoroethylene carbonate (FEC) on the performance and surface chemistry of Si-nanowire Li-ion battery anodes.* Langmuir, 2011. **28**(1): p. 965-976.

62.   Guo, J., et al., *Cyclability study of silicon–carbon composite anodes for lithium-ion batteries using electrochemical impedance spectroscopy.* Electrochimica Acta, 2011. **56**(11): p. 3981-3987.

63.   Profatilova, I.A., et al., *Enhanced thermal stability of a lithiated nano-silicon electrode by fluoroethylene carbonate and vinylene carbonate.* Journal of Power Sources, 2013. **222**: p. 140-149.

64.   Nguyen, C.C. and B.L. Lucht, *Comparative study of fluoroethylene carbonate and vinylene carbonate for silicon anodes in lithium ion batteries.* Journal of The Electrochemical Society, 2014. **161**(12): p. A1933-A1938.

65.   Lin, Y.-M., et al., *High performance silicon nanoparticle anode in fluoroethylene carbonate-based electrolyte for Li-ion batteries.* Chemical communications, 2012. **48**(58): p. 7268-7270.

66.   Hu, L., et al., *Si nanoparticle-decorated Si nanowire networks for Li-ion battery anodes.* Chemical Communications, 2011. **47**(1): p. 367-369.

67.   Park, M.-H., et al., *Silicon nanotube battery anodes.* Nano letters, 2009. **9**(11): p. 3844-3847.

68.   Zheng, Y., et al., *Nano-porous Si/C composites for anode material of lithium-ion batteries.* Electrochimica acta, 2007. **52**(19): p. 5863-5867.

69.   Ge, M., et al., *Porous doped silicon nanowires for lithium ion battery anode with long cycle life.* Nano letters, 2012. **12**(5): p. 2318-2323.

70.   Datta, M.K., et al., *Amorphous silicon–carbon based nano-scale thin film anode materials for lithium ion batteries.* Electrochimica Acta, 2011. **56**(13): p. 4717-4723.

71.   Peng, B., et al., *Lithium transport at silicon thin film: Barrier for high-rate capability anode.* The Journal of chemical physics, 2010. **133**(3): p. 034701.

72.   Yao, Y., et al., *Interconnected silicon hollow nanospheres for lithium-ion battery anodes with long cycle life.* Nano letters, 2011. **11**(7): p. 2949-2954.

73.   Wen, Z., et al., *Rational design of carbon network cross-linked Si–SiC hollow nanosphere as anode of lithium-ion batteries.* Nanoscale, 2014. **6**(1): p. 342-351.

74.   Hu, Y.S., et al., *Superior Storage Performance of a Si@ SiOx/C Nanocomposite as Anode Material for Lithium‐Ion Batteries.* Angewandte Chemie International Edition, 2008. **47**(9): p. 1645-1649.

75.   Chan, C.K., et al., *High-performance lithium battery anodes using silicon nanowires.* Nature nanotechnology, 2008. **3**(1): p. 31-35.

76.   Song, T., et al., *Arrays of sealed silicon nanotubes as anodes for lithium ion batteries.* Nano letters, 2010. **10**(5): p. 1710-1716.

77.   Yin, J., et al., *Micrometer-scale amorphous Si thin-film electrodes fabricated by electron-beam deposition for Li-ion batteries.* Journal of the Electrochemical Society, 2006. **153**(3): p. A472-A477.

78.   Birkmire, R.W. and E. Eser, *Polycrystalline thin film solar cells: present status and future potential.* Annual Review of Materials Science, 1997. **27**(1): p. 625-653.

79.   Minami, T., et al., *Highty conductive and transparent silicon doped zinc oxide thin films prepared by RF magnetron sputtering.* Japanese journal of applied physics, 1986. **25**(9A): p. L776.

80.   Shah, A., et al., *Thin‐film silicon solar cell technology.* Progress in photovoltaics: Research and applications, 2004. **12**(2‐3): p. 113-142.

81. Jovanov, V., et al., *Influence of interface morphologies on amorphous silicon thin film solar cells prepared on randomly textured substrates.* Solar Energy Materials and Solar Cells, 2013. **112**: p. 182-189.

82. !!! INVALID CITATION !!! {}.

83. Foo, K.L., et al., *Fabrication and characterization of ZnO thin Films by sol-gel spin coating method for the determination of phosphate buffer saline concentration.* Current Nanoscience, 2013. **9**(2): p. 288-292.

84. Becker, C., et al., *Polycrystalline silicon thin-film solar cells: Status and perspectives.* Solar Energy Materials and Solar Cells, 2013. **119**: p. 112-123.

85. Khang, D.-Y., et al., *A stretchable form of single-crystal silicon for high-performance electronics on rubber substrates.* Science, 2006. **311**(5758): p. 208-212.

86. Yu, C., et al., *Silicon Thin Films as Anodes for High‐Performance Lithium‐Ion Batteries with Effective Stress Relaxation.* Advanced Energy Materials, 2012. **2**(1): p. 68-73.

87. Flaherty, D.W., et al., *Growth and characterization of high surface area titanium carbide.* The Journal of Physical Chemistry C, 2009. **113**(29): p. 12742-12752.

88. Abel, P.R., et al., *Improving the stability of nanostructured silicon thin film lithium-ion battery anodes through their controlled oxidation.* ACS nano, 2012. **6**(3): p. 2506-2516.

89. Pal, S., et al., *Modeling of lithium segregation induced delamination of a-Si thin film anode in Li-ion batteries.* Computational Materials Science, 2013. **79**: p. 877-887.

90. Pal, S., et al., *Modeling the delamination of amorphous-silicon thin film anode for lithium-ion battery.* Journal of Power Sources, 2014. **246**: p. 149-159.

91. Bucci, G., et al., *Measurement and modeling of the mechanical and electrochemical response of amorphous Si thin film electrodes during cyclic lithiation.* Journal of the Mechanics and Physics of Solids, 2014. **62**: p. 276-294.

92. Choi, Y.S., et al., *A simple technique for measuring the fracture energy of lithiated thin-film silicon electrodes at various lithium concentrations.* Journal of Power Sources, 2015. **294**: p. 159-166.

93. Demirkan, M., L. Trahey, and T. Karabacak, *Cycling performance of density modulated multilayer silicon thin film anodes in Li-ion batteries.* Journal of Power Sources, 2015. **273**: p. 52-61.

94. Xu, Y., et al., *3D Si/C fiber paper electrodes fabricated using a combined electrospray/electrospinning technique for Li‐ion batteries.* Advanced Energy Materials, 2015. **5**(1).

95. Chen, S., et al., *Hierarchical 3D mesoporous silicon@ graphene nanoarchitectures for lithium ion batteries with superior performance.* Nano Research, 2014. **7**(1): p. 85-94.

96. Lee, J.K., et al., *Silicon nanoparticles-graphene paper composites for Li ion battery anodes.* Chem Commun (Camb), 2010. **46**(12): p. 2025-7.

97. Paek, S.-M., E. Yoo, and I. Honma, *Enhanced cyclic performance and lithium storage capacity of SnO2/graphene nanoporous electrodes with three-dimensionally delaminated flexible structure.* Nano letters, 2008. **9**(1): p. 72-75.

98. Wang, J.-Z., et al., *Flexible free-standing graphene-silicon composite film for lithium-ion batteries.* Electrochemistry Communications, 2010. **12**(11): p. 1467-1470.

99. Lu, Z., et al., *In situ growth of Si nanowires on graphene sheets for Li-ion storage.* Electrochimica Acta, 2012. **74**: p. 176-181.

100. Xin, X., et al., *A 3D porous architecture of Si/graphene nanocomposite as high-performance anode materials for Li-ion batteries.* Journal of Materials Chemistry, 2012. **22**(16): p. 7724-7730.

101.   Luo, J., et al., *Crumpled Graphene-Encapsulated Si Nanoparticles for Lithium Ion Battery Anodes.* The Journal of Physical Chemistry Letters, 2012. **3**(13): p. 1824-1829.

102.   Ji, J., et al., *Graphene‐Encapsulated Si on Ultrathin‐Graphite Foam as Anode for High Capacity Lithium‐Ion Batteries.* Advanced Materials, 2013. **25**(33): p. 4673-4677.

103.   Wang, B., et al., *Adaptable Silicon-Carbon Nanocables Sandwiched between Reduced Graphene Oxide Sheets as Lithium Ion Battery Anodes.* ACS Nano, 2013. **7**(2): p. 1437-1445.

104.   Chabot, V., et al., *Graphene wrapped silicon nanocomposites for enhanced electrochemical performance in lithium ion batteries.* Electrochimica Acta, 2014. **130**: p. 127-134.

105.   Li, Z.F., et al., *Novel pyrolyzed polyaniline-grafted silicon nanoparticles encapsulated in graphene sheets as li-ion battery anodes.* ACS Appl Mater Interfaces, 2014. **6**(8): p. 5996-6002.

106.   Ye, Y.-S., et al., *Improved anode materials for lithium-ion batteries comprise non-covalently bonded graphene and silicon nanoparticles.* Journal of Power Sources, 2014. **247**: p. 991-998.

107.   Ni, Z.H., et al., *Uniaxial strain on graphene: Raman spectroscopy study and band-gap opening.* ACS nano, 2008. **2**(11): p. 2301-2305.

108.   Chen, J., et al., *Enhanced electrochemical performances of silicon nanotube bundles anode coated with graphene layers.* Materials Research Bulletin, 2016. **73**: p. 394-400.

109.   Ferrari, A., et al., *Raman spectrum of graphene and graphene layers.* Physical review letters, 2006. **97**(18): p. 187401.

110.   Wang, Y.Y., et al., *Raman studies of monolayer graphene: the substrate effect.* The Journal of Physical Chemistry C, 2008. **112**(29): p. 10637-10640.

111.   Ferrari, A.C., *Raman spectroscopy of graphene and graphite: disorder, electron–phonon coupling, doping and nonadiabatic effects.* Solid state communications, 2007. **143**(1): p. 47-57.

112.   Cançado, L., A. Jorio, and M. Pimenta, *Measuring the absolute Raman cross section of nanographites as a function of laser energy and crystallite size.* Physical Review B, 2007. **76**(6): p. 064304.

113.   Ferreira, E.M., et al., *Evolution of the Raman spectra from single-, few-, and many-layer graphene with increasing disorder.* Physical Review B, 2010. **82**(12): p. 125429.

114.   Eigler, S., et al., *Wet chemical synthesis of graphene.* Advanced materials, 2013. **25**(26): p. 3583-3587.

115.   Park, S.-H., et al., *Self-assembly of Si entrapped graphene architecture for high-performance Li-ion batteries.* Electrochemistry Communications, 2013. **34**: p. 117-120.

116.   Tao, H.-C., et al., *Self-supporting Si/Reduced Graphene Oxide nanocomposite films as anode for lithium ion batteries.* Electrochemistry Communications, 2011. **13**(12): p. 1332-1335.

117.   Zhou, M., et al., *Graphene/carbon-coated Si nanoparticle hybrids as high-performance anode materials for Li-ion batteries.* ACS Appl Mater Interfaces, 2013. **5**(8): p. 3449-55.

118.   Chen, D., et al., *Facile synthesis of graphene–silicon nanocomposites with an advanced binder for high-performance lithium-ion battery anodes.* Solid State Ionics, 2014. **254**: p. 65-71.

119.   Su, M., et al., *Enhancement of the Cyclability of a Si/Graphite@Graphene composite as anode for Lithium-ion batteries.* Electrochimica Acta, 2014. **116**: p. 230-236.

120.   Xiang, H., et al., *Graphene/nanosized silicon composites for lithium battery anodes with improved cycling stability.* Carbon, 2011. **49**(5): p. 1787-1796.

121. Eoma, K., et al., *The design of a Li-ion full cell battery using a nano silicon and nano multi-layer graphene composite anode.* Journal of Power Sources, 2014. **249**: p. 118-124.

122. de Guzman, R.C., et al., *Effects of graphene and carbon coating modifications on electrochemical performance of silicon nanoparticle/graphene composite anode.* Journal of Power Sources, 2014. **246**: p. 335-345.

123. Li, H., C. Lu, and B. Zhang, *A straightforward approach towards Si@C/graphene nanocomposite and its superior lithium storage performance.* Electrochimica Acta, 2014. **120**: p. 96-101.

124. Kannan, A.G., et al., *Silicon nanoparticles grown on a reduced graphene oxide surface as high-performance anode materials for lithium-ion batteries.* RSC Advances, 2016. **6**(30): p. 25159-25166.

125. Li, N., et al., *Encapsulated within graphene shell silicon nanoparticles anchored on vertically aligned graphene trees as lithium ion battery anodes.* Nano Energy, 2014. **5**: p. 105-115.

126. Bai, X., et al., *Si@SiOx/graphene hydrogel composite anode for lithium-ion battery.* Journal of Power Sources, 2016. **306**: p. 42-48.

127. Güneş, F., *A direct synthesis of Si-nanowires on 3D porous graphene as a high performance anode material for Li-ion batteries.* RSC Advances, 2016. **6**(2): p. 1678-1685.

Chapter 3 Publications

Paper 1: A branched micro-sized Si anode for Lithium-ion batteries

Yinjie Cen[a], Yangyang Fan[a], Qingwei Qin[b*], Diran Apelian[a] and Jianyu Liang[a*]

a. Department of Mechanical Engineering, Worcester Polytechnic Institute, Worcester, MA, 01609 Unite State

b. The Key State Laboratory of Refractories and Metallurgy, Wuhan University of Science and Technology, Wuhan, Hubei 430081, China

Abstract:

Silicon (Si) with a theoretical capacity of 3,579 mAh/g is an attractive anode material for Lithium-ion batteries. Currently, nano-sized Si with a diameter in the range of less than 150 nm is the focus of research effort. However, difficulty to obtain a uniform dispersion and to increase the loading ratio of nano-sized Si remain challenging. In this work, a Lithium-ion battery anode was constructed using micro-sized Si from acid-etching of casting Al-Si alloy scraps. The acquired Si possessed a unique branched structure with a diameter of 0.5-1 µm in branches and 5-10 µm in length. Compared with the typical low loading ratio of much less than 1 mg/cm^2 in nano-sized Si anodes, this micro-sized Si anode had a typical loading ratio of 2 mg/cm^2. The branched Si with conventional carbon coating (Si/C) demonstrated an initial discharge capacity of 3,153 mAh/g at the current rate of 1/16C. It maintained a discharge capacity of 1,133 mAh/g at the 100th cycle under the current rate of 1/4C. The capacity decay was less than 0.2% per cycle from the 20th cycle to the 100th cycle. The Si/C composite showed a discharge capacity of 488 mAh/g at the current rate of 1C. After being cycled at a high rate of 1C, decreasing the current rate to

1/8C was shown to restore the capacity to 927 mAh/g after another 20 cycles. Micro-sized Si anode of branched morphology had advantages of low cost, easy dispersion, and immediate compatibility with the current industrial electrode manufacturing processes. This study suggests that employing micro-sized Si materials with rationally designed spatial structures may result in good electrochemical performance and may be of interest for high energy, high power density and large-scale next generation Lithium-ion batteries.

1. Introduction

The increasing demand for high power energy supplies motivates the exploration of alternative electrode materials for the next generation Lithium-ion batteries. Among all potential anode materials, Silicon (Si), the second most abundant element on earth, is attractive due to its high theoretical capacity of 4,200 mAh/g and its low working potential at 0.4 V vs. Lithium (Li). However, the theoretical capacity of 4,200 mAh/g for $Li_{22}Si_5$ can only be obtained at the molten temperature [1]. The fully discharged Si anode has a theoretical capacity of 3,579 mAh/g with a crystalline $Li_{15}Si_4$ structure, which is still almost ten times that of Graphite (372 mAh/g) [2]. The high specific capacity comes with over 300% volume expansion and contraction during lithiation/delithiation process. This volume change results in rapid pulverized deformation, lost electrical contact and unstable solid electrolyte interphase (SEI) that can lead to poor cycling performance and severe capacity fading. In additional, pure Si has a low electric conductivity (6.7×10^{-4} S/cm) which is the main obstacle, especially at a high rate [3-5].

Several strategies have been vigorously studied to mitigate the difficulties and improve the electrochemical performance of Si anode. These methods include: carbon coating to increase electric conductivity and to improve the structural stabilization [6]; chemical doping to facilitate the conductance of electrons [7]; using nano-sized Si anode such as nanofiber, nanotube and nanoporous structures [8-10]; dispersing Si into functional matrix to support the structure [11]; setting cut-off voltage to be higher than 80 mV during discharge to avoid recrystallization [12, 13]; employing additives such as fluoroethylene carbonate (FEC) and vinylene carbonate (VC) in electrolyte to stabilize the SEI layer [14, 15]; and using high strain polymer binder such as alginate hydrogel, carboxymethyl

cellulose (CMC) and poly(acrylic acid) (PAA) to constrain the deformation during delithiation [16, 17].

Even though tremendous efforts have been devoted to developing nano-sized Si anode, the industrial scale practice remains a challenge. First, the large surface area to volume ratio of nano-sized Si leads to increased side reactions with electrolyte. Second, the very low tapped density of nano-sized particles severely limits the volumetric energy density. Third, the current manufacturing process for mixing binder and carbon conductive material with the active materials cannot effectively overcome the severe agglomeration of nano-sized Si. Thus not all Si nanoparticles fully participate in lithiation/delithiation process. Very large amount of binder and carbon conductive material are necessary to obtain reported capacities in nano-sized Si anodes, which means decreased volumetric energy density. Submicro to micro-sized Si materials may mitigate some of the difficulties facing nano-sized Si. But the study on submicro to micro-sized Si materials for Lithium-ion batteries is scarce.

Earlier studies on micro-sized Si without any modification as the anode of Lithium-ion battery resulted in poor electrochemical performance. Yoshio et al studied 8 µm Si with a graphitic coating by thermal vapor deposition and reached a capacity of 800 mAh/g at the 20th cycle at a current rate of 1/5C [18]. More recently, Cui and Bao et al demonstrated a capacity of 2,000 mAh/g after 130 cycles at a current rate of 1/10C using silicon microparticles (SMPs) with particle size about 3-8 µm. The SMPs were mixed with a hydrogen-bonding polymer that could withstand high stress during volume expansion. However, The Si mass loading was 0.5-0.7 mg/cm^2 and no other study using this method or similar methods for micro-sized Si was reported [19]. Wang et al developed porous Si

micro-sized particles with carbon coating by thermal decomposing of resin and demonstrated a capacity of 1,400 mAh/g after 300 cycles at a current rate of C/4. However, there was only about 0.2 mg/cm^2 of active materials compared with the conventional 1-2 mg/cm^2 in order to get the reported high mass specific capacity [20].

In this work, a branched Si material was acquired by acid-etching of casting Al-Si alloy. The branched structure with a branch diameter of 0.5-1 µm and length of 5-10 µm was obtained reliably from adding Strontium (Sr) modifier during the casting of Al-Si alloy. The anode was then tested in coin cells with the initial discharge capacity of 3,153 mAh/g at the current rate of 1/16C. It maintained a discharge capacity of 1,133 mAh/g at the 100th cycle under the current rate of 1/4C. The stable electrochemical performance strongly suggests that spatial structure can be manipulated as another factor to enable microsized Si anode in large scale Lithium-ion battery manufacturing.

2. Experiments

Al-Si Alloy

The source of Si came from the scraps of Sr modified Al-Si alloy. The alloy was constituted from pure Aluminum ingots (99.99% purity) and Al-Si master alloys. Sr was added in controlled quantity to manipulate the Si morphology. The alloys were melt in an induction furnace in a clean silicon carbide crucible coated with boron nitride. The molten was degassed and then poured at approximately 800 °C. The casting was performed in a brass mold followed by air-cooling. The targeted Si content was 10 wt% and the Sr was added at less than 1 wt%. The weight of collected Al-Si alloys was about 20 g in the form of scraps.

Electrode Si/C composite preparation

Small pieces of Al-Si alloy were immersed in a 3 mol/L hydrogen chloride acid solution (HCl, Sigma-Aldrich, ACS reagent, 37%) for overnight with vigorous magnetic stirring (800 rpm). Al was dissolved and Si powders were obtained. The Si powders were collected by vacuum filtration then washed with deionized water (DI water, 18.2 $\mu\Omega$/cm electrical resistivity) and Ethanol (Sigma-Aldrich, 99.8%). The resulted powders were dried in a vacuum oven at 80 °C.

The Si powders were coated with carbon by conventional carbon coating method. The Si powders were wet mixed with sucrose (Ultra-Pure, MP Biomedicals Inc) in Methanol (Sigma-Aldrich, 99.9%) and the mixture was ground to fine particles. Carbon coated Si was obtained by heating the mixture to and holding it at 600 °C for 180 mins with a heating rate of 5 °C/min under N_2 flux. The carbon coating could improve the electric conductivity and prevent pulverization at high current rates.

Materials Characterization

The chemical composition of Al-Si alloy was collected by Optical Emission Spectrometry (OES, Spectro). X-ray Diffraction (XRD) patterns of powder Si were recorded (Cr Kα radiation at λ=2.23 Å, the 2θ angle from 30°-130°, XRD PANALYTICAL EMPYREAN). Scanning Electron Microscopy (SEM, JEOL JEM-7000F) equipped with an Energy Dispersive X-ray Spectrometry (EDX, Oxford Instrument) was used to study the morphology and composition of Si and Si/C powder. The actual carbon content in Si/C composite was measured by Thermogravimetric Analyzer (TGA Q50, TA instruments) with a heating rate of 10 °C/min.

Electrochemical Measurements

To make the working anode, Si or Si/C powder was mixed with Timical Super C65 conductive carbon black (MTI Corporation) and Carboxymethyl Cellulose Sodium (CMC, Sigma-Aldrich) as binder in DI water. The weight ratio of the prepared slurry was 70 wt % of Si, 15 wt % of conductive carbon black and 15 wt % of binder. The slurry was then cast on a copper foil and dried at 60 °C for 10 hours and then at 80 °C overnight under vacuum. The loading weight of active material in the fabricated electrode was about 2 mg/cm^2. Coin cells were assembled using Li metal foil as counter electrode and a Celgard 2400 membrane as separator. The electrolyte composed of 1 mol LiPF$_6$ in a mixture of Ethylene carbonate (EC), Diethyl Carbonate (DEC) and Dimethyl Carbonate (DMC) with 1:1:1 volume ratio. All the coin cells were tested on MTI BST8-WA at room temperature for galvanostatic charge and discharge in the range of 0.001–1.5 V. Current density was

defined using 3,579 mA/g as 1C. The Cyclic Voltammogram (CV) at a scanning rate of 1 mV/s was tested by BASi 100B electrochemical analyzer.

3. Results and Discussion

The chemical composition and structure of Si/C composite

Table 3-1 OES analysis of Al-Si alloy chemical composition

Element	Si (%)	Sr (%)	Al (%)	Others (%)
Weight Concentration	10.675	0.013	89.300	0.012

Table 3-1 showed the chemical composition of Al-Si alloy assessed by OES. The major components in the used Al-Si alloy were 89.3 wt% of Al, 10.675 wt% of Si and 0.013 wt% of Sr. There were about 0.012 wt% of other impurity elements combined including Na, Ca and Fe. HCl and HNO_3 effectively reacted with the metallic components except for pure Si. If trace amount residues such as Al, Sr or other metallic compound remained after acid etching, the metallic residue might serve as dopants on the surface of Si powder and contribute to increasing the electronic conductivity.
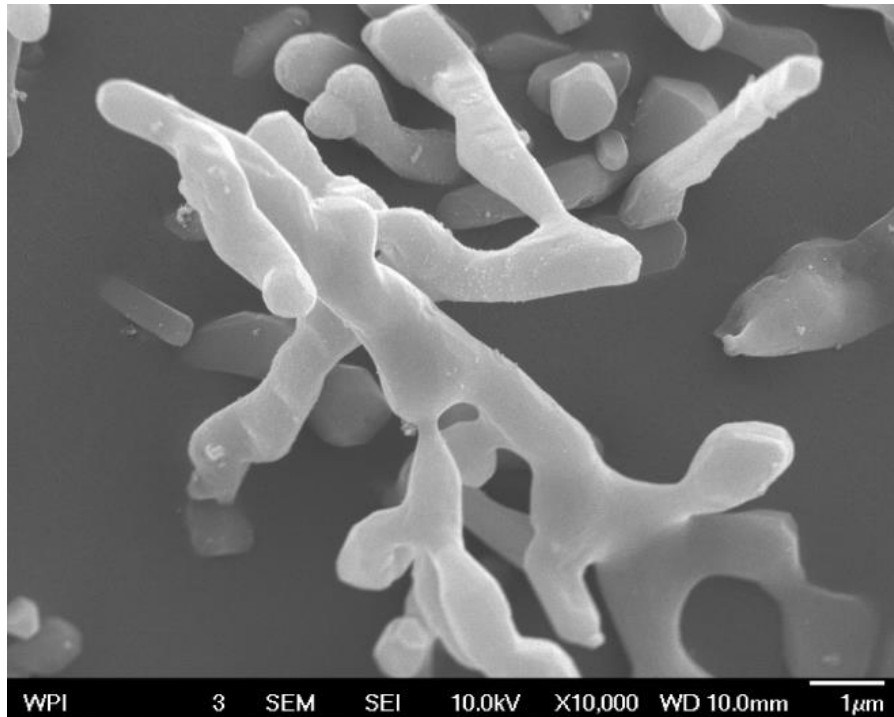

Figure 3-1: The surface morphology of branched micro-sized Si in SEM

Figure 3-1 clearly showed the branch-like morphology of acquired Si powders. The diameter of the branches typically ranged from 0.5 µm to 1 µm. The length of each branch varied from 5 µm to 10 µm. Agglomeration was not observed in either pure Si powder (Figure 3-1) or Si/C composite (Figure 3-2 (a)) due to their micro-size. By comparing the morphology before and after carbon coating, it could be concluded that the conventional carbon coating retained the branched structure. EDX mapping results in Figure 3-2 (c-e) showed that the carbon and oxygen uniformly distributed along the Si branches. It indicated successful Carbon coating on the surface of Si. The actual concentration of each element was also semi-quantitative recorded by EDX as 86.5 wt% of Si, 12.1 wt% of C and 1.4 wt% of O. The oxygen may belong to the SiO_2 layer which existed naturally in our samples. In fact, the 1.4 wt% of oxygen level corresponded to 2 wt% of SiO_2, which was smaller than that of nano-sized Si which could be more than 20 wt% [21, 22]. This low oxygen content can be contributed to the micro-sized of the Si.
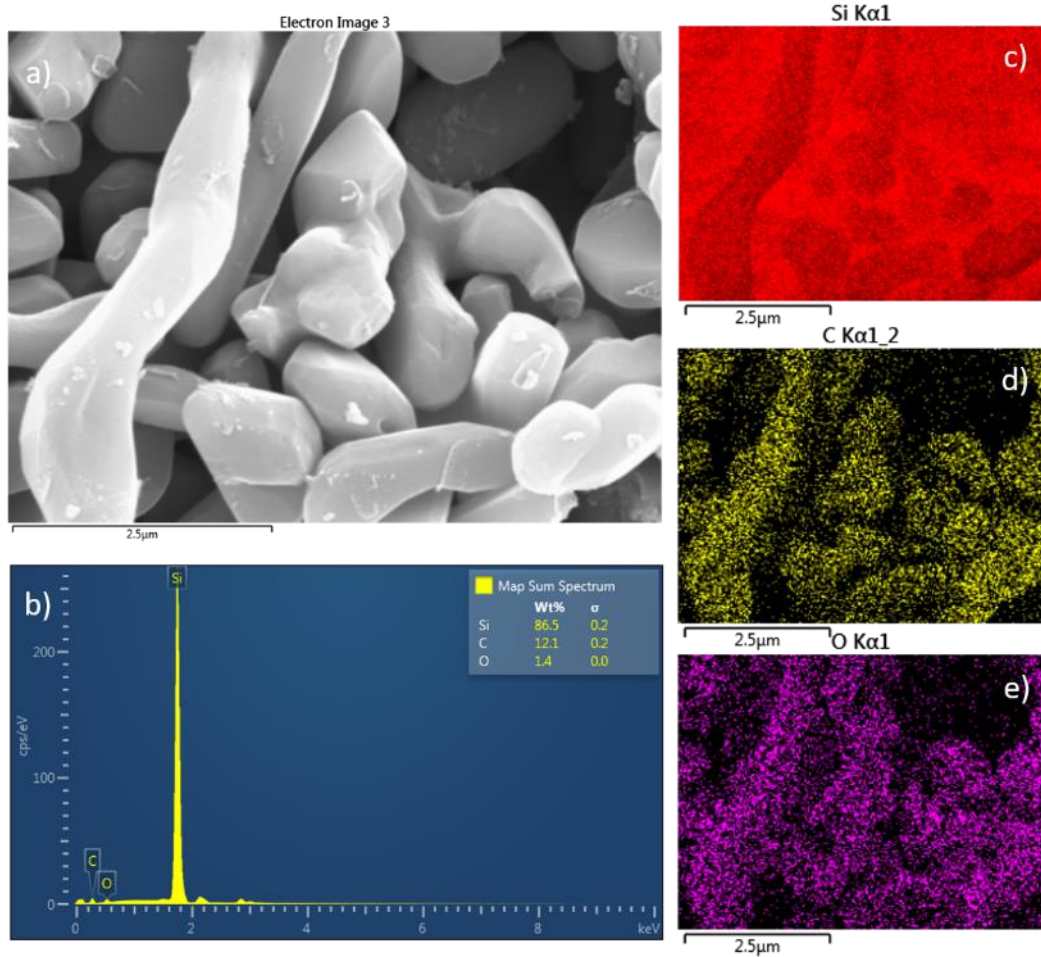
Figure 3-2: The SEM images of carbon-coated Si (a), the chemical composition by EDX (b) with element analysis and mapping for Si (c), C (d) and O (e)
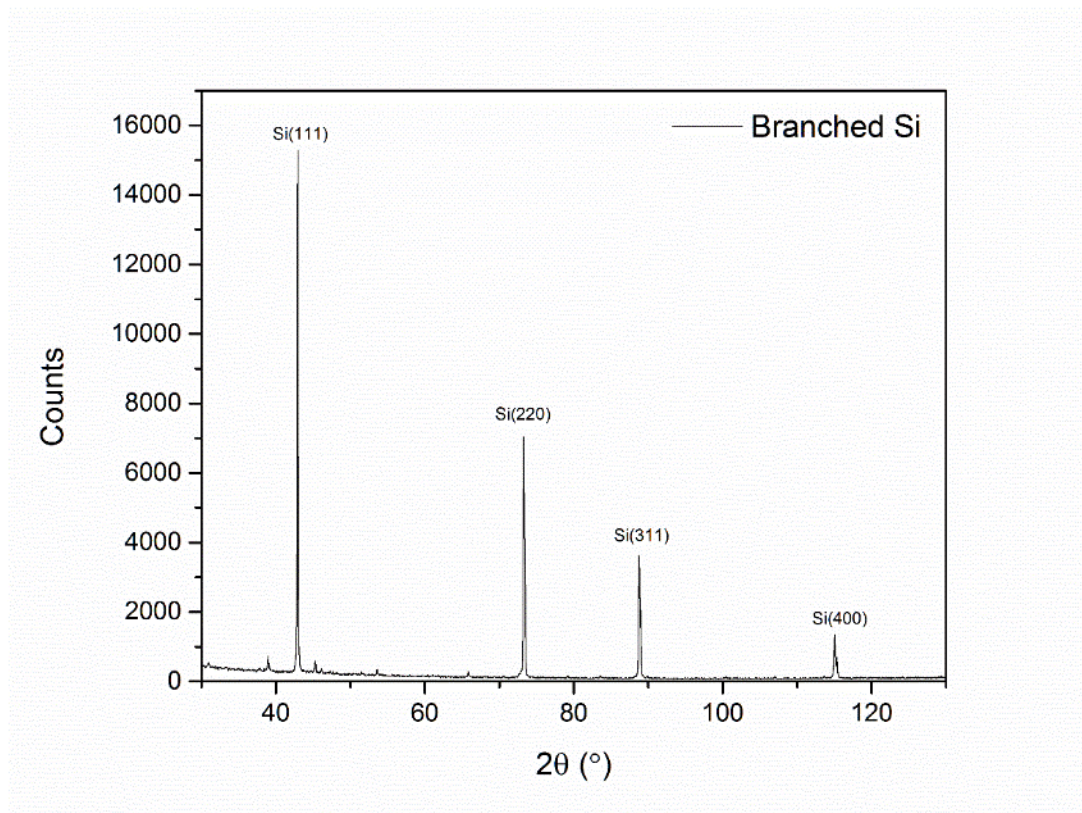
Figure 3-3: XRD analysis of carbon-coated Si powders under Cr radiation

Figure 3-3 presented the XRD pattern of pure branched Si. The characteristic peaks of eutectic Si matched the XRD database: ICDD number 01-0791. The peaks assigned to the (111), (220), (311) and (400) diffractions of Si were clearly labeled. The branched Si coated with carbon was also scanned by XRD. However, the XRD result remained the same and no peak from carbon was observed since carbon was in the amorphous form [23, 24]. The characterization peaks were strong and sharp, which indicated good crystallinity and relatively large crystal size. The carbon loading ratio in the Si/C composite was 8.7 wt% as determined by TGA.
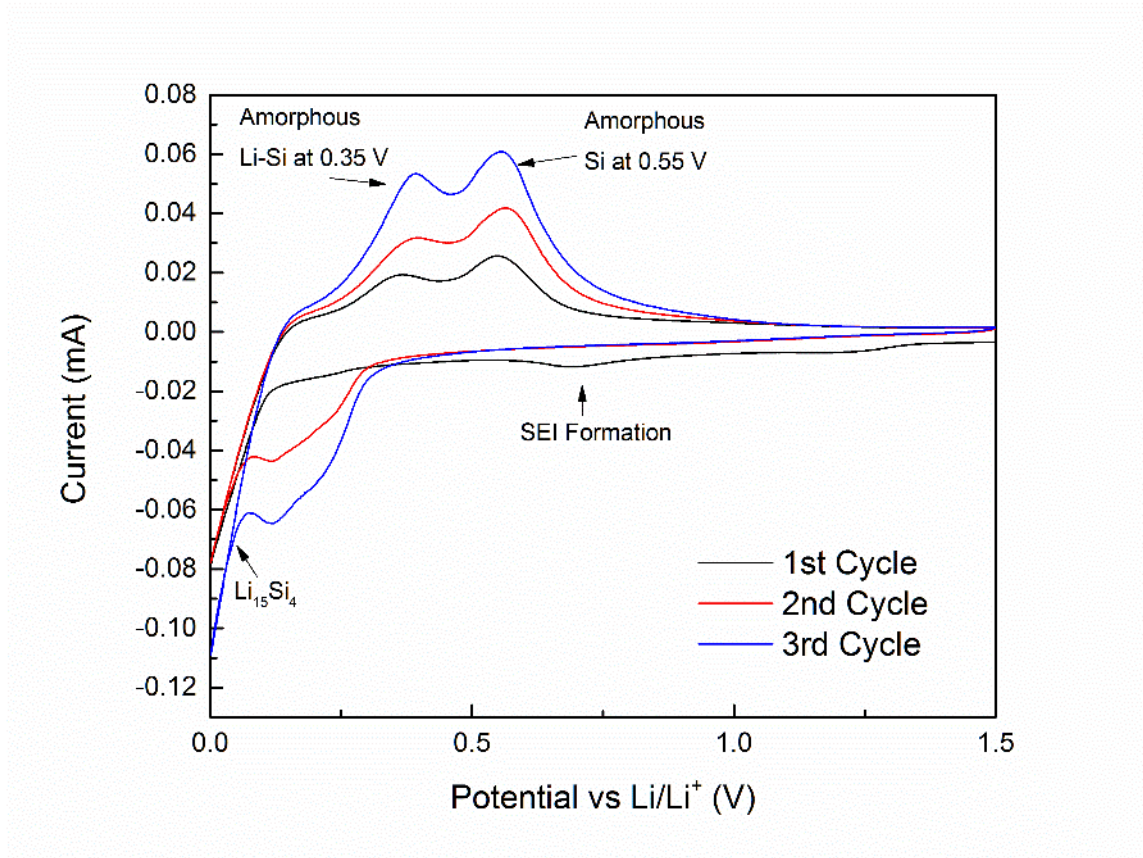
Figure 3-4: The CV profile of acquired Si/C composite at the scanning rate of 1 mV/s with range of 0-1.5 V

The electrochemical reaction of acquired Si/C was investigated by CV in Figure 3-4. In the CV plot, a small and broad peak at 0.7 V (vs. Li/Li$^+$) marked the generation of new SEI layers. This cathodic peak did not exist in the second and third lithiation processes indicating that a stable SEI layer was formed on the electrode surface during the first lithiation. At 0.2 V, the increasing cathodic current in the second and third scan was correlated to the intercalation reaction of Li in Si to form amorphous Li-Si compounds. The sharp peak at the end of the first lithiation process was when amorphous Li-Si compounds transferred into crystalline Li$_{15}$Si$_4$. During the anodic scan for delithiation process, the peaks at 0.35 V and 0.55 V were characterized as typical extractions of lithium

ions. The anodic peak at 0.35 V represented the transformation from crystalline $Li_{15}Si_4$ to amorphous Li-Si compounds. And the anodic peak at 0.55 V indicated the formation of amorphous Si. In the second and third cycles, the lithiation process was stable as there was no new phase formed. The gradually increased peak intensity indicated the activation process for Si/C composite.
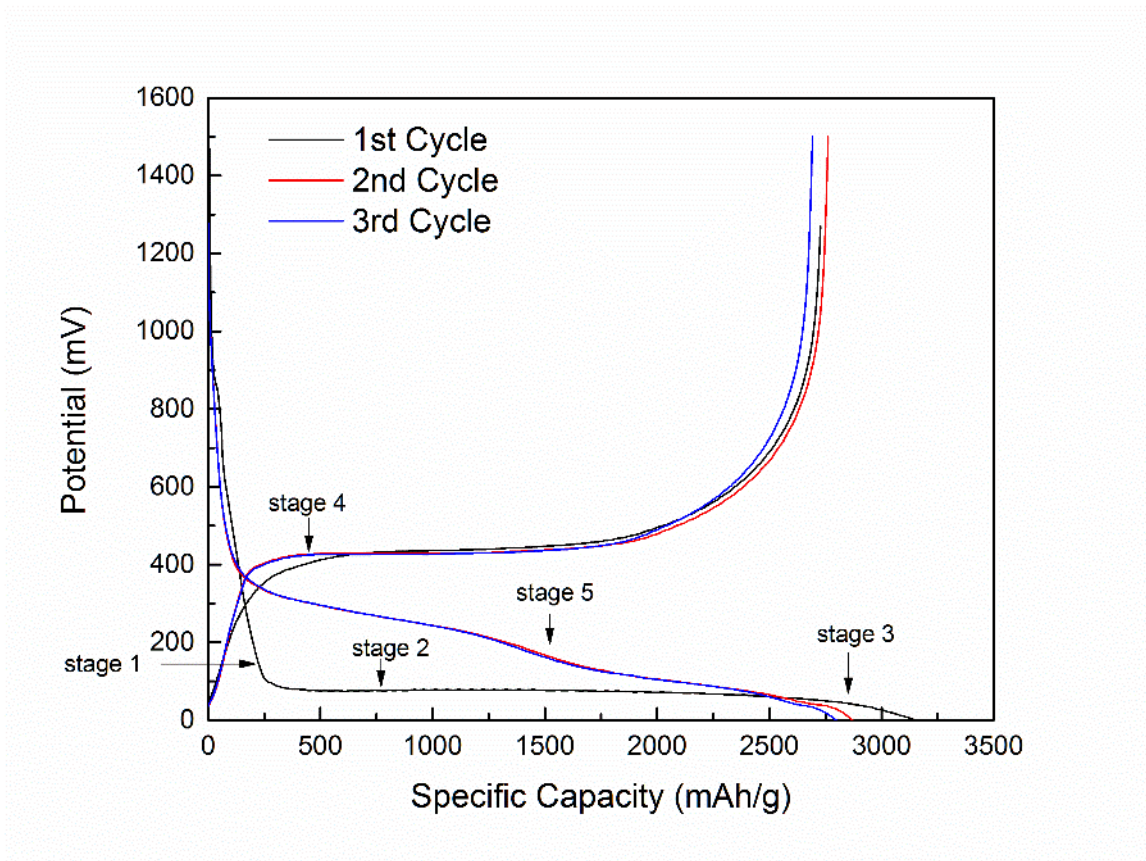
Figure 3-5: The first three charge/discharge profile of acquired Si/C composite at the current rate of 1/16C, with potential window of 0.001-1.5 V

The first three charge/discharge cycles of Si/C composite at the current rate of 1/16C were shown in Figure 3-5 with different process stages clearly labeled. During the first lithiation process, the potential dropped from open-circuit voltage all the way down to ~0.1 V (stage 1), followed by a long steady plateau (stage 2). This distinctive two-phase process

represented the continuous transformation from ordered crystalline Si to amorphous Si-Li [12]. By the end of discharge, the potential dropped from 0.07 V to 0 V representing the formation of crystalline $Li_{15}Si_4$ (stage 3). The $Li_{15}Si_4$ was a metastable phase which could only be formed at the chemical potential lower than 0.07 V during discharge. It did not exist in the binary Li-Si phase diagram [2, 25]. Only one charge plateau at 0.4 V existed in the first and following charge processes indicating that the crystalline $Li_{15}Si_4$ transferred into amorphous Si (stage 4). In the second and third discharge processes, the lithium ions directly inserted into the amorphous Si at the potential of 0.4 V (stage 5). Thus, the discharge plateau corresponding to formation of amorphous Si-Li disappeared and was replaced by a continuous decrease in potential. Similar to the first cycle, the potential dropped rapidly from 0.07 V to 0 V when crystalline $Li_{15}Si_4$ formed.

The initial specific capacity of Si at the first cycle was 3,153 mAh/g, which was close to 3,579 mAh/g, the theoretical capacity of $Li_{15}Si_4$. This high capacity can be attributed to branched micro-structure, which sufficiently facilitated lithiation and delithiation process. The specific capacities of Si in second and third discharge processes were 2,870 mAh/g and 2,797 mAh/g respectively. The columbic efficiencies were 86.8% for the first complete cycle, and 96.2% and 96.3% for the second and third cycles respectively. The commonly observed plateau at 0.5-0.8 V in discharge process of nano-sized Si anodes corresponding to the formation of SEI layer was not obvious. This phenomenon indicated that only a small amount of SEI was formed. This is an advantage of the micro-sized Si/C due to the fact that the surface to volume ratio in micro-sized Si/C was much smaller than that of nano-sized Si structure.
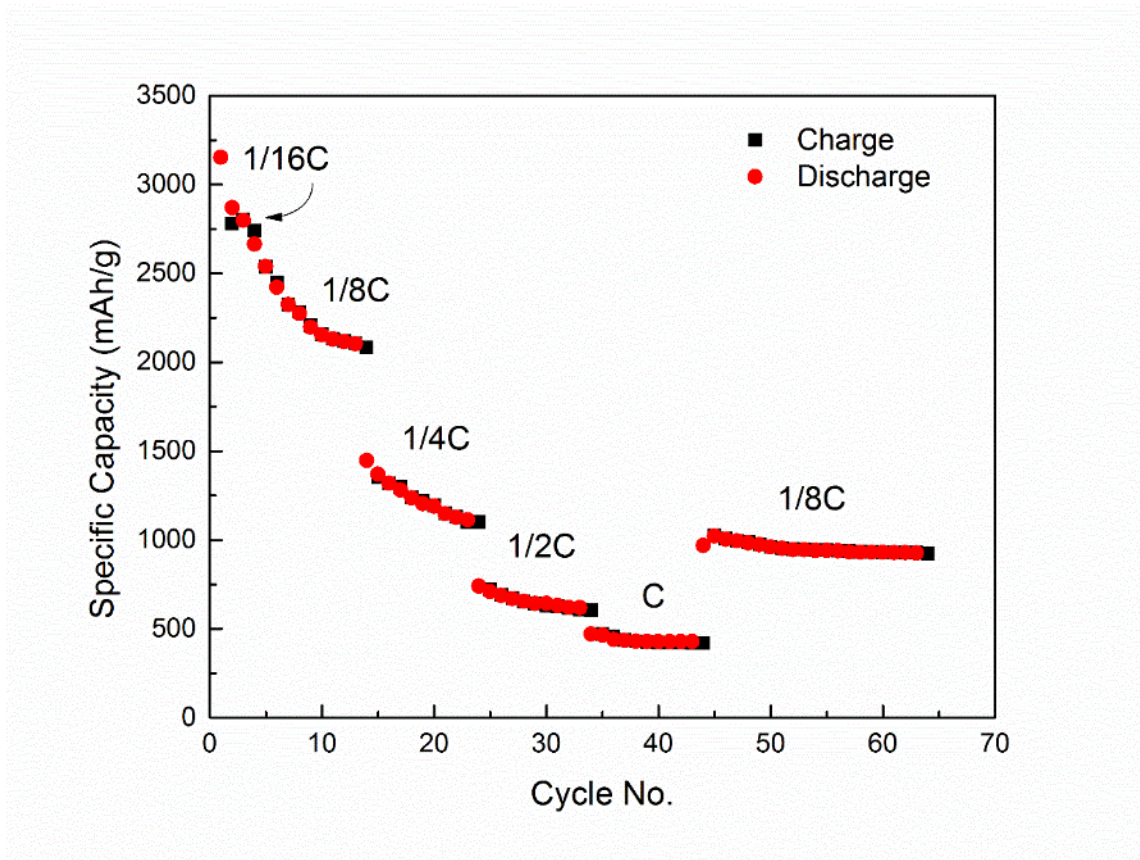
Figure 3-6: The rate performance of acquired Si/C composite in Lithium-ion batteries, with the current rate range from 1/16C, 1/8C, 1/4C, 1/2C, C and 1/8C in the end, with potential window of 0.001-1.5 V

Lithium-ion batteries made from branched micro-sized Si/C anode were cycled at 5 different charge and discharge rates: 1/16C, 1/8C, 1/4C, 1/2C and 1C. Besides the first three cycles under the rate of 1/16C, the coin cells were tested for 10 cycles at each rate. After being cycled at 1C rate, the coin cells were tested for 20 cycles at 1/8C again as shown in Figure 3-6. The Si/C composite provided relatively stable cycling performance at various current rates. The average discharge capacity was ~2,000 mAh/g at 1/8C, ~1,250 mAh/g at 1/4C, ~700 mAh/g at 1/2C and ~500 mAh/g at 1C. The lowest cycling performance of 488 mAh/g at a current rate of 1C was still higher than that of commercial graphite anode. The specific capacity recovered to above 1,000 mAh/g at 1/8C current rate after high rate cycling, which implied good cycle stability of the Si/C composite. The

discharge capacity ended with 927 mAh/g at the 20th cycle at 1/8C current rate. This could

be contributed to the unique branched structure that may provide better accommodation of

the volume expansion during lithiation/delithiation as schematically shown in Figure 3-8.
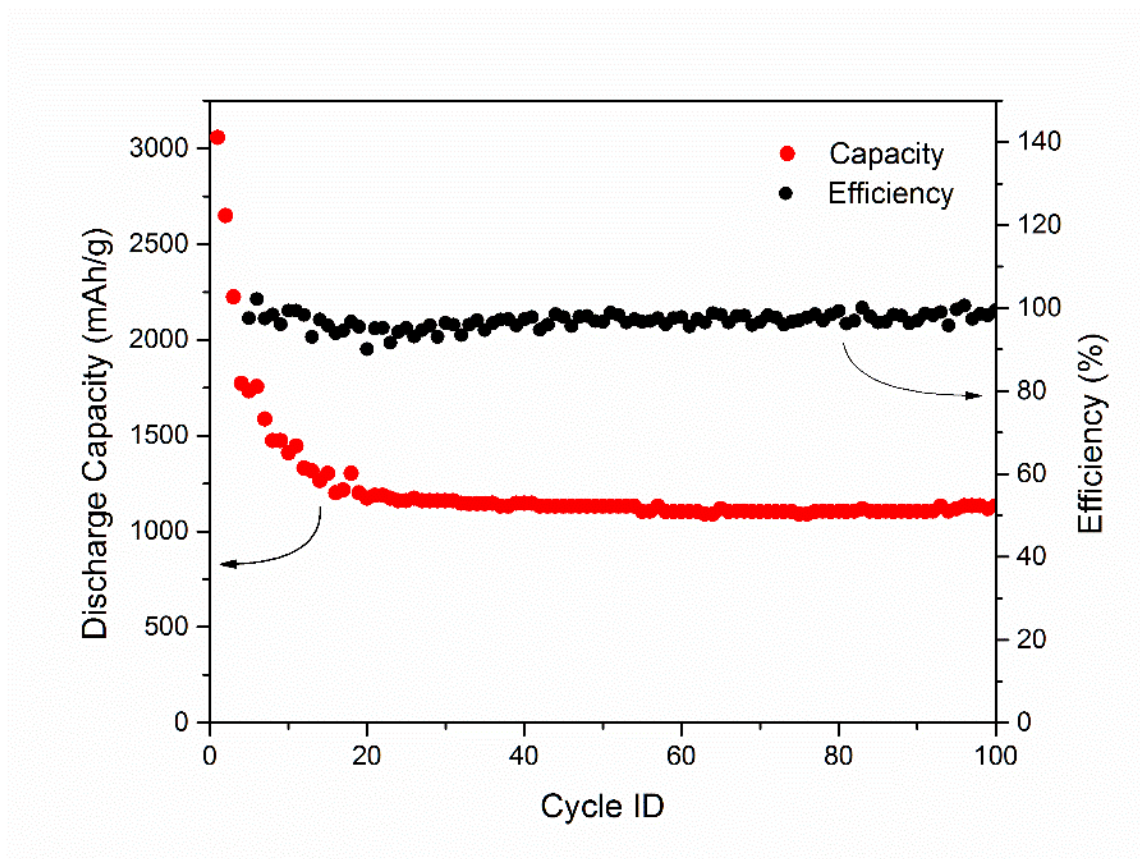
Figure 3-7: The cycling performance of acquired Si/C composite at the current density of 1/4C for 100 cycles, after initiated for the first 3 cycles at the current rate of 1/16C, with potential window of 0.001-1.5 V

The long-term electrochemical performance of branched micro-sized Si/C was shown in

Figure 3-7. The initial specific capacity at 1/16C reached 3,057.4 mAh/g. After the

initiation, the coin cells were tested for 100 cycles at 1/4C rate. A reversible discharge

capacity of 1,133 mAh/g at the current rate of 1/4C was obtained at the 100th cycle. The

comlumbic Efficiency was maintained at above 96%. It should be noted that the

electrochemical performance became stable after around 20 cycles. After the 20th cycle, a capacity decay of less than 0.2% per cycle was observed.

Figure 3-8: Illustration of branched Si during lithiation/delithiation with extra space among the branches, the size difference before and after lithiation demonstrating the actual 300 % volume expansion

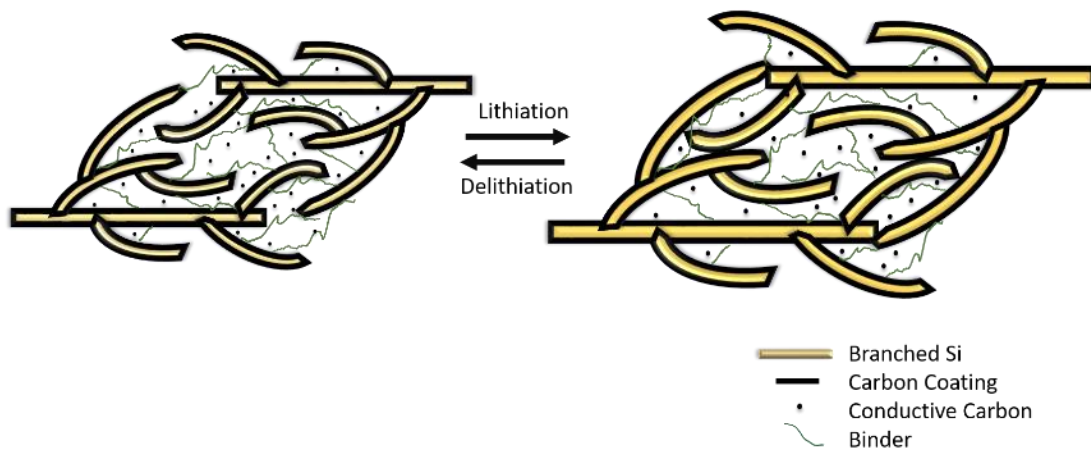In this study, branched micro-structure was observed to help improve the overall electrochemical performance of micro-sized Si anode. The stable performance of branched micro-sized Si anode could be attributed to the following reasons. It was hypothesized that the packing of branched micro-sized Si could generate void space among the branches as shown in Figure 3-8. The void space could better accommodate the Si volume expansion during lithiation/delithiation process with the help of carbon coating layer on Si surface. In addition, the hierarchical nature of the branched structure could provide increased contact with binders and conductive carbon and mitigate the capacity loss resulted from losing contact with Si which was also illustrated in Figure 3-8. The accommodation of volume expansion by void space might decrease the displacement of branched Si during lithiation/delithiation process so that the binders were able to maintain their functionality. This promising branched structural Si anode was expected to illuminate further micro-sized Si anode design, which was practical for scalable productions.

4. Conclusions

In summary, an anode based on micro-sized Si from acid-etching of casting Al-Si alloy scraps was acquired. The micro-Si possessed a unique branched structure with a diameter of 0.5-1 µm in branches, and a length of 5-10 µm. This micro-sized Si anode provided high loading ratio of active material for high power density [26]. The Si/C anode demonstrated the initial discharge capacity of 3,153 mAh/g at the current rate of 1/16C and maintained a discharge capacity of 1,133 mAh/g at the 100th cycle at the current rate of 1/4C. The capacity decay was less than 0.2% per cycle from the 20th cycle to the 100th cycle. The Si/C composite demonstrated a discharge capacity of 488 mAh/g at the current rate of 1C. After being cycled at a high rate of 1C, decreasing the current rate to 1/8 C was shown to restore the capacity to 927 mAh/g after another 20 cycles. The electrochemical performance suggested that branched micro-sized Si anode, with its advantage of low cost, easy dispersion, and immediate compatibility with the current electrode manufacturing processes, may be of interest for high capacity large scale Lithium-ion battery manufacturing. The stable electrochemical performance strongly suggests that spatial structure can be manipulated as another factor to enable microsized Si anode application.

Reference

1. Chan, C.K., et al., *High-performance lithium battery anodes using silicon nanowires.* Nature nanotechnology, 2008. **3**(1): p. 31-35.
2. Hatchard, T. and J. Dahn, *In situ XRD and electrochemical study of the reaction of lithium with amorphous silicon.* Journal of The Electrochemical Society, 2004. **151**(6): p. A838-A842.
3. Kubota, Y., et al., *Electronic structure of LiSi.* Journal of Alloys and Compounds, 2008. **458**(1): p. 151-157.
4. Boukai, A.I., et al., *Silicon nanowires as efficient thermoelectric materials.* Nature, 2008. **451**(7175): p. 168-171.
5. Eranna, G., *Crystal Growth and Evaluation of Silicon for VLSI and ULSI*. 2014: CRC Press.
6. Zhou, M., et al., *Graphene/carbon-coated Si nanoparticle hybrids as high-performance anode materials for Li-ion batteries.* ACS Appl Mater Interfaces, 2013. **5**(8): p. 3449-55.
7. Ge, M., et al., *Porous doped silicon nanowires for lithium ion battery anode with long cycle life.* Nano letters, 2012. **12**(5): p. 2318-2323.
8. Park, M.-H., et al., *Silicon nanotube battery anodes.* Nano letters, 2009. **9**(11): p. 3844-3847.
9. Cho, J., *Porous Si anode materials for lithium rechargeable batteries.* Journal of Materials Chemistry, 2010. **20**(20): p. 4009-4014.
10. Cui, L.F., et al., *Carbon-Silicon Core-Shell Nanowires as High Capacity Electrode for Lithium Ion Batteries.* Nano Letters, 2009. **9**(9): p. 3370-3374.
11. Bai, X., et al., *Si@SiOx/graphene hydrogel composite anode for lithium-ion battery.* Journal of Power Sources, 2016. **306**: p. 42-48.
12. Key, B., et al., *Real-time NMR investigations of structural changes in silicon electrodes for lithium-ion batteries.* Journal of the American Chemical Society, 2009. **131**(26): p. 9239-9249.
13. Key, B., et al., *Pair distribution function analysis and solid state NMR studies of silicon electrodes for lithium ion batteries: understanding the (de) lithiation mechanisms.* Journal of the American Chemical Society, 2010. **133**(3): p. 503-512.
14. Lin, Y.-M., et al., *High performance silicon nanoparticle anode in fluoroethylene carbonate-based electrolyte for Li-ion batteries.* Chemical communications, 2012. **48**(58): p. 7268-7270.
15. Chen, L., et al., *Effect of vinylene carbonate (VC) as electrolyte additive on electrochemical performance of Si film anode for lithium ion batteries.* Journal of Power Sources, 2007. **174**(2): p. 538-543.
16. Koo, B., et al., *A Highly Cross‑Linked Polymeric Binder for High‑Performance Silicon Negative Electrodes in Lithium Ion Batteries.* Angewandte Chemie International Edition, 2012. **51**(35): p. 8762-8767.
17. Liu, J., et al., *A high-performance alginate hydrogel binder for the Si/C anode of a Li-ion battery.* Chemical Communications, 2014. **50**(48): p. 6386-6389.
18. Yoshio, M., et al., *Carbon-coated Si as a lithium-ion battery anode material.* Journal of The Electrochemical Society, 2002. **149**(12): p. A1598-A1603.
19. Wang, C., et al., *Self-healing chemistry enables the stable operation of silicon microparticle anodes for high-energy lithium-ion batteries.* Nature chemistry, 2013. **5**(12): p. 1042-1048.
20. Yi, R., et al., *Micro‑sized Si‑C Composite with Interconnected Nanoscale Building Blocks as High‑Performance Anodes for Practical Application in Lithium‑Ion Batteries.* Advanced Energy Materials, 2013. **3**(3): p. 295-300.

21. Okada, R. and S. Iijima, *Oxidation property of silicon small particles.* Applied physics letters, 1991. **58**(15): p. 1662-1663.
22. Nymark, A.M., *Oxidation of silicon powder in humid air.* 2012.
23. Dimov, N., S. Kugino, and M. Yoshio, *Carbon-coated silicon as anode material for lithium ion batteries: advantages and limitations.* Electrochimica Acta, 2003. **48**(11): p. 1579-1587.
24. Ng, S.H., et al., *Highly Reversible Lithium Storage in Spheroidal Carbon‐Coated Silicon Nanocomposites as Anodes for Lithium‐Ion Batteries.* Angewandte Chemie International Edition, 2006. **45**(41): p. 6896-6899.
25. Li, J. and J. Dahn, *An in situ X-ray diffraction study of the reaction of Li with crystalline Si.* Journal of The Electrochemical Society, 2007. **154**(3): p. A156-A161.
26. Aifantis, K.E., S.A. Hackney, and R.V. Kumar, *High energy density lithium batteries: materials, engineering, applications*. 2010: John Wiley & Sons.

Paper 2: Effect of Particle Size and Surface Treatment on Si/Graphene Nanocomposites Lithium-Ion Battery Anodes

Yinjie Cen[a], Qingwei Qin[b], Richard D. Sisson[a], Jianyu Liang[a*]

a. Department of Mechanical Engineering, Worcester Polytechnic Institute, Worcester, MA 01609, United State
b. The Key State Laboratory of Refractories and Metallurgy, Wuhan University of Science and Technology, Wuhan, Hubei 430081, China

Abstract:

In this study, the electrochemical performance of Si particles with size ranges of 20-30 nm, 30-50 nm, ~100 nm and 1-5 µm in Si/Graphene composites were compared. Si/graphene composites were fabricated by static force. Silane agent was introduced to Si surface to render positive charges and was subsequently bonded with graphene oxide (GO) possessing negative surface charges. The following reduction resulted in Si/Graphene (Si/G) composites. It was found that the piranha pre-treatment before introduction of silane agent provided more stable cycling performance for all sizes tested. This effect may be attributed to stronger bonding between Si particles and GO that led to more stable Si/graphene structure. The 100 nm Si/Graphene samples with piranha treatment demonstrated the highest discharge capacity of 1,561 mAh/g after 100 cycles at a current density of 0.5 C. It showed higher discharge capacity compared with the 30-50 nm sample and 20-30 nm sample at discharge rates ranging from 0.1 C to 1 C. 30-50 nm sample with piranha treatment demonstrated the least capacity retention of 80% in long term cycling tests.

1. Introduction

High capacity electrode materials are needed for Lithium-ion batteries (LIBs) due to the increasing demand of high power and energy density for high performance devices, energy storage packages and electric vehicles (EV). Si with theoretical capacity of 3,579 mAh/g, which is almost 10 times of that of conventionally used graphite, is an attractive material for anode in LIBs. However, the severe capacity loss remains as a challenge preventing the large scale use of Si in LIBs. The severe capacity loss is resulted from the 300% volume expansion during lithiation/delithiation process [1, 2]; and the continuous growth of solid electrolyte interphase (SEI) on Si surface [3, 4].

To mitigate the above challenges, Si nanostructures, including nanowires [5, 6], nanotubes [7], nanoparticles [1, 8] and nanopores [9, 10], have been vigorously studied and have demonstrated improved electrochemical performance compared with Si microstructures. In addition to employing Si nanostructures, carbon coating is necessary in constructing working Si electrodes. Carbon coating not only provides contact with Si particles to ensure electro-conductivity, but also prevents the direct contact of Si with electrolyte and the formation of thick SEI. Among various carbon coatings, Si/Graphene composites have drawn much attention. Many facile fabrication routines, such as mechanical mixing [5, 6], pyrolyzed PANI functionalized assembly [7] and amide functional group self-assembly [8, 9] resulted in various Si-Graphene assembles.

However, there is no apparent trend or rule that can guide the design of Si nanostructured electrode fabrication to achieve stable outstanding electrochemical performance. For example, there is no conclusion on optimal particle size, though particles of size smaller than 150 nm are mostly used. This may have been influenced by the work of Liu, Zhu and

Huang et al [10, 11] as they have observed a strong dependence of Si particle fracture on the particle size. Si particles larger than 150 nm tend to crack into pieces during lithiaion/delithiaion cycling. Some of the small cracked pieces may detach from conductor and stop participating in electrochemical reactions. This could result in fast deteriorating capacity.

Wu et al investigated the effect of Si particle size in micrometer range in 2005 [12]. In their study, 3 µm Si particles outperformed the 20 µm ones with an initial capacity of 800 mAh/g and a retention of 600 mAh/g after 50 cycles. Cho et al studied the effect of Si particle size in 5-20 nm range in 2010 [13]. The 10 nm Si presented highest charge capacity, they exhibited lower Coulombic efficiency than 20 nm sized n-Si and a low capacity retention of 81%. In both works carbon coating were applied. However, the particle size effect in Si/Graphene composites has not been studied systematically. A comprehensive literature review of Si/Graphene composite anode was conducted and some representative results are summarized in Table 3-2, in which the Si and graphene assembly method, initial capacity and the capacity at the 100th cycle were compared. We found that the size effect of Si/Graphene composites could not be determined by literature review only as they were strongly affected by fabrication methods and processing details. Si/Graphene composites with similar structures could present very different electrochemical performance due to different process details.

In this work, experimental study was carried out on fabricating Si/Graphene composites with Si particle sizes of 20-30 nm, 30-50 nm, 100 nm, and 1-5 µm. The Si/Graphene composites were obtained by static-assembling process of Si with GO. Pretreatment of Si surface with piranha was conducted to improve bonding between Si and graphene and was

shown to improve the overall electrochemical performance. The electrochemical performance was tested by coin cells. The 100 nm Si/Graphene nanocomposites had the highest initial capacity of 2,737 mAh/g at the current rate of 0.1C and the highest discharge capacity of 1,561 mAh/g after 100 cycles at the current density of 0.5C. The 30-50 nm Si/Graphene nanocomposites treated with piranha solution exhibited the most stable cycling performance, retaining 89.1% of the initial capacity at the 100th cycle of ~1360 mAh/g.

Table 3-2: A literature review of Si/Graphene composite anode

Si Source with Ref.	Graphene Synthesis Method	Graphene Weight Ratio	Si particle size	Initial Reversible Capacity	First Cycle Efficiency	Best capacity retention at the 100th cycle with current rate	Capacity retention at the 100th cycle
Si NPs [5]	Graphite Oxidation + H_2 Reduction	~40%	~20 nm	~2,050 mAh/g	~96%	~1,000 mAh/g 1,000 mA/g	52.6%
Si NPs [14]	Modified Hummer's Method + Hydrazine Reduction	73.6%	3-80 nm	~2,400 mAh/g	~41%	~708 mAh/g 50 mA/g	64.4%
Si NPs [15]	Hummers Method + Thermal Reduction	66.7%	50-100 nm	1,040 mAh/g	63%	~800 mAh/g 50 mA/g	72.7%
Si NPs [16]	Thermal Expansion	~33%	50 nm	2,753 mAh/g	~80%	30th, ~2,400 mAh/g 300 mA/g	68.6%
Aerosol Droplets Si NPs [17]	Crumpled Reduction	40%	50-100 nm	1,175 mAh/g	~95%	~1,000 mAh/g 1,000 mA/g	86.5%
3-D Porous Si by Magnesiothermic Reduction [18]	Hummer's Method + Thermal Reduction	~40%	30-50 nm	1,100 mAh/g	~79%	~400 mAh/g 5,000 mA/g charge 100 mA/g discharge	50%
Si NPs on Ultrathin-graphite Foam [19]	Hummer's Method + Thermal Reduction	15.1%	~100 nm	1,000 mAh/g	62.5%	~400 mAh/g 400 mA/g	~37.2%
Si NPs on 3-D tree-like GNS [20]	Microwave Plasma CVD	19%	~20 nm	2,731 mAh/g	~56%	1,400 mAh/g 150 mA/g	86.7%
(PANI)-Si NPs [7]	Modified Hummer's Method + Pyrolysis Method	26%	50 nm	~1,500 mAh/g	~70%	1,000 mAh/g 2,000 mA/g	80%

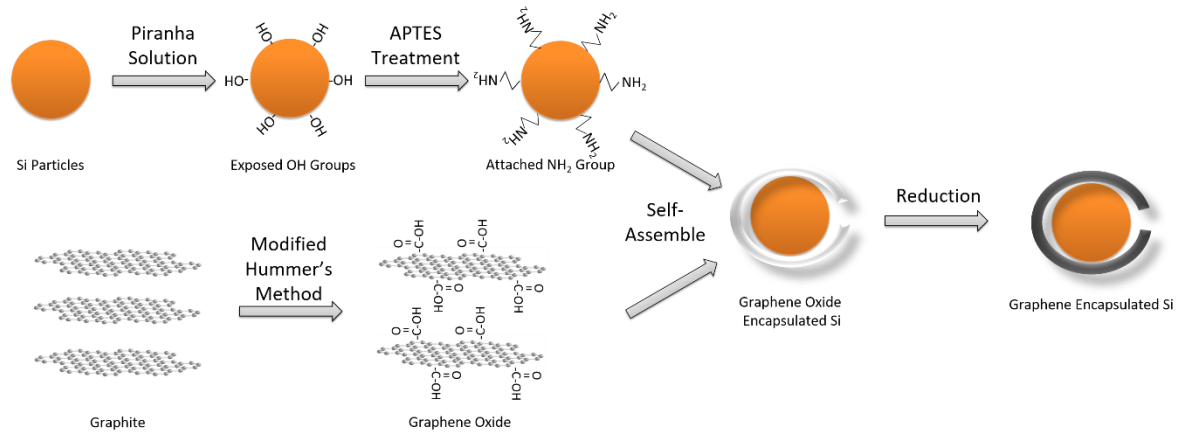| Amino benzoyl acid treated Si NPs [9]	Modified Hummer's Method + Thermal Reduction	32.7%	100-150 nm	1,100 mAh/g	73%	1,250 mAh/g 200 mA/g	78.8%
Si NPs on Graphene Hydrogel [21]	Modified Hummer's Method + Ascorbic Acid + Thermal Reduction	29%	50 nm	2,250 mAh/g	53%	1,800 mAh/g 100 mA/g	~60%

2. Experiments

Figure 3-9: Schematic illustration of procedure to synthesize Si/Graphene composites

Figure 3-9 illustrated the process of fabricating the Si/Graphene composites. The Si particles were first modified by piranha solution to expose the hydroxyl groups on the surface of Si particles. Then the hydrolysis reaction happened between APTES and –OH exposed Si particle surface to attach the –NH_2 groups for positive charged Si particles. Graphene oxide was synthesized by modified Hummer's method starting from graphite flakes. The GO were oxidized with –COOH functional groups thus resulted in negative polarity. The Si/Graphene Oxide composites were assembled by static electric attractive force. At last the assembled Si/Graphene Oxide composites were reduced to obtain Si/Graphene composites.

In this work, four different Si particle sizes were studied: 20-30 nm Si (98%+, 20-30 nm, Nanoamor), 30-50 nm Si (98+%, 30-50 nm, Nanoamor, Inc), ~100 nm Si (99%, 100 nm, MTI) and 1-5 µm Si (99.9%, 1-5 µm, Alfa Aesar). The Si/Graphene composites were named as nSi25/G, nSi40/G, nSi100/G and mSi/G respectively. The Si/Graphene treated

by piranha solution were named as nSi25/G_p, nSi40/G_p, nSi100/G_p and mSi/G_p respectively.

Synthesis of Graphene Oxide

Graphene Oxide (GO) was synthesized by adapting a reported modified Hummers method [22]. A mixture of concentrated H_2SO_4 (95-98%, Alfa Aesar) and H_3PO_4 (85%, Alfa Aesar) with volume ratio of 9:1 was added to a mixture of natural graphite flakes (99.9%, Alfa Aesar) and $KMnO_4$ (>99%, Sigma Aldrich). The reaction was then heated to 50 °C and stirred for 24 h. Finally, the reaction was cooled to room temperature and poured onto ice cubes with H_2O_2 (30%, Sigma Aldrich) to form a stable bright yellow suspension. The prepared GO was ultrasonically dispersed into Deionized Water (DI Water) to obtain GO hydrosol (0.02 g/ml).

Surface Treatment of Si

The Si particles were immersed in the freshly made piranha solution ($H_2SO_4/H_2O_2 = 3:1$ v/v) for 1 h at 80 °C to introduce hydroxyl groups on the surface. They were then washed thoroughly with large amount of DI water and ethanol separately, followed with filtration. The OH-treated Si particles were transferred into a 1 wt% methanol solution of (3-aminopropyl)triethoxysilane (APTES, 99%, Sigma Aldrich) and stirred for 12 hours to obtain -NH_2 functionalized Si particles. The suspension was flited and washed, then dried in a vacuum oven at 80 °C overnight. Another group of Si particles without piranha solution pretreatment were also prepared for comparison.

Fabrication of Si/G composites

The Si particles were dispersed in N, N-dimethyloformamide (DMF, 99%, Sigma-Aldrich) by sonication until a homogenous yellow suspension was formed. GO hydrosol was then introduced and sonicated for another 2 hours. Next, hydrazine (anhydrous, 98%, Sigma-Aldrich) was slowly added under nitrogen (N_2, UHP, Airgas) protection. The reaction was kept at 95 °C for overnight. The resultant black particles were collected by centrifuging and washed with ethanol. Finally, the as-made composites were dried in the vacuum oven for 12 hours to obtain the final Si/G composites.

Characterization

The powder tapped density was carried out by vertically tapping powders in the 100 ml graduated cylinder for 10, 500, and 1,250 times then measuring the final volumes. The surface area of selected Si particles was measured by Brunauer–Emmett–Teller (BET) gas absorption method (Micromeritics ASAP 2020). The morphology of bare Si particles, Si/G composites and graphene nanosheets was investigated by Scanning Electron Microscopy (SEM, JOEL 7000F). The actual graphene loading ratio was measured by Thermogravimetric Analyzer (TGA Q50, TA instruments). Crystallographic information of the samples was investigated with X-Ray Diffraction (XRD, Cr Kα radiation at λ=2.23 Å, PANALYTICAL EMPYREAN). Raman Spectrum (Horiba, XploRA One, 532 nm green laser) was performed to characterize the reduced graphene. Zeta potential was measured by Zetasizer Nano ZS90 (Malvern) to confirm the surface charge of GO and modified Si.

Electrochemical Tests

The electrochemical tests were conducted by using a half-coin cell setup. For preparation of testing electrode, pure Si, Si/G composites without piranha treatment and Si/G composites with piranha treatment of different particle sizes were individually mixed with acetylene black (MTI) and water based binder at a weight ratio of 70:15:15, respectively. The binder was prepared by dissolving carboxymethyl cellulose (CMC, MTI) and Styrene-Butadiene Rubber (SBR) in the water. The electrode mixture was casted onto the Cu foil and dried at 60 °C for 12 h, then cut into round disks with a diameter of 11.99 mm. The disks were degassed in vacuum furnace at 120 °C for 8 h. The CR2032 coin cells were assembled in a glove box with Lithium foil as counter electrode. The electrolyte was 1 M LiPF6 dissolved in a mixed solution of diethyl carbonate (DEC) and ethyl carbonate (EC) with 1:1 vol ratio with 2 wt% fluoroethylene carbonate (FEC, 99%, Sigma-Aldrich) as additive. The electric performance was tested between 0.001 and 1.5 V at different current rates. The charge/discharge current rates were calculated based on the theoretical capacity of lithiated $Li_{15}Si_4$ at 3,579 mAh/g [23].

3. Results and Discussion

Table 3-3: Tapped density and specific surface area of selected Si particles in different size

Si particle size	Tapped Density	Specific Surface Area
20-30 nm	0.09 g/cm^3	106.621 m^2/g
30-50 nm	0.16 g/cm^3	78.274 m^2/g
~100 nm	0.75 g/cm^3	30.925 m^2/g
1-5 μm	1.14 g/cm^3	2.672 m^2/g

Table 3-3 listed the tapped density and specific surface area of Si particles. The tapped density increased with increasing in Si particle size. 25 nm Si particles had a tapped density of 0.09 g/cm^3 while Si particles ranged in 1-5 μm had a tapped density of 1.14 g/cm^3. A higher tapped density might lead to a higher loading weight of active materials since the thickness of casted electrode on current collector tended to be constant. Meanwhile, 25 nm Si particles possessed the highest specific surface area of 106.6 m^2/g, which agreed with other reported measured Si nanoparticle surface area [24]. In LIBs, the larger specific surface area could provide a shorter lithium ion pathway during charge/discharge to enhance the electrochemical performance. However, the large specific surface area could also mean large consumption of electrolyte in forming SEI layer. Comparing 25 nm and 100 nm Si particles, while the surface area of the 25 nm Si more than doubled that of 100 nm Si, the tapped density was only about 1/8 of the latter. Meanwhile, extra effort might be needed to ensure good dispersing of smaller nanoparticles. Thus, when the electrochemical performance was similar, 100 nm Si may be a sensible materials for LIBs.
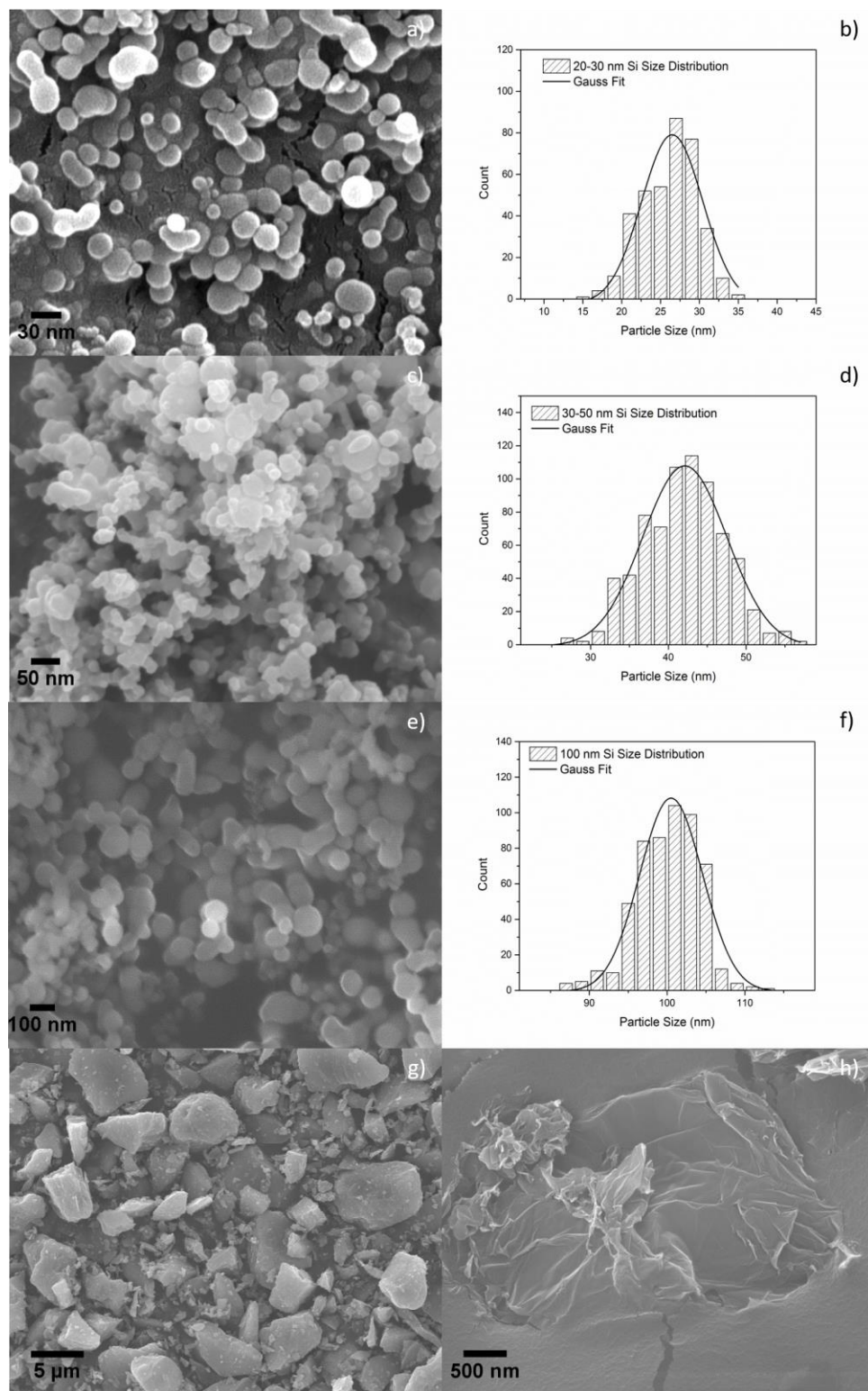
Figure 3-10: The morphology of selected Si particles in SEM: a) 25 nm Si, c) 40 nm Si, e) 100 nm Si, g) 1-5 µm Si and the corresponding particle size distribution for 25 nm Si in b), 40 nm Si in d) and 100 nm Si in f); The SEM of Graphene nanosheets also given in h).

The morphology of Si particles were shown in Figure 3-10 a), c), e) and f). The SEM images and the corresponding size distribution charts for nanosized Si particles confirmed the size and shape of Si powders, with the 25 nm, 40 nm and 100 nm being sphere and 1-5 µm particles being coarse flakes. The morphology of graphene nanosheets was given in Figure h). The graphene had a unique wrinkling and folded surface morphology, which provided large surface area for anchoring Si particles.
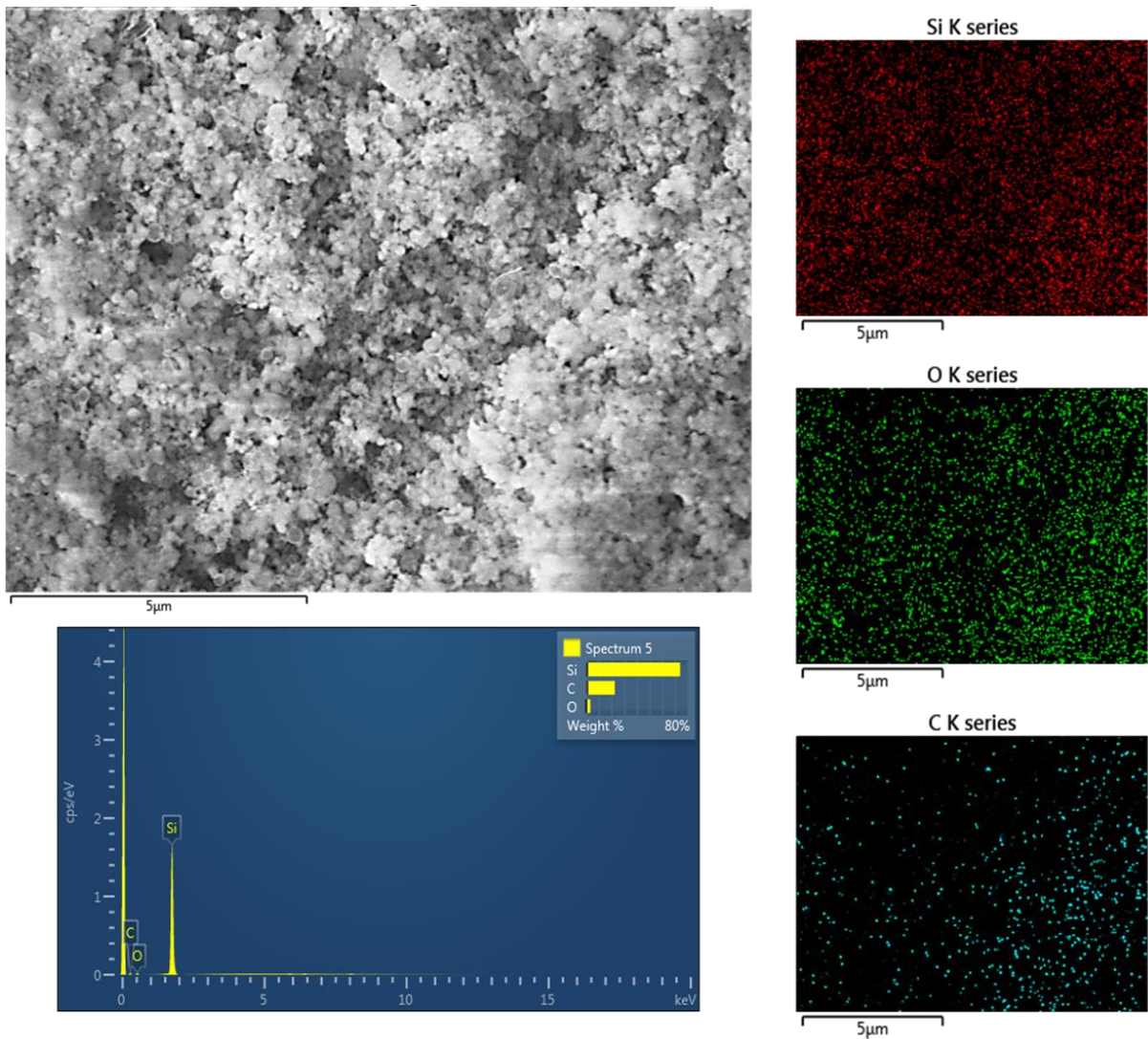

Figure 3-11: The EDX mapping of 100 nm Si/Graphene nanocomposites; Left: Detected area in SEM image with element spectrum; Right: Element signal map (Silicon K series in RED, Oxygen K series in GREEN and Carbon K series in light blue)

The EDX scan of Si/Graphene composites showed similar uniform distribution of Si, C and O across the surface of all samples. Figure 3-11 represented the typical observed element mapping. The oxygen content was mainly attributed to the thin SiO_2 layer, which was highly desired in fabrication of Si/Graphene composites. It should be noted that the EDX data does not provide accurate quantitative result.
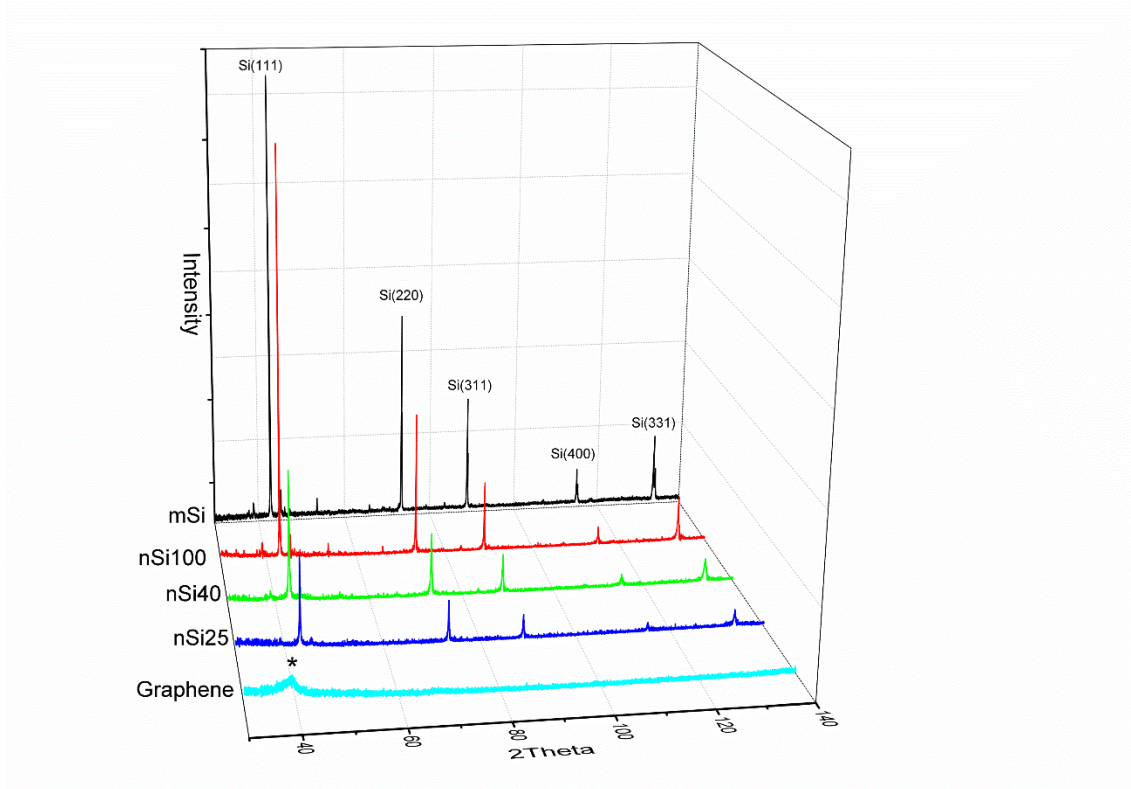

Figure 3-12: XRD patterns of Graphene nanosheets and selected Si particles with mSi in black, nSi100 in red, nSi40 in green, and nSi25 in blue

The crystalline structure of graphene and Si/Graphene were analyzed by X-ray diffraction (XRD) as shown in Figure 3-12. XRD specturm of all Si/Graphene samples were all most identical, showing the presence of pure silicon phases and trace of graphene characterization peak as labeled with *. The characterization peaks at 42.965°, 73.319°, 88.812°, 115.038° and 133.581° could be assgined to the (111), (220), (311), (400) and (311) differactions of Si (XRD database: ICDD number 01-0791) respectively. These

peaks were observed in all Si particles with different size. The XRD pattern from microsize Si particles demostrated the highest intensity, and the sharpest peaks among all four Si samples, which were caused by the high degree of crystallinty. With the decreasing of the Si particle size, the peak intensities of nanosized Si particle decreased and the width of the characterizaion peaks broadened. This result could be explained by small crystalline domain in nanosize Si particles. The actual crystalline size could be calculated by Scherer's equation as $d = \frac{0.9\lambda_{K\alpha}}{B_{2\theta} \times \cos\theta}$, in which $\lambda_{K\alpha}$ was wavelength of X-Ray ($\lambda_{K\alpha} = 0.223$ nm), θ is the peak angle, and $B_{2\theta}$ was the full width half maximum in radians. The mean Si crystalline size were 119.8 nm, 70.1 nm, 37.7 nm and 20.6 nm for Si particles size of 1 µm, 100 nm, 30-50 nm and 20-30 nm respectively. It should be noticed that the crystalline size was not equaled to the particle size.
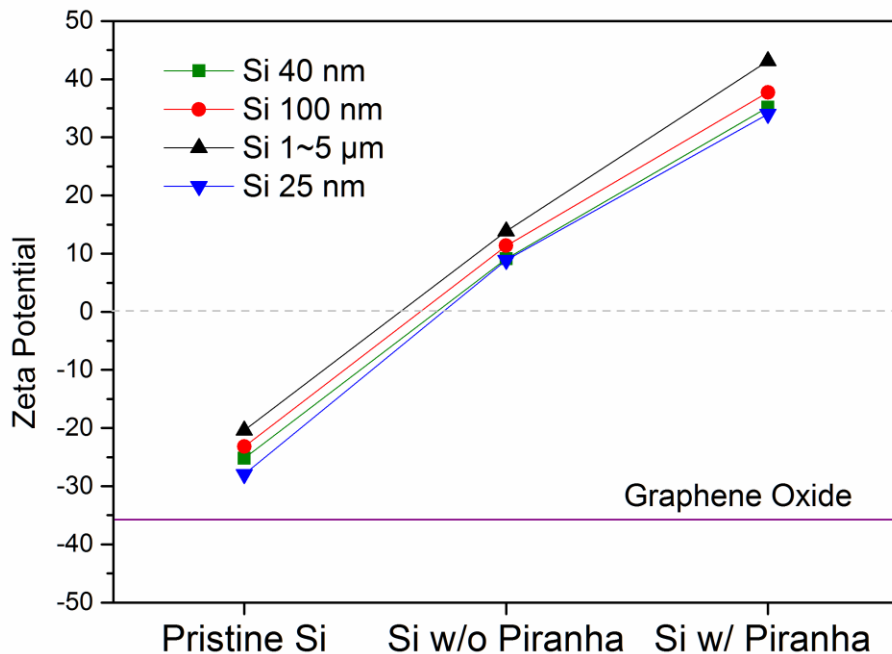
Zeta potential is the electro kinetic potential existing in the interfacial double layer (DL) at the shear plane of the particles. It is an efficient technique to determine the surface charge of modified particles, in the form of the potential difference between the dispersion medium and stationary layer of attached dispersed particles. In this measurement, low concentration (1 mg/ml) particles were dispersed in DI water. Pristine Si particles, NH_2-decorated Si without piranha solution treatment, and NH_2-decorated Si particles with piranha solution treatment of three sizes were examined. The zeta potential results in Figure 3-13 confirmed that pristine Si particles had negative surface charge with zeta potential of -27.94 mV, -25.18 mV, -23.20 mV and -20.42 mV for 25 nm, 40 nm, 100 nm and 1-5 µm particles respectively. The negative charge might have originated from the SiO_2 layer on the surface. This observation agreed well with other fundamental studies of SiO_2 surface charge [16]. Zeta potential confirmed that surface charges of Si particles were converted from negative to positive by treating the surface with APTES without piranha pretreatment. However, when piranha treatment was added, the zeta potentials of all samples decorated by APTES treatment were further elevated to 34.01 mV, 35.19 mV, 37.73 mV and 43.16 mV for 25 nm, 40 nm Si, 100 nm Si and 1-5 µm Si respectively. The piranha solution treatment ensured that the particle surface was clean, hydrophilic and having exposed -OH group on the surface for further amide functionalization. This zeta potential increase could be attributed to increased –OH groups on the particle surface after piranha treatment which could lead to increased amount of –NH_2 groups being attached. The APTES could bind to the exposed-OH groups on the surface of Si particles by hydrolysis reaction, while

presenting free –NH$_2$ groups for further assembling. Thus, Piranha pretreatment resulted in higher positive zeta potential and led to stronger static bonding of Si particle with negatively charged GO with a zeta potential at -35.78 mV.

Table 3-4: TGA analysis of graphene loading ratio for selected Si particles

	Graphene Loading Ratio by TGA	
	Without Piranha Solution	With Piranha Solution
Si 20-30 nm	8.3 wt%	8.5 wt%
Si 30-50 nm	8.7 wt%	8.8 wt%
Si 100 nm	9.1 wt%	9.6 wt%
Si 1-5 μm	9.3 wt%	9.6 wt%

The graphene loading ratio were measured by TGA method, and summarized in Table 3-4. The targeted loading ratio is 10 wt%. In the TGA test, all samples were tested from room temperature to 700 °C at a heating rate of 10 °C/min. The actual graphene loading ratio was close to the targeted 10 wt% in all samples.
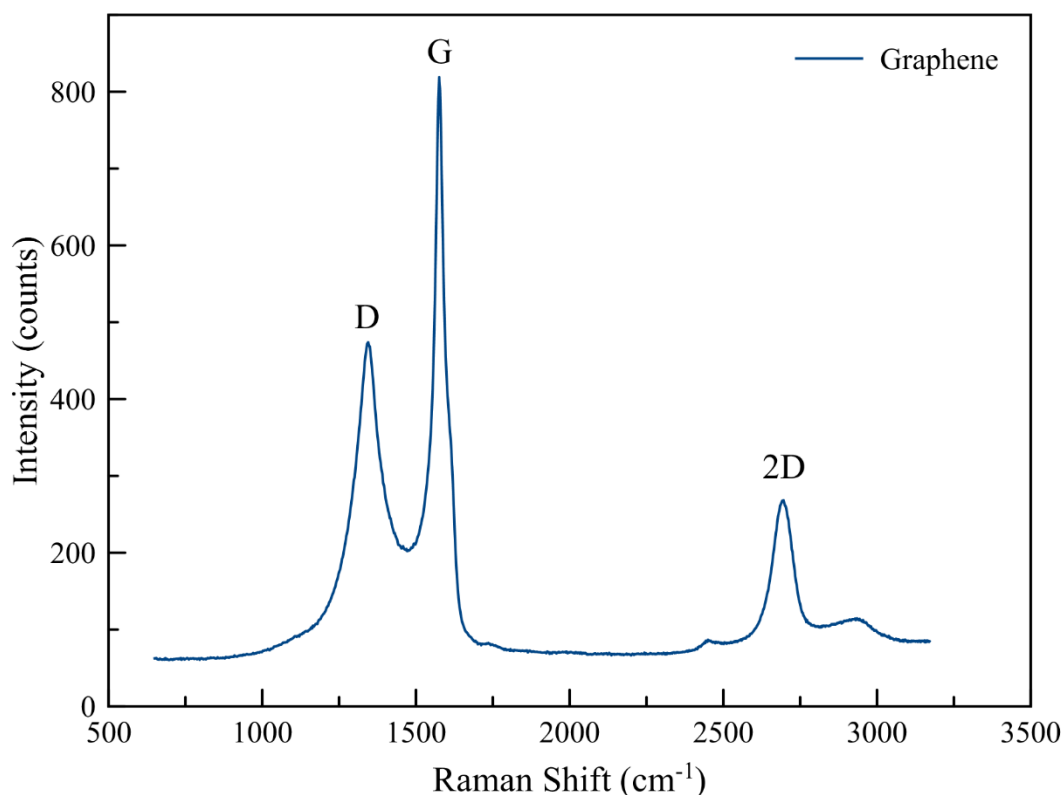
Figure 3-14: Raman Spectrum of synthesized graphene with 532 nm green laser

Structural information of synthesized graphene such as the number of stacking layers and defect density were characterized by Raman spectroscopy [25]. The Raman spectrum of reduced graphene nanosheets were shown in Figure 3-14. D band (at around 1350 cm^{-1}) indicated the out of plane vibrations attributed to the presence of structural defects. G band (at around 1580 cm^{-1}) stood for C=C bond stretching of all pairs of sp^2 atoms. 2D band (at around 2700 cm^{-1}) was caused by the double resonance process. The intensity of 2D band and its symmetrical shape were widely used to characterize the layered graphene structure. The graphene sample presented a 2D band at 2695 cm^{-1} with a symmetrical peak from the scatted electron by two phonons. The full width at half maximum (FWHM) of graphene sample is ~59 cm^{-1}. Typically, the smaller the FWHM was, the higher the quality of single

layered graphene structure. Another characteristic peak for graphene in Raman spectrum

was the D band around 1346 cm^{-1}. It had been proven that the higher the value of I_D/I_G the

smaller the crystallite size and the smaller the defects distance. The I_D/I_G of reduced

graphene was 0.81, which indicated a graphene-like structure with approximately size of

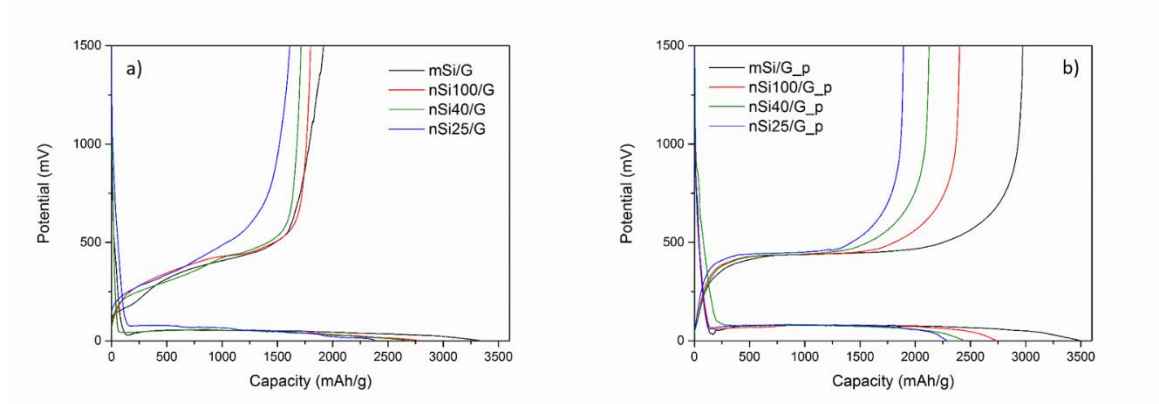9000 carbon atoms and defects distance of 17 nm [26].

Figure 3-15: The initial charge/discharge curves of 1-5 µm Si/Graphene composites, 100 nm Si/Graphene nanocomposites, 40 nm Si/Graphene nanocomposites and 25 nm Si/Graphene nanocomposites without piranha treatment a) and with piranha treatment b) under current rate of 0.05C

Figure 3-15 showed the initial charge/discharge curves of 1-5 µm Si/Graphene composites,

100 nm Si/Graphene nanocomposites, 40 nm Si/Graphene nanocomposites and 25 nm

Si/Graphene nanocomposites without piranha treatment (Figure 3-15 (a)) and with piranha

treatment (Figure 3-15 (b)) at the current rate of 0.05C. All samples demonstrated typical

charge/discharge behaviors of Si anode. During the first lithiation process, the potential

dropped all the way down to ~100 mV followed by a long steady plateau. This distinctive

two-phase process represented the continual transformation from ordered crystalline Si to

amorphous Si [27]. By the end of discharge, the potential dropped abruptly at 70 mV where

crystalline Li$_{15}$Si$_4$ formed. The Li$_{15}$Si$_4$ was a metastable phase which could only be found

at the last stage of the discharge process. It did not exist in the binary Li-Si phase diagram

[28, 29]. Only one charge plateau at 400 mV was observed in each charge curve indicating that the crystalline Si transferred into amorphous Si. In the second discharge processes, the lithium ions directly inserted into the amorphous Si at the potential of 400 mV resulting in a discharge potential decreasing with a steady slope. Similar to the first discharge, the potential dropped at 70 mV where the crystalline $Li_{15}Si_4$ appeared. The cut-off of 1 mV was where all the Si was transferred to $Li_{15}Si_4$ phase.

The initial specific capacity of Si/G particles in first cycle were 3,345 mAh/g for mSi/G, 2,793 mAh/g for nSi100/G, 2,697 mAh/g for nSi40/G and 2,603 mAh/g for nSi25/G. With pretreatment by piranha solution, the initial specific capacity of Si/G particles in first cycle were 3,497 mAh/g for mSi/G_p, 2,737 mAh/g for nSi100/G_p, 2,445 mAh/g for nSi40/G_p and 2,287 mAh/g for nSi25/G_p. There was no significant change before and after piranha treatment for the initial performance at low current rate (0.05C). The particle size demonstrated a more pronounced influence on the electrochemical performance. For both micro sized Si particle mSi/G and mSi/G_p, their initial specific capacities were very close to 3,579 mAh/g, the theoretical capacity of $Li_{15}Si_4$. Comparing the electrochemical performance of Si/G nanocomposites with or without piranha treatment, it was noted that the capacity decay was less pronounced in samples with piranha pretreatment. As indicated by zeta potential data, piranha treatment might have resulted in a strong attraction between Si nanoparticles and graphene oxide with the matching amount of opposite surface charge. This strong attraction might have led to strong attachment between final Si and graphene product. This better contact with graphene might help explain the more stable plateau observed at the chemical potential of ~400 mV, in piranha treated samples.

Figure 3-16 showed the cycling performance of the samples. All of them were first activated by cycling for 2 cycles at low current rate of 0.05C. Then the current rate was increased to 0.5C and hold for 100 cycles. For both mSi/G and mSi/G_p samples, the severe capacity loss in the second cycle occurred leading to capacity decay and low columbic efficiency. This could be attributed to the collapse of micro size Si particles in electrochemical reactions. The decreasing trend in initial specific capacity with decreasing particle size agreed with other published works and might be caused by increasing agglomeration in decreasing nanosized particles. After the 5th cycle, both mSi/G and mSi/G_p samples retained less capacity than that of the commercialized graphite. Furthermore, the cycling performance of Si/G composite anodes were improved with

decreasing particle size. The capacity of nSi100/G at the 100th cycle was 843 mAh/g corresponding to a reversible capacity retention of 50.1%; the capacity of nSi40/G at the 100th cycle was 1,170 mAh/g, corresponding to a reversible capacity retention of 74.3% and the capacity of nSi25/G at the 100th cycle was 651 mAh/g corresponding to a reversible capacity retention of 66.7%. The best discharge capacity came from nSi100/G_p. which was 1,563 mAh/g at 100th cycle. The piranha solution treatment improved the cycling performance of all samples. The reversible capacity retention of nSi100/G_p at 100th cycle was 77%, which was higher than that of nSi100/G. The samples of nSi40/G_p and nSi25/G_p demonstrated a similar improvement. Though nSi100/G_p exhibited the best cycling performance in capacity value, nSi40/G_p resulted in the best overall electrochemical performance with the least capacity decay and the highest reversible capacity retention of 89.1% at the 100th cycle of 1,360 mAh/g. The 25 nm Si/Graphene nanocomposites were also studied in cycling performance test. nSi25/G_p had a lower discharge capacity at 100th cycle of 819 mAh/g at the current rate of 0.5C.
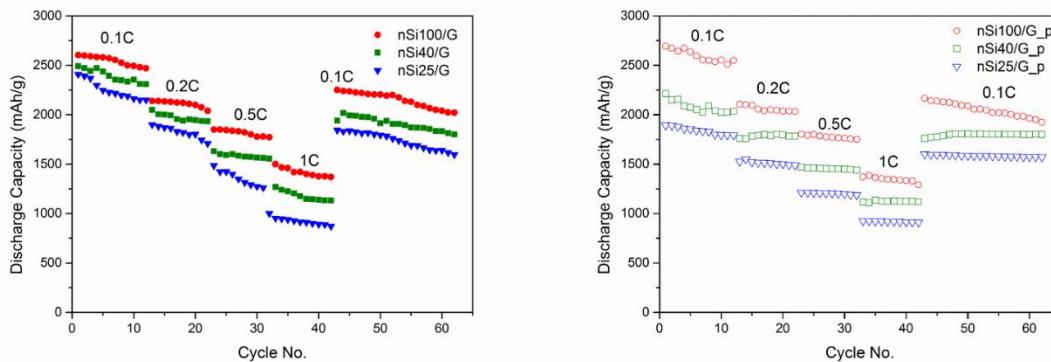

Figure 3-17: Rate performance of a) Si/Graphene nanocomposites without piranha treatment, b) Si/Graphene nanocomposites with piranha treatment; all the sample were charged at increased rates of 0.1C, 0.2C, 0.5C and 1C for each 10 cycles, then cycled for another 20 cycles at the current rate of 0.1C

Rate performance tests were carried out at charge/discharge current densities of 0.1C, 0.2C, 0.5C and 1C for 10 cycles each and concluded with current density of 0.1C for final 20 cycles as shown in Figure 3-17. The rate performance of mSi was not exhibited due to their fast irreversible failure after only a few cycles. The Si/Graphene nanocomposites pretreated by piranha solution showed a more stable rate performance than that of Si/Graphene nanocomposites without piranha solution treatment. The nSi25/G had less capacity decay and more capacity recovering after high rate cycling than that of nSi100/G. In details, the nSi100/G_p gave the highest capacity of around 1,350 mAh/g at the current rate of 1C; the nSi40/G_p demonstrated the best cycling performance overall at all current rates. At 1C current rate, the capacity began with 1,139 mAh/g and ended at 1,118 mAh/g after 10 cycles. The nSi25/G_p also demonstrated a good rate performance with an ending capacity of 910 mAh/g at the current rate of 1C.

Table 3-5: Summary of Si/Graphene anode electrochemical data

		Cycling Performance		Rate Performance	
		Initial Capacity at 0.05C	Capacity at the 100th cycle	Capacity at 1C after 10 cycles	Recovered capacity at 0.1C after 20 cycles
Si 20-30 nm	nSi25/G	2,603 mAh/g	641 mAh/g	871 mAh/g	1,496 mAh/g
	nSi25/G_p	2,287 mAh/g	820 mAh/g	910 mAh/g	1,572 mAh/g
Si 30-50 nm	nSi40/G	2,697 mAh/g	1,170 mAh/g	1,030 mAh/g	1,713 mAh/g
	nSi40/G_p	2,445 mAh/g	1,362 mAh/g	1,118 mAh/g	1,799 mAh/g

Si 100 nm	nSi100/G	2,793 mAh/g	843 mAh/g	1,271 mAh/g	1,901 mAh/g
	nSi100/G_p	2,737 mAh/g	1,563 mAh/g	1,350 mAh/g	1,924 mAh/g
Si 1-5 μm	mSi/G	3,345 mAh/g	N/A	N/A	N/A
	mSi/G_p	3,497 mAh/g	N/A	N/A	N/A

In this study, the electrochemical performance of Si/G nanocomposites were improved by two contributors: nanosized particles and the zeta potential difference between GO precursor and positively charged Si particles. All the electrochemical performance data were summarized in Table 3-5. For Si particles with a smaller size, it could better accommodate the huge volume expansion during charge/discharge of Si anode especially for nanosized particle less than 150 nm as 150 nm was the critical size to prevent the creak from happening. The piranha treatment allowed to directly manipulate the surface charge of Si particles in present of higher zeta potential than that of charged particles without piranha treatment. Comparing with directly attacking Si surface by amide groups, the piranha solution made the Si surface more vulnerable to $-NH_2$ hydrolysis reaction by exposing more –OH groups. This would sufficiently increase the zeta potential difference then generate a stronger bonding between Si and graphene oxide. This well assembled Si/Graphene nanostructure helped maintain the integrity of Si nanoparticles during cycling, improve the kinetics of delithiation process and increase the electric conductivity of the nanocomposites, thus a good cycling performance and rate performance could be both expected. The Si nanoparticles Si100/G_p had an initial capacity of 2,737 mAh/g at the

current rate of 0.05C and the 100th discharge capacity of 1,563 mAh/g at the current rate

of 0.5C. The nSi40/G_p had a discharge capacity around 1,118 mAh/g at current rate of

1C, which was about 3 times higher than that of graphite (372 mAh/g).

4. Conclusions

In summary, we successfully synthesized graphene from graphite flasks, and utilized the reduction process to fabricate Si/Graphene anode composites for lithium-ion batteries, particularly for high-energy density applications. The surface layer of SiO_2 on Si particles was taken advantage by anchor silane agent with amide functional groups to positively charge the Si particles. The encapsulated structures helped maintain the integrity of Si nanoparticles during cycling, prevent the Si nanoparticles from losing contact with conductive materials. The initial capacity of Si/G composites were 3,345 mAh/g, 2,793 mAh/g and 2,697 mAh/g for mSi/G, nSi100/G and nSi30/G respectively. The Si/G nanocomposites maintained the discharge capacity of ~840 mAh/g after 100 cycles at the current rate of 0.5C. The piranha pretreatment increased the zeta potential of NH_2 functionalized Si particles for additional ~25 mV which resulted in more Si particles loaded on the graphene surface. The existing of strongly encapsulated graphene benefited from piranha treatment could improve the kinetics of delithiation process and increase the electric conductivity of the nanocomposites. The nSi100/G_p had the highest discharge capacity of 1,563 mAh/g after 100 cycles at a current density of 0.5C. The nSi40/G_p presented the outstanding rate performance with a retained capacity of 1,118 mAh/g at a current density of 1C. The nSi40/G_p also gave the best cycling performance at the current rate of 0.5C, in which the discharge capacity of the 100th cycle was 1,360 mAh/g.

Reference

1. Liu, X.H., et al., *Size-dependent fracture of silicon nanoparticles during lithiation.* Acs Nano, 2012. **6**(2): p. 1522-1531.
2. Chon, M.J., et al., *Real-time measurement of stress and damage evolution during initial lithiation of crystalline silicon.* Physical Review Letters, 2011. **107**(4): p. 045503.
3. Lee, Y.M., et al., *SEI layer formation on amorphous Si thin electrode during precycling.* Journal of The Electrochemical Society, 2007. **154**(6): p. A515-A519.
4. Pinson, M.B. and M.Z. Bazant, *Theory of SEI formation in rechargeable batteries: capacity fade, accelerated aging and lifetime prediction.* Journal of the Electrochemical Society, 2013. **160**(2): p. A243-A250.
5. Lee, J.K., et al., *Silicon nanoparticles-graphene paper composites for Li ion battery anodes.* Chem Commun (Camb), 2010. **46**(12): p. 2025-7.
6. Li, H., C. Lu, and B. Zhang, *A straightforward approach towards Si@C/graphene nanocomposite and its superior lithium storage performance.* Electrochimica Acta, 2014. **120**: p. 96-101.
7. Li, Z.F., et al., *Novel pyrolyzed polyaniline-grafted silicon nanoparticles encapsulated in graphene sheets as li-ion battery anodes.* ACS Appl Mater Interfaces, 2014. **6**(8): p. 5996-6002.
8. Mi, H., et al., *Three-dimensional network structure of silicon-graphene-polyaniline composites as high performance anodes for Lithium-ion batteries.* Electrochimica Acta, 2016. **190**: p. 1032-1040.
9. Ye, Y.-S., et al., *Improved anode materials for lithium-ion batteries comprise non-covalently bonded graphene and silicon nanoparticles.* Journal of Power Sources, 2014. **247**: p. 991-998.
10. Liu, X.H. and J.Y. Huang, *In situ TEM electrochemistry of anode materials in lithium ion batteries.* Energy & Environmental Science, 2011. **4**(10): p. 3844-3860.
11. Liu, X.H., et al., *In situ TEM experiments of electrochemical lithiation and delithiation of individual nanostructures.* Advanced Energy Materials, 2012. **2**(7): p. 722-741.
12. Liu, W.-R., et al., *Effect of electrode structure on performance of Si anode in Li-ion batteries: Si particle size and conductive additive.* Journal of Power Sources, 2005. **140**(1): p. 139-144.
13. Kim, H., et al., *A Critical Size of Silicon Nano‐Anodes for Lithium Rechargeable Batteries.* Angewandte Chemie International Edition, 2010. **49**(12): p. 2146-2149.
14. Wang, J.-Z., et al., *Flexible free-standing graphene-silicon composite film for lithium-ion batteries.* Electrochemistry Communications, 2010. **12**(11): p. 1467-1470.
15. Tao, H.-C., et al., *Self-supporting Si/Reduced Graphene Oxide nanocomposite films as anode for lithium ion batteries.* Electrochemistry Communications, 2011. **13**(12): p. 1332-1335.
16. Xiang, H., et al., *Graphene/nanosized silicon composites for lithium battery anodes with improved cycling stability.* Carbon, 2011. **49**(5): p. 1787-1796.
17. Luo, J., et al., *Crumpled Graphene-Encapsulated Si Nanoparticles for Lithium Ion Battery Anodes.* The Journal of Physical Chemistry Letters, 2012. **3**(13): p. 1824-1829.
18. Xin, X., et al., *A 3D porous architecture of Si/graphene nanocomposite as high-performance anode materials for Li-ion batteries.* Journal of Materials Chemistry, 2012. **22**(16): p. 7724-7730.
19. Ji, J., et al., *Graphene‐Encapsulated Si on Ultrathin‐Graphite Foam as Anode for High Capacity Lithium‐Ion Batteries.* Advanced Materials, 2013. **25**(33): p. 4673-4677.

20.   Li, N., et al., *Encapsulated within graphene shell silicon nanoparticles anchored on vertically aligned graphene trees as lithium ion battery anodes.* Nano Energy, 2014. **5**: p. 105-115.

21.   Bai, X., et al., *Si@SiOx/graphene hydrogel composite anode for lithium-ion battery.* Journal of Power Sources, 2016. **306**: p. 42-48.

22.   Cen, Y., et al., *Fabrication of TiO 2–graphene composite for the enhanced performance of lithium batteries.* RSC Advances, 2016. **6**(71): p. 66971-66977.

23.   Trill, J.-H., et al., *NMR investigations on the lithiation and delithiation of nanosilicon-based anodes for Li-ion batteries.* Journal of Solid State Electrochemistry, 2011. **15**(2): p. 349-356.

24.   Buriak, J.M., *High surface area silicon materials: fundamentals and new technology.* Philosophical Transactions of the Royal Society of London A: Mathematical, Physical and Engineering Sciences, 2006. **364**(1838): p. 217-225.

25.   Ferrari, A., et al., *Raman spectrum of graphene and graphene layers.* Physical review letters, 2006. **97**(18): p. 187401.

26.   Eigler, S., et al., *Wet chemical synthesis of graphene.* Advanced materials, 2013. **25**(26): p. 3583-3587.

27.   Key, B., et al., *Real-time NMR investigations of structural changes in silicon electrodes for lithium-ion batteries.* Journal of the American Chemical Society, 2009. **131**(26): p. 9239-9249.

28.   Hatchard, T. and J. Dahn, *In situ XRD and electrochemical study of the reaction of lithium with amorphous silicon.* Journal of The Electrochemical Society, 2004. **151**(6): p. A838-A842.

29.   Li, J. and J. Dahn, *An in situ X-ray diffraction study of the reaction of Li with crystalline Si.* Journal of The Electrochemical Society, 2007. **154**(3): p. A156-A161.

Paper 3: The Study of Graphene Quality in Si/Graphene Nanocomposite Anode for Lithium-ion Battery

Yinjie Cen[a], Qingwei Qin[b], Mingjiang Tao[c], Richard D. Sisson[a], Jianyu Liang[a*]

a. Department of Mechanical Engineering, Worcester Polytechnic Institute, Worcester, MA, 01609 United State

b. The Key State Laboratory of Refractories and Metallurgy, Wuhan University of Science and Technology, Wuhan, Hubei 430081, China

c. Department of Civil Engineering, Worcester Polytechnic Institute, Worcester, MA 01609 United State

Abstract:

Si/Graphene nanoparticles are attractive alternative anode materials for Lithium-ion batteries due to its large specific capacity of 3,579 mAh/g. When Si is employed as the key active material for anode, conductive carbon is necessary to provide the needed conductivity. The carbon materials selected in Si/C composites affects the electrochemical performance of resulted anode. In this study, three batches of Graphene with different surface morphology, chemical potential, defect density and electronic conductivity was fabricated. Si/Graphene nanocomposites were formed by static electric self-assembly followed with the in-situ reduction process. Graphene that exhibited the highest surface area of 464.8 m^2/g, the shortest defect distance of 9.96 nm and the lowest charge transfer resistance of 47.33 Ω demonstrated the best overall electrochemical performance in the battery test. It had the highest initial discharge capacity of 2,692 mAh/g at the current rate

of 0.1C, the best cycling performance of 1,135 mAh/g at the 200th cycle at the current rate of 0.5C and the best rate performance of around 1,300 mAh/g at the current rate of 1C. This work confirms that the desired graphene quality for Si/Graphene nanocomposite anode is drastically different from what is demanded by some other applications and could be useful to the design of different types of graphene nanocomposite anode.

1. Introduction

Silicon (Si) is a promising candidate for Lithium-ion battery anode with very high theoretical capacity of 3,579 mAh/g. However the Si anodes in Lithium-ion batteries suffer large volume expansion (~300%) and low conductivity during lithiation and delithiaion process [1, 2]. The volume expansion causes cracking and pulverization of the Si anode which leads to poor cycling performance, and the low conductivity results in low rate performance [3-5]. Carbon coating is necessary to improve conductivity and electrochemical performance. The carbon must be able to retain intimate contact with Si nanoparticles before and after volume expansion and electronically/ioniclly conductive as well as electrochemically stable to form solid electrolyte interphase (SEI) layers [6, 7]. Different methods have been employed to obtain the carbon coating, including chemical vapor deposition (CVD) [8], ball milling [9] and sol–gel polycondensation followed with carbonization [10]. The carbon coating quality plays an important role in improving electrode performance: Yoshio et al demonstrated a 17.6 wt% carbon coating on natural graphite anode outperformed in Ethylene carbonate (EC) based electrolyte than in propylene carbonate (PC) based electrolyte [11]; Fey et al studied that the thickness of carbon coating layer must be uniformly distributed around each active $LiFePO_4$ particles to decrease the polarization [12]; Kim et al found out that carbon coated layer on $LiNi_{1/3}Mn_{1/3}Co_{1/3}O_2$ particles by sugar precursor could suppress the generation of oxygen to improve thermal stability [13].

Si/Graphene has attracted much attention due to graphene's unique property such as outstanding stiffness (1.1×10^3 GPa Young's Modulus) and super electronic conductivity (10^6 S/m) [14]. Si/Graphene nanocomposites anode have been fabricated by various

methods such as mechanical mixing [15, 16], pyrolyzed PANI functionalized assembly [17] and amide functional group self-assemble method [18, 19]. Almost in all battery electrodes, graphene is obtained by reduction of graphene oxide (GO) in favor of low cost, energy efficiency and easiness to functionalization for specific applications. GO synthesized by Hummer's/Modified Hummer's method is the state-of-art precursor to obtain the graphene nanosheets by in-situ thermal/chemical reduction [20, 21].

The study of graphene quality in electrode materials is still blank. In the study of other applications such as bioelectric sensor devices, optical electronics and photovoltaic cells, much attention has been devoted to understand the desired graphene quality. It is discovered that single or mono layer, large and flat surface and defect-free structure were desirable for these applications [22-24]. Battery electrodes may demand different set of qualities. Our previous work have demonstrated that the quality of synthesized graphene nanosheets could be tuned by process control [25]. In this study, three batches of Graphene with different surface morphology, chemical potential, defect density and electronic conductivity was fabricated. Si/Graphene nanocomposites were formed by static electric assembly followed with the in-situ reduction process.

It was found that the electrochemical performance of Si/Graphene nanocomposite anode benefited from high surface area, high defect density and high electronic conductivity. An initial discharge capacity of 2,692 mAh/g at the current rate of 0.1C, with cycling performance of 1,135 mAh/g at the 200th cycle at the current rate of 0.5C and rate performance of around 1,300 mAh/g at the current rate of 1C was achieved in the sample with Graphene that exhibited the highest surface area of 464.8 m^2/g, the shortest defect

distance of 9.96 nm and the lowest charge-transfer resistance of 47.33 Ω. This work could

be useful to the design of different types of graphene nanocomposite anode.
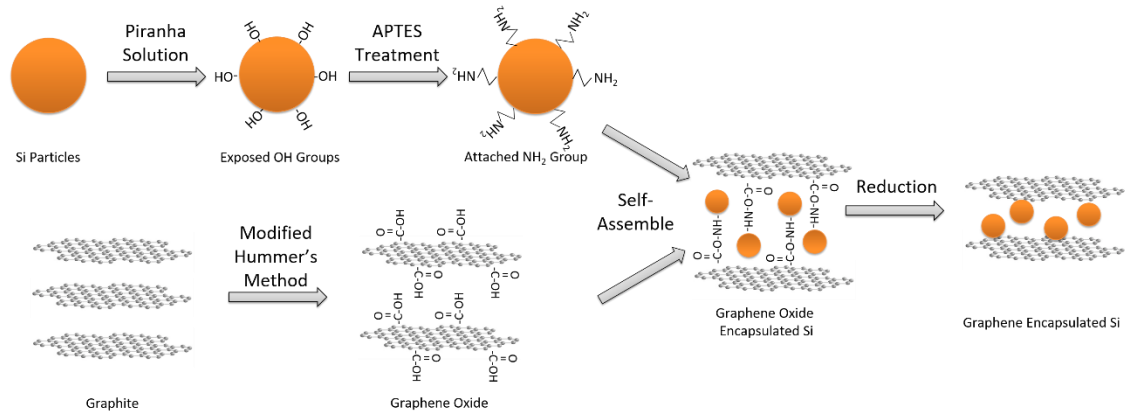
2. Experiments

Figure 3-18: Process flow of Si/Graphene nanocomposites fabrication

Figure 3-18 presented the general process of Si/Graphene nanocomposites fabrication. The Si nanoparticles were purchased from Alfa Aesar (crystalline, APS = 100 nm, 99%, Plasma Synthesized). Si nanoparticles were pre-washed by piranha solution then functionalized with $-NH_2$ groups to introduce positive surface charges. In two samples, graphite flakes were oxidized by modified Hummer's method to obtain negatively charged GO precursors for graphene nanosheets. Then static electric self-assembly enabled the formation of Si/GO nanocomposite between negatively charged GO and positively charged Si nanoparticles. Then in-situ thermal or chemical reduction was performed to acquire Si/G nanocomposites. The thermal reduced Si/G nanocomposites were named as Si/tRG and chemical reduced Si/G nanocomposites were named as Si/cRG. Another Si/G nanocomposites were prepared by improved modified Hummer's method followed with chemical reduction, which were named as Si/iRG.

The modification of Si nanoparticles

Si nanoparticles were immersed in freshly made piranha solution (H_2SO_4/H_2O_2 = 3:1 v/v) for 1 h at 80 °C to introduce hydroxyl groups on the surface. After washing, filtration and

drying, the 1 wt% methanol solution of (3-aminopropyl)triethoxysilane (APTES, 99%, Sigma Aldrich) was used to introduce -NH_2 functional groups on the surface of Si nanoparticles. The resulted powder were washed and dried in a vacuum oven at 80 °C overnight.

GO synthesis

The GO was synthesized by adapting a reported modified Hummer's method. A mixture of H_2SO_4 (95-98%, Alfa Aesar) and H_3PO_4 (85%, Alfa Aesar) with volume ratio of 9:1 was added to a mixture of natural graphite flakes (99.9%, Alfa Aesar) and $KMnO_4$ (>99%, Sigma Aldrich). The reaction was then heated to 50 °C and stirred for 12 h. Finally, the reaction was cooled to room temperature and poured onto ice cubes with H_2O_2 (30%, Sigma Aldrich) to form a stable bright yellow suspension.

An improved process was performed with caution to maintain reaction temperature to be below 5 °C to minimize defect density in the obtained GO [26]. The resulted bright yellow suspension was washed by Deionized Water (DI Water) followed with filtration and vacuum dry.

Fabrication of Si/G nanocomposites

The Si/GO nanocomposites were formed. The Si nanoparticles were dispersed in N, N-dimethyloformamide (DMF, 99%, Sigma-Aldrich) by sonication for 1 hour, then the prepared GO powders were added. The whole suspension was sonicated and stirred for 3 hours to form Si/GO hydrogel. The reduction of Si/GO nanocomposites followed two routines:

1. Chemical Reduction Routine: Hydrazine (anhydrous, 98%, Sigma-Aldrich) was slowly added to Si/GO hydrogel under nitrogen (N2, UHP, Airgas) flux. The reaction was kept at 95 °C for overnight. The resultant black particles were collected by centrifuging and washed with ethanol. Finally, the as-made composites were dried in the vacuum oven for 12 hours to obtain the final Si/G nanocomposites.

2. Thermal Reduction Routine: The Si/GO hydrogel was dried in vacuum oven at 80 °C for overnight. Then the powders were reduced under N_2 at 1,000 °C in a tube furnace for 3 h to get Si/Graphene nanocomposites.

Characterization: physical and electrochemical properties

The surface area of selected Si particles was measured by Brunauer–Emmett–Teller (BET) gas absorption method (Micromeritics ASAP 2020). The morphology was confirmed by Scanning Electron Microscopy (SEM, JOEL 7000F). The crystal structures were investigated by X-Ray Diffraction (XRD, Cr Kα radiation at λ=2.23 Å, PANALYTICAL EMPYREAN). The actual graphene loading ratio was measured by Thermogravimetric Analyzer (TGA Q50, TA instruments). Raman Spectrum (Horiba, XploRA One, 532 nm green laser) was performed to characterize the quality of reduced graphene. Zeta potential was measured by Zetasizer Nano ZS90 (Malvern) to confirm the surface charge of GO and modified Si. The electrode conductivity of Si/Graphene was verified by Electrochemical Impedance Spectroscopy (EIS, Bio-Logic SAS) at scanning range of 200 kHz to 1 mHz.

The anode was prepared by mixing of electrode, acetylene black (MTI) and carboxymethyl cellulose (CMC, MTI) / Styrene-Butadiene Rubber (SBR) binder at a weight ratio of 70:15:15, respectively. The resulted slurry was casted on a piece of Cu foil by doctor blade and dried at 60 °C for 12 h, then transferred into a vacuum furnace at 120 °C for 8 h. The

electrochemical properties were tested with CR2032 coin cell with Lithium foil as counter electrode. The electrolyte was 1 M $LiPF_6$ dissolved in a mixed solution of diethyl carbonate (DEC) and ethyl carbonate (EC) with 1:1 vol ratio with 2 wt% fluoroethylene carbonate (FEC, 99%, Sigma-Aldrich) as additive. The electrochemical performance was tested between 0.001 and 1.5 V at different current rates. The charging/discharging current rates were calculated based on the theoretical capacity of lithiated $Li_{15}Si_4$ as 3,579 mAh/g [27].
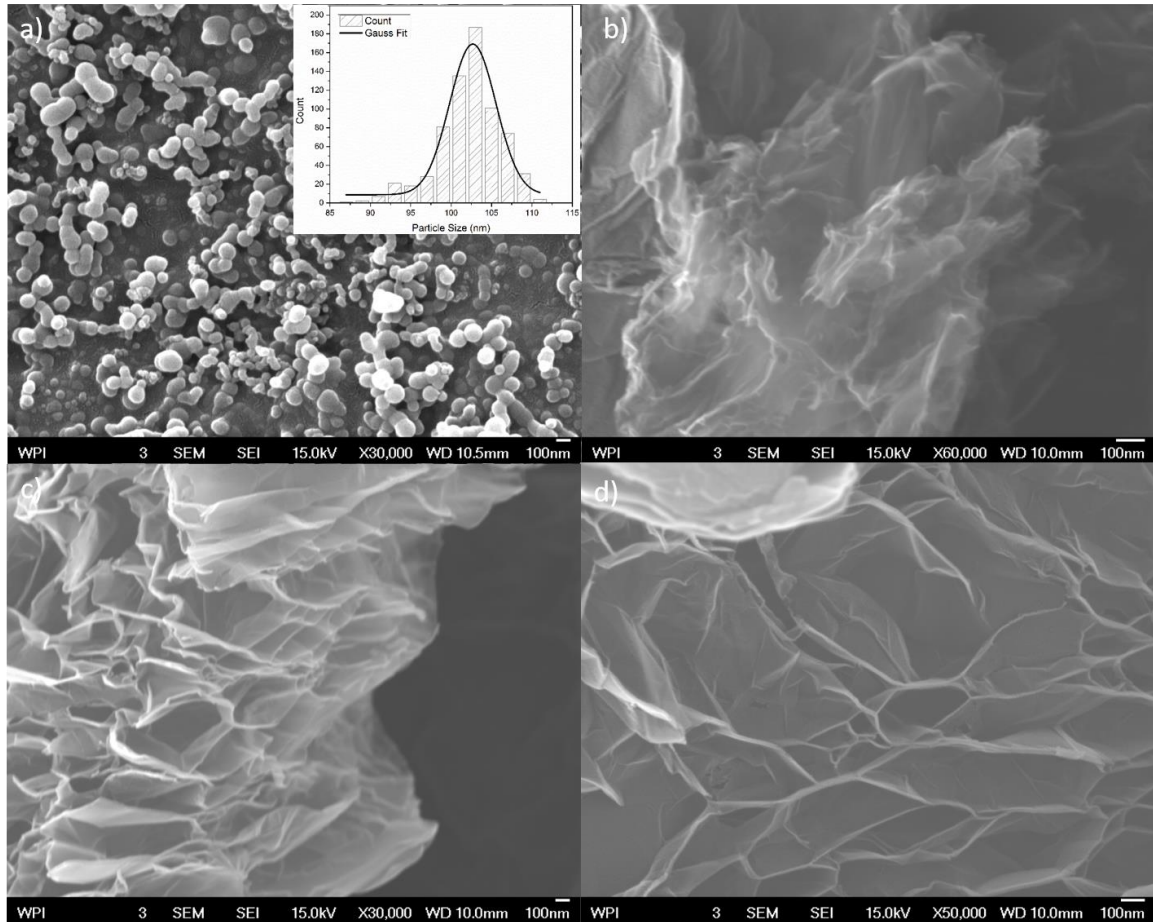
3. Results and Discussion

Figure 3-19: The SEM pictures of the morphologies of 100 nm Si particles with size distribution chart inserted (a), graphene nanosheets synthesized by modified Hummer's method + Thermal reduction (b), modified Hummer's method + Chemical reduction (c) and improved modified Hummer's method + Chemical reduction (d).

Figure 3-19 gave the selected SEM pictures of 100 nm Si particles and the graphene nanosheets synthesized by corresponding Hummer's method + reduction method. In Figure 3-19 (a), the particle size of Si was clearly observed and the size distribution was counted by image J software to confirm the 100 nm Si nanoparticles. The layered morphology of graphene was observed as in Figure 3-19 (b-d). Irregularly stacked sheets could be seen in all three samples. The chemical reduced graphene nanosheets had the highest crumpled degree, which indicated the higher surface areas than other two samples. It was in agreement with specific surface area measured in Table 3-7. The improved modified

103

Hummer's method at the low reaction temperature produced lager and flatter graphene nanosheets due to better preservation of the carbon honeycomb framework, which was in agreement with literature [26].
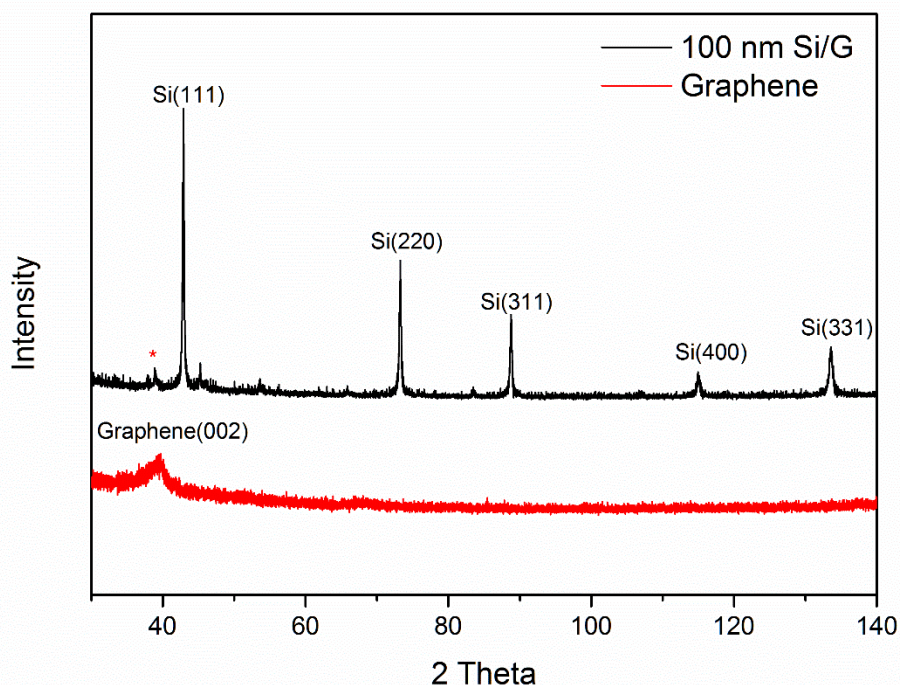

Figure 3-20: XRD of 100 nm Si/Graphene nanocomposites and graphene nanosheets

The crystalline structure of graphene and Si/Graphene were analyzed by X-ray diffraction (XRD) as shown in Figure 3-20. XRD spectrums of all reduced graphene nanosheets samples were all most identical, showing the characterization peek at 39.707° with broad peak width and weak intensity. This was led by the decreasing of the crystal integrity while the disorder parameter increased. The trace of graphene characterization peak was labeled with "*" in the XRD profile of Si/Graphene nanocomposites. The main characterization peaks of pure Si at 42.965°, 73.319°, 88.812°, 115.038° and 133.581° could be assigned to

the (111), (220), (311), (400) and (331) diffractions of Si (XRD database: ICDD number 01-0791) respectively.

Table 3-6: The Zeta potential of GO, comparing with APTES charged Si

	Zeta Potential
Modified Hummer's Method GO	-35.78 mV
Improved Modified Hummer's Method GO	-31.27 mV
APTES Charged-Si	+37.73 mV

The zeta potential was employed to determine the surface charge of samples in the form of the potential difference between the dispersion medium and stationary layer of dispersed particles. In Table 3-3 GO formed by modified Hummer's method has a zeta potential of -35.78 mV. GO synthesized by improved modified Hummer's method had a higher zeta potential of -31.27 mV. Si had a positively charged zeta potential of 37.73 mV which confirmed the successful surface modification.

Table 3-7: Summary of specific surface area and graphene weight ratio in Si/Graphene nanocomposites

	Specific Surface Area	Graphene weight ratio
tRG	291.2 m^2/g	8.86 %
cRG	464.8 m^2/g	9.31 %
iRG	413.3 m^2/g	9.08 %

Table 3-7 summarized the specific surface area and zeta potential of synthesized graphene nanosheets and APTES modified Si nanoparticles. The cRG sample had the highest specific surface area of 464.8 m^2/g. The specific surface area of iRG was lower than that of cRG which can be explained by the less crumpled surface. The tRG had the lowest specific surface area of 291.2 m^2/g, which was caused by the incomplete exfoliation process at the high temperature [28-30]. The actual weight ratio of Graphene nanosheets in Si/Graphene nanocomposites were investigated by TGA and the actual graphene loading

weight for Si/tRG, Si/cRG and Si/iRG were 8.86%, 9.13% and 9.08% respectively. They
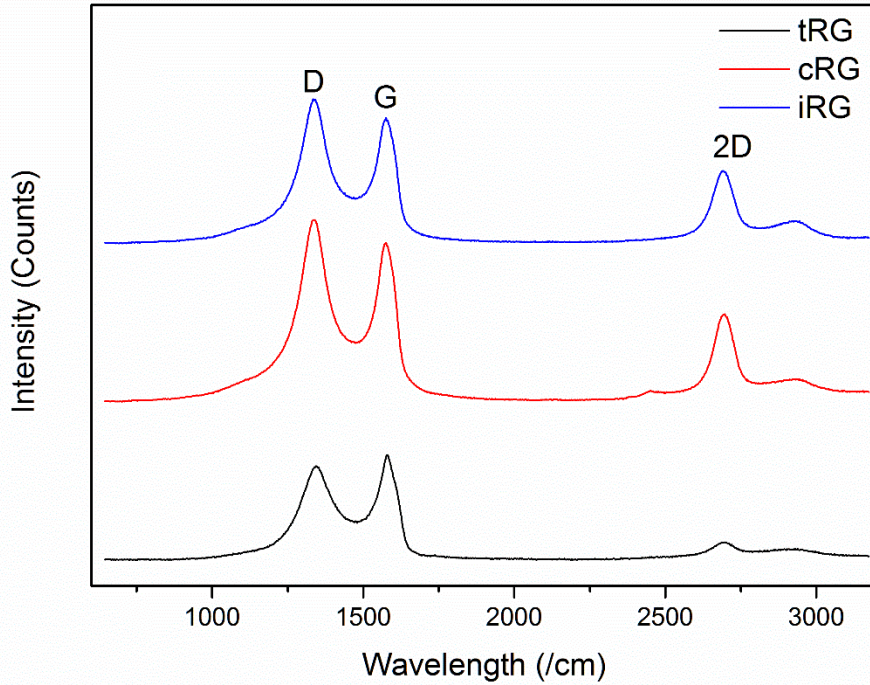
were all close to the targeted 10% loading weight.

Figure 3-21: Raman Spectrum of thermal reduced graphene (in black), chemical reduced graphene (in red) and improved modified Hummer's method with chemical reduction (in blue) under the 532 nm green laser radiation; The D, G and 2D band peaks were labeled.

Table 3-8: Summary of reduced graphene properties based on the Raman Spectrum of tRG, cRG and iRG in Figure 3-21

	2D Peak Intensity	I_D/I_G	Defect Distance (L_D)
tRG	Week	0.96	12.33 nm
cRG	Strong	1.47	9.96 nm
iRG	Strong	1.38	10.28 nm

The Raman spectroscopy is a fast, nondestructive and informative technique to characterize quality of graphene [31] such as the number of stacking layers and defect density. In Raman spectrum, G band around 1580 cm^{-1} and 2D band around 2700 cm^{-1}, were commonly used to identify the graphene. G band stood for C=C bond stretching of all pairs of sp^2 atoms. 2D band was caused by the double resonance process. The intensity of 2D band and its symmetrical shape were commonly used to characterize AB-stacked graphene structure and can be used to determine the number of graphene layers [32, 33]. For the tRG sample, the 2D band at 2695 cm^{-1} was very week, comparing to those of cRG sample and iRG sample. This indicated that the tRG sample possessed a graphitic stacking structure. D band at around 1350 cm^{-1} indicated the out of plane vibrations attributed to the presence of structural defects, in which the increasing of D band intensity resulted in more sp^2 domains. It had been proven that the value of the I_D/I_G could be used to measure the disorder degree of graphene nanosheets. The relationship between I_D/I_G and the defect distance (L_D) was proposed as: $\frac{I_D}{I_G} = \frac{C(\lambda)}{L_D^2}$ in the consideration of point defects, where C(λ) was the function of liner laser wavelength [34-36]. The larger the I_D/I_G, the smaller the crystallite size and the smaller the defect distance. The I_D/I_G of reduced graphene were 0.96, 1.47 and 1.38 for tRG, cRG and iRG respectively. Thus the L_D could be calculated based on the excitation energy of Raman spectrum (532 nm, 2.33 eV) as 12.33 nm, 9.96 nm and 10.28 nm for tRG, cRG and iRG respectively. The tRG had the longest defect distance, which could be explained by the incomplete exfoliation during reduction process temperature [28-30]. The iRG had a lower defect density than that of cRG, which could be attributed to the better preserved honeycomb structure by improved Hummer's method. Key information from Raman study were summarized in Table 3-8.
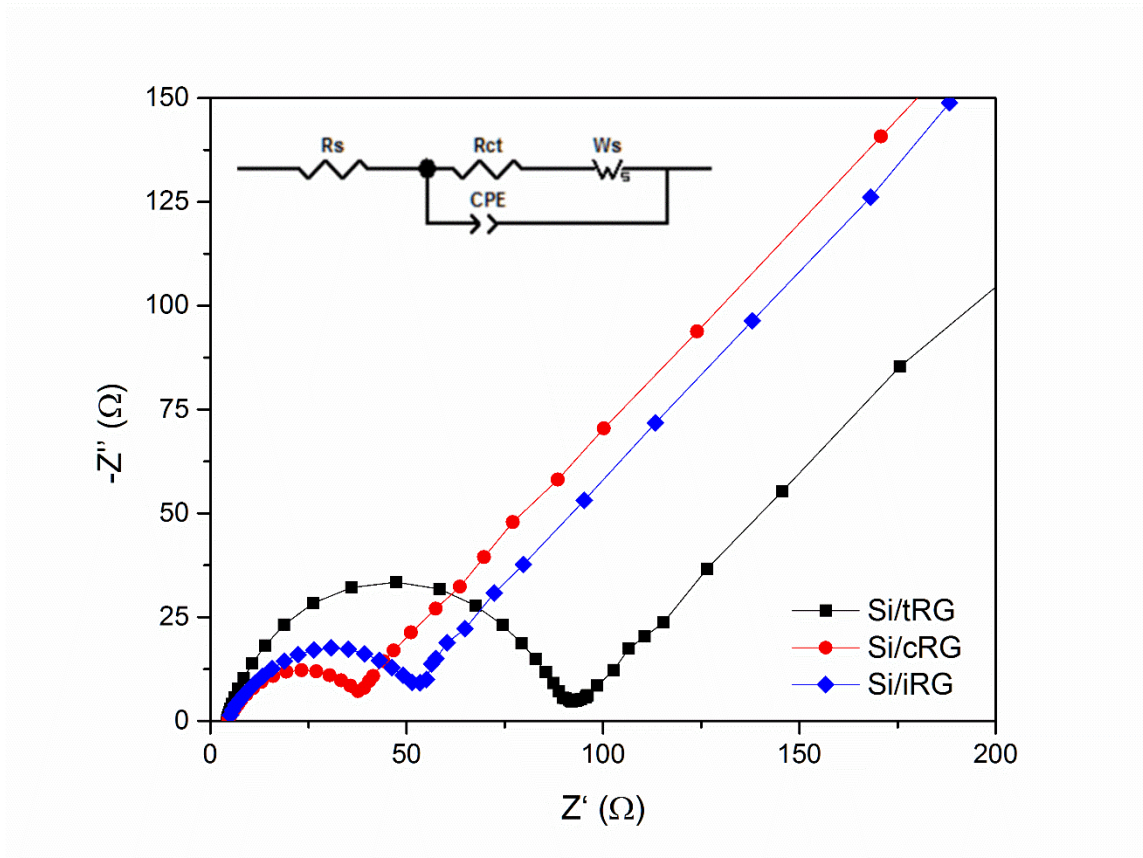
Figure 3-22: EIS of Si/tRG in black, Si/cRG in red and Si/iRG in blue with the correlated Nyquist fitting at the scanning range of 200 kHz to 1 mHz

Table 3-9: Summary of charge-transfer resistance of Si/Graphene nanocomposites

	Charge-transfer resistance (R_{ct})
Si/tRG	89.52 Ω
Si/cRG	47.33 Ω
Si/iRG	62.15 Ω

The electronic conductivity of three Si/graphene samples was investigated by EIS with insertion of simulated equivalent circuit by Z-view software in Figure 3-22. All three EIS

curves fitted with the typical Nyquist plot, which included one semicircle in the high-middle frequency region and a vertically inclined tail. The semicircle was correlated to the internal resistance (R_S) and charge-transfer resistance (R_{ct}). The low frequency region was corresponded to the lithium ion diffusion in the electrodes called Warburg tail. For Si/Graphene nanocomposites, R_{ct} had the key information about the electrode interface. As seen in Table 3-9, Si/cRG anode gave the lowest charge-transfer resistance which indicated that the cRG had the highest conductivity at the interface. This may be attributed to large specific surface area and the high defect density. Low charge-transfer resistance is beneficial for obtaining good cycling performance in batteries.
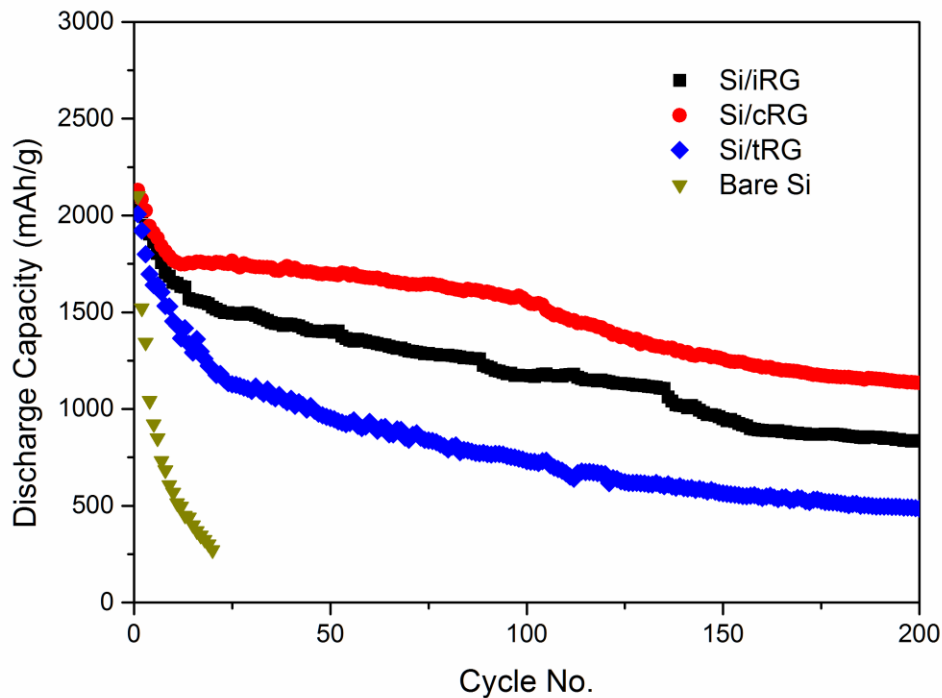

Figure 3-23: Long-term electrochemical performance of Si/iRG (black), Si/cRG (red) and Si/tRG (blue) nanocomposites for 200 cycles under the current rate of 0.5C with Si specific discharge capacity, bare Si (yellow) for comparison.

The long-term electrochemical performance of all three Si/Graphene nanocomposites were shown in Figure 3-23. All the coin cells were tested under the current rate of 0.5C for 200 cycles after 2 charging/discharging cycles at the current rate of 0.1C for initiation process. Bare Si's cycling performance was also included for comparison. The Si/tRG nanocomposites demonstrated the most severe capacity decay and had a 24.2% capacity retention with the discharge capacity of 485 mAh/g at the 200th cycle. Si/cRG demonstrated a discharge capacity of 1,135 mAh/g at 200th cycle, corresponding to a reversible capacity retention of 53.3%. The Si/iRG nanocomposites also exhibited a cycling performance with the discharging capacity of 837 mAh/g at the 200th cycle. It stood for 41.3% capacity retention.
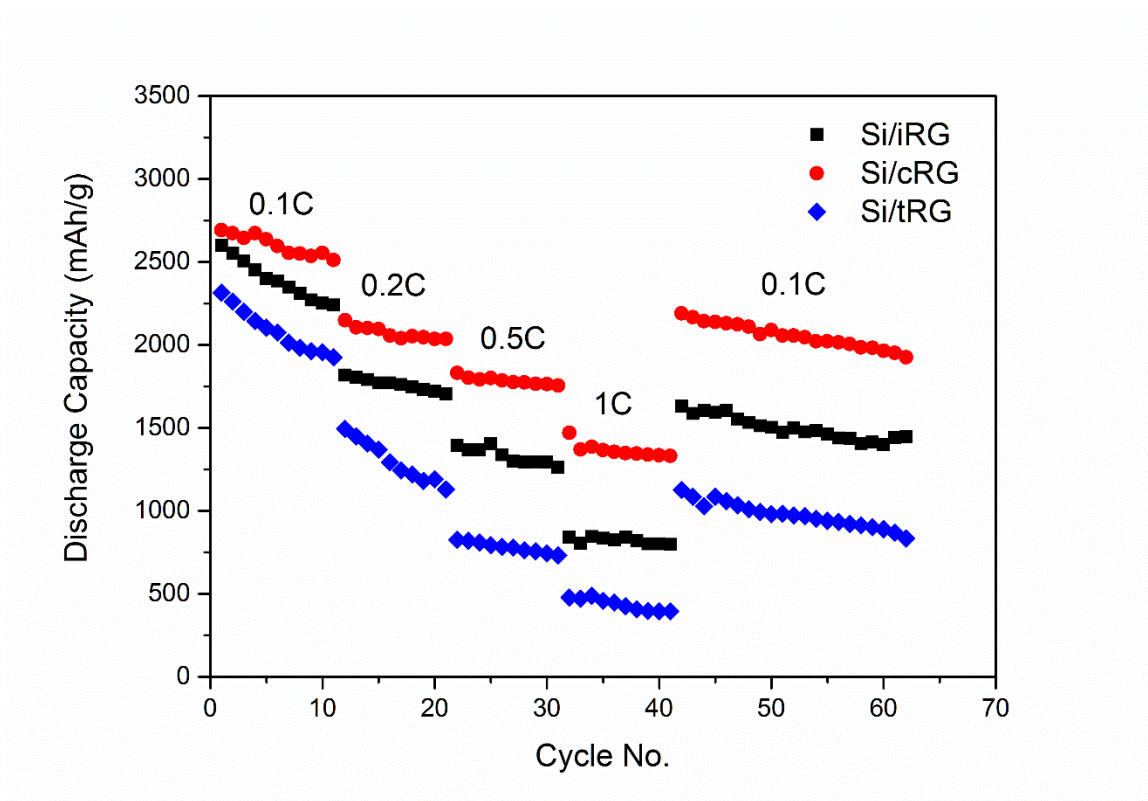

Figure 3-24: Rate performance of Si/Graphene nanocomposite anode of Si/iRG (black), Si/cRG (red) and Si/tRG (blue) under the current densities of 0.1C, 0.2C, 0.5C and 1C for each 10 cycles then back to 0.1C for final 20 cycles with Si specific discharge capacity

The rate performance tests were carried out at charge/discharge current densities of 0.1C, 0.2C, 0.5C and 1C for 10 cycles each and concluded with current density of 0.1C for final 20 cycles as shown in Figure 3-24. The initial capacities at the current rate of 0.1C were 2,601 mAh/g, 2,692 mAh/g and 2,314 mAh/g for Si/iRG, Si/cRG and Si/tRG respectively. The Si/cRG nanocomposites showed the best rate performance of all three samples. Si/cRG nanocomposites gave the highest capacity of around 1,300 mAh/g at the end of 10th cycle at current rate of 1C. After been cycled at 1 C, it restored its capacity to around 1,950 mAh/g after 20 cycles at 0.1C. The Si/tRG nanocomposites demonstrated the lowest capacity of around 390 mAh/g at the current rate of 1C.

Overall, the best electrochemical performance came from the Si/graphene nanocomposites employing the graphene nanosheets with highest surface area of 464.8 m^2/g, shortest defect distance of 9.96 nm and lowest charge-transfer resistance of 47.33 Ω. The thermally reduced graphene demonstrated a graphite-like structure and resulted in least desirable electrochemical performance, in which inefficient amount of graphene surface involved in loading Si nanoparticles. Another interested finding in this work was that Si/Graphene nanoparticle anode had its own preference for graphene quality. The iRG resulted in a flatter surface did not improve the electrochemical performance of Si/Graphene anode as much as crumpled cRG did.

4. Conclusion

In conclusion, the electrochemical performance of Si/Graphene nanocomposite anode could be improved by employing graphene with large surface area, short defect distance and low charge-transfer resistance. In this study, the Si/Graphene nanoparticles were formed by static electric self-assembly followed with the in-situ reduction process. The graphene synthesized by chemical reduction method resulted in the desirable properties with the highest specific surface area of 464.8 m^2/g, the shortest defect distance of 9.96 nm and the lowest charge-transfer resistance of 47.33 Ω. The corresponded Si/cRG nanocomposites showed outstanding electrochemical performance in battery test. It had the highest initial discharge capacity of 2,692 mAh/g at the current rate of 0.1C, the best cycling performance of 1,135 mAh/g at the 200th cycle at the current rate of 0.5C and the best rate performance of around 1,300 mAh/g at the current rate of 1C. This work pointed out that the desired reduced graphene qualities for Si/Graphene nanocomposite anode was different from other graphene applications. This work could also be helpful to the design of different types of graphene nanocomposite anode.

Reference

1.   Limthongkul, P., et al., *Electrochemically-driven solid-state amorphization in lithium-silicon alloys and implications for lithium storage.* Acta Materialia, 2003. **51**(4): p. 1103-1113.

2.   Buriak, J.M., *High surface area silicon materials: fundamentals and new technology.* Philosophical Transactions of the Royal Society of London A: Mathematical, Physical and Engineering Sciences, 2006. **364**(1838): p. 217-225.

3.   Obrovac, M. and L. Krause, *Reversible cycling of crystalline silicon powder.* Journal of The Electrochemical Society, 2007. **154**(2): p. A103-A108.

4.   Key, B., et al., *Real-time NMR investigations of structural changes in silicon electrodes for lithium-ion batteries.* Journal of the American Chemical Society, 2009. **131**(26): p. 9239-9249.

5.   Okamoto, H., *Li-Si (Lithium-Silicon).* Journal of Phase Equilibria and Diffusion, 2009. **30**(1): p. 118-119.

6.   Luo, F., et al., *Review—Nano-Silicon/Carbon Composite Anode Materials Towards Practical Application for Next Generation Li-Ion Batteries.* Journal of The Electrochemical Society, 2015. **162**(14): p. A2509-A2528.

7.   Lee, K.T. and J. Cho, *Roles of nanosize in lithium reactive nanomaterials for lithium ion batteries.* Nano Today, 2011. **6**(1): p. 28-41.

8.   Dimov, N., S. Kugino, and M. Yoshio, *Carbon-coated silicon as anode material for lithium ion batteries: advantages and limitations.* Electrochimica Acta, 2003. **48**(11): p. 1579-1587.

9.   Wang, D., et al., *High performance amorphous-Si@ SiO x/C composite anode materials for Li-ion batteries derived from ball-milling and in situ carbonization.* Journal of Power Sources, 2014. **256**: p. 190-199.

10.   Hasegawa, T., et al., *Preparation of carbon gel microspheres containing silicon powder for lithium ion battery anodes.* Carbon, 2004. **42**(12): p. 2573-2579.

11.   Yoshio, M., et al., *Effect of Carbon Coating on Electrochemical Performance of Treated Natural Graphite as Lithium‐Ion Battery Anode Material.* Journal of The Electrochemical Society, 2000. **147**(4): p. 1245-1250.

12.   Cho, Y.-D., G.T.-K. Fey, and H.-M. Kao, *The effect of carbon coating thickness on the capacity of LiFePO 4/C composite cathodes.* Journal of Power Sources, 2009. **189**(1): p. 256-262.

13.   Kim, H.-S., et al., *Effect of carbon coating on LiNi 1/3 Mn 1/3 Co 1/3 O 2 cathode material for lithium secondary batteries.* Journal of Power Sources, 2007. **171**(2): p. 917-921.

14.   Lee, C., et al., *Measurement of the elastic properties and intrinsic strength of monolayer graphene.* science, 2008. **321**(5887): p. 385-388.

15.   Lee, J.K., et al., *Silicon nanoparticles-graphene paper composites for Li ion battery anodes.* Chem Commun (Camb), 2010. **46**(12): p. 2025-7.

16.   Li, H., C. Lu, and B. Zhang, *A straightforward approach towards Si@C/graphene nanocomposite and its superior lithium storage performance.* Electrochimica Acta, 2014. **120**: p. 96-101.

17.   Li, Z.F., et al., *Novel pyrolyzed polyaniline-grafted silicon nanoparticles encapsulated in graphene sheets as li-ion battery anodes.* ACS Appl Mater Interfaces, 2014. **6**(8): p. 5996-6002.

18.   Mi, H., et al., *Three-dimensional network structure of silicon-graphene-polyaniline composites as high performance anodes for Lithium-ion batteries.* Electrochimica Acta, 2016. **190**: p. 1032-1040.

19.   Ye, Y.-S., et al., *Improved anode materials for lithium-ion batteries comprise non-covalently bonded graphene and silicon nanoparticles.* Journal of Power Sources, 2014. **247**: p. 991-998.

20.   Si, Y. and E.T. Samulski, *Synthesis of water soluble graphene.* Nano letters, 2008. **8**(6): p. 1679-1682.

21.   Marcano, D.C., et al., *Improved synthesis of graphene oxide.* ACS nano, 2010. **4**(8): p. 4806-4814.

22.   Feng, L. and Z. Liu, *Graphene in biomedicine: opportunities and challenges.* Nanomedicine, 2011. **6**(2): p. 317-324.

23.   Chen, J., et al., *Optical nano-imaging of gate-tunable graphene plasmons.* Nature, 2012. **487**(7405): p. 77-81.

24.   Guo, C.X., et al., *Layered graphene/quantum dots for photovoltaic devices.* Angewandte Chemie International Edition, 2010. **49**(17): p. 3014-3017.

25.   Yao, Y.Q., et al. *A Synthesize Protocol for Graphene Nanosheets*. in *Materials Science Forum*. 2017. Trans Tech Publ.

26.   Eigler, S., et al., *Wet chemical synthesis of graphene.* Advanced materials, 2013. **25**(26): p. 3583-3587.

27.   Trill, J.-H., et al., *NMR investigations on the lithiation and delithiation of nanosilicon-based anodes for Li-ion batteries.* Journal of Solid State Electrochemistry, 2011. **15**(2): p. 349-356.

28.   Stankovich, S., et al., *Synthesis and exfoliation of isocyanate-treated graphene oxide nanoplatelets.* Carbon, 2006. **44**(15): p. 3342-3347.

29.   Zhang, L., et al., *Controlled synthesis of few-layered graphene sheets on a large scale using chemical exfoliation.* Carbon, 2010. **48**(8): p. 2367-2371.

30.   Eda, G., G. Fanchini, and M. Chhowalla, *Large-area ultrathin films of reduced graphene oxide as a transparent and flexible electronic material.* Nature nanotechnology, 2008. **3**(5): p. 270-274.

31.   Ferrari, A., et al., *Raman spectrum of graphene and graphene layers.* Physical review letters, 2006. **97**(18): p. 187401.

32.   Stankovich, S., et al., *Synthesis of graphene-based nanosheets via chemical reduction of exfoliated graphite oxide.* Carbon, 2007. **45**(7): p. 1558-1565.

33.   Ferrari, A.C., *Raman spectroscopy of graphene and graphite: disorder, electron–phonon coupling, doping and nonadiabatic effects.* Solid state communications, 2007. **143**(1): p. 47-57.

34.   Childres, I., et al., *Raman spectroscopy of graphene and related materials.* New developments in photon and materials research, 2013. **1**.

35.   Ferrari, A.C. and D.M. Basko, *Raman spectroscopy as a versatile tool for studying the properties of graphene.* Nature nanotechnology, 2013. **8**(4): p. 235-246.

36.   Cancado, L., et al., *General equation for the determination of the crystallite size La of nanographite by Raman spectroscopy.* Applied Physics Letters, 2006. **88**(16): p. 163106-163106.

Chapter 4 Conclusion and Future Work

This thesis presented a series of experimental investigations on fabrication, electrochemical performance and characterization of Silicon-Carbon composite anodes in Lithium-ion batteries. A microsized branched Si anode with carbon coating was successfully acquired. The previous knowledge constituting study of TiO_2/Graphene nanocomposites was successfully adapted in our study of Si/Graphene nanocomposites. Both of the Si/Graphene nanocomposite and branched Si/C composite demonstrated promising electrochemical performance in Lithium-ion battery tests. Corresponding to the objectives in Chapter 1, the following conclusions were drawn. Possible directions for future work are presented in the end of this chapter.

1. An anode based on micro-sized Si from acid-etching of casting Al-Si alloy scraps was acquired. The microsized Si possessed a unique branched structure with a diameter of 0.5-1 µm in branches, and a length of 5-10 µm. It had the active material loading density of 2 mg/cm^2. With carbon coating, the Si/C anode demonstrated the initial discharge capacity of 3,153 mAh/g at the current rate of 1/16C and maintained a discharge capacity of 1,133 mAh/g at the 100th cycle at the current rate of 1/4C. The capacity decay was less than 0.2% per cycle from the 20th cycle to the 100th cycle. The rate performance of Si/C composite was also promising with a discharge capacity of 488 mAh/g at the current rate of 1C, then decreasing the current rate to 1/8 C was shown to restore the capacity to 927 mAh/g after another 20 cycles. It indicated that branched micro-sized Si anode, with its advantage of low cost, easy dispersion, and immediate compatibility with the current electrode manufacturing processes, may have potential for high capacity large scale Lithium-ion battery manufacturing. The stable electrochemical performance strongly suggests that

spatial structure can be manipulated as another factor to enable microsized Si anode application.

2. Graphene nanosheets were successfully synthesized from graphite flasks by modified Hummer's method to fabricate Si/Graphene composite anodes. The surface oxidation layer of Si particles was taken advantage by amide functional groups for positive charge. The surface treatment by piranha solution lowered the zeta potential of Si surface by ~25 mV which resulted in improved electrochemical performance. With surface treatment, 100 nm Si/Graphene nanocomposites demonstrated the highest discharge capacity of 1,563 mAh/g after 100 cycles at the 0.5C current rate. This work could help the selection of Si particle size and surface treatment process in Si/Graphene nanocomposite anode assembled by other fabrication methods too.

3. The desired graphene quality in Si/Graphene nanocomposite anode was investigated. Large surface area, short defect distance and low charge-transfer resistance were shown to be advantageous in anode application, which was different from the quality requirement in other electronic devices. The graphene synthesized by chemical reduction method possessed the highest specific surface area of 464.8 m^2/g, the shortest defect distance of 9.96 nm and the lowest charge-transfer resistance of 47.33 Ω among three samples studied. It showed promising electrochemical performance in battery test, with the initial discharge capacity of 2,692 mAh/g at the current rate of 0.1C, the cycling performance of 1,135 mAh/g at the 200th cycle at the current rate of 0.5C. This work may be helpful to the design of different types of graphene nanocomposite anodes.

With the knowledge gained in this study, possible future work may continue in two aspects: further investigation of the spatial structure in microsized Si anode to optimize

electrochemical performance; and integration of Si/Graphene anode into the complete commercial Li-ion battery system.

Appendices

Publication List

<u>Yinjie Cen</u>

[1]. Geng, X., Jing, J., <u>Cen, Y.</u>, Datta, R., & Liang, J. (2015). In situ synthesis and characterization of polyethyleneimine-modified carbon nanotubes supported ptru electrocatalyst for methanol oxidation. *Journal of Nanomaterials*, *2015*, 19.

[2]. Geng, X., <u>Cen, Y.</u>, Sisson, R. D., & Liang, J. (2016). An Effective Approach towards the Immobilization of PtSn Nanoparticles on Noncovalent Modified Multi-Walled Carbon Nanotubes for Ethanol Electrooxidation. *Energies*, *9*(3), 165.

[3]. Yao, Y, Xu, Q, <u>Cen, Y.</u>, Li, B., and Liang, J, (2016). "Exposure of Carbon Nanotubes Fabricated by Template-Assisted CVD through a Two-Step Method," *International Journal of Materials, Mechanics and Manufacturing* vol. 4, no. 3, pp. 183-186, 2016.

[4]. <u>Cen, Y.</u>, Yao, Y., Xu, Q., Xia, Z., Sisson, R. and Liang, J. (2016) Fabrication of TiO_2-graphene composite for enhanced performance of Lithium batteries, *RSC Advances* 6(71), 66971-66977.

[5]. <u>Cen, Y.</u>, Qin, Q., Sisson, R. and Liang, J. (2017). Effect of Particle Size and Surface Treatment on Si/Graphene Nanocomposites Lithium-Ion Battery Anodes, *(To be submitted to Electrochimica Acta)*

[6]. <u>Cen, Y.</u>, Qin, Q., Tao, M., Sisson, R. and Liang, J. (2017). The Study of Graphene Quality in Si/Graphene Nanocomposite Anode for Lithium-ion Battery, *(To be submitted to Journal of Physical Chemistry C)*

[7]. Cen, Y., Fan, Y., Qin, Q., Apelian, D. and Liang, J. (2017). A branched micro-sized Si anode for Lithium-ion batteries, *(To be submitted to Journal of Power Source)*

[8]. Yao, Y, Cen, Y., Sisson, R. and Liang, J. (2017) J. A Synthesize Protocol for Graphene Nanosheets, *Materials Science Forum* (Vol. 880, pp. 3-6). Trans Tech Publications